Universidade de Lisboa
Faculdade de Ciências
Departamento de Física

Improving resolution for the Siemens 3T MR-BrainPET

Melissa Raquel da Silva Botelho

Dissertação

Mestrado Integrado em Engenharia Biomédica e Biofísica
Perfil em Radiações em Diagnóstico e Terapia

2015

Universidade de Lisboa
Faculdade de Ciências
Departamento de Física

Improving resolution for the Siemens 3T MR-BrainPET

Melissa Raquel da Silva Botelho

Dissertação orientada pela Doutora Liliana Caldeira e Professor Doutor Nuno Matela

Mestrado Integrado em Engenharia Biomédica e Biofísica

Perfil em Radiações em Diagnóstico e Terapia

2015

“Se vi melhor e mais longe, foi por me ter apoiado sobre ombros de gigantes…”

Isaac Newton

RESUMO

A tomografia por emissão de positrões (acrónimo em inglês: PET) consiste numa técnica imagiológica não invasiva que permite obter informação *in vivo* sobre a distribuição espácio-temporal das moléculas. Antes da aquisição de imagem é necessário que um radiofármaco seja administrado ao paciente para que posteriormente este se distribua ao longo do corpo de acordo com a estrutura química e a fisiologia da pessoa. O PET é uma modalidade de imagem médica que se destaca pela aquisição de informação fisiológica. No entanto a informação anatómica fornecida por esta técnica é bastante escassa. Para contrariar esta limitação foi proposta a fusão do PET com outra modalidade que permitisse este tipo de informação: tomografia computorizada (acrónimo em inglês: CT) ou ressonância magnética nuclear (acrónimo em inglês: MRI). Inicialmente a fusão das duas imagens médicas não permitia a aquisição simultânea, baseando-se no co-registo das imagens adquiridas. Contudo, devido a vários erros causados pelas diferenças no posicionamento do paciente, foi proposto o desenvolvimento de sistemas híbridos que permitem a aquisição simultânea das diferentes imagens. Em 1998 foi proposto o primeiro sistema hídrico (com PET), PET/CT. Como técnicas de CT envolvem radiação ionizante e apresentam um reduzido contraste entre os tecidos moles, o PET/CT foi recentemente substituído por PET/MRI, permitindo a conjugação de informação molecular do PET com informação anatómica, funcional e estrutural da MRI. No entanto, esta fusão apresentou algumas dificuldades, como por exemplo os detetores e a eletrónica do PET serem sensíveis aos campos magnéticos da MRI. Entretanto foram desenvolvidos os fotodíodos de avalanche (acrónimo em inglês: APD) permitindo a construção dos sistemas híbridos PET/MRI. O *BrainPET* foi o primeiro sistema híbrido de PET/MRI, existindo apenas quatro *scanners* em todo o mundo. O *scanner 3TMR-BrainPET*, desenvolvido pela *Siemens Medical Solution Inc.*, foi construído para imagiologia cerebral. Este *scanner* permite a aquisição de imagens PET com alta resolução (3 mm).

Alguns exames médicos como o PET apresentam uma aquisição muito longa (aproximadamente 1 hora), tornando-se difícil para o paciente permanecer imóvel durante toda a aquisição. Por conseguinte, na maioria dos casos, o movimento torna-se inevitável, introduzindo artefactos na imagem e consequentemente degradando-a. Assim, torna-se fundamental corrigir este movimento para assegurar a qualidade ótima das imagens, oferecendo a perspetiva de melhorar o diagnóstico e o tratamento. Ao longo dos anos foram propostos diversos métodos de correção do movimento. Uns corrigem-no no domínio da imagem, corrigindo apenas o movimento entre as frames mas não o que ocorre dentro de cada uma delas, e outros no domínio dos eventos, em que a correção do movimento consegue ser mais precisa uma vez que é feita diretamente nos eventos adquiridos. No contexto PET/MRI, ambas as imagens, PET e MRI, podem ser utilizadas para estimar o movimento e posteriormente corrigi-lo.

Nesta tese focar-nos-emos apenas na correção do movimento da cabeça que é considerado um movimento rígido e os parâmetros que o representam, três rotações e três translações de acordo com os três eixos Cartesianos (x, y e z), podem ser estimados utilizando algoritmos de registo de imagens. Este trabalho apresenta e testa um *software* de código aberto que dispõe desses algoritmos de dados multidimensionais, o *Insight Toolkit* (ITK), permitindo a estimação do movimento no domínio da imagem. O ITK já foi aplicado, com sucesso, em estudos de correções do movimento em modalidades técnicas de imagem, tanto para movimentos rígidos como deformáveis, que é o caso do movimento provocado pela respiração ou pelo batimento cardíaco.

Relativamente à metodologia aplicada neste trabalho, inicialmente foram adquiridas imagens MPRAGE (imagens adquiridas com MRI) com o intuito de descobrir o alcance máximo do movimento da cabeça dentro das bobines do *scanner*. De seguida foram simulados quatro alcances diferentes: 1, 5, 10 e 30 de translação (mm) e de rotação (º) considerando os três eixos (x, y e z). Com o objetivo de testar a versatilidade do software, estas simulações foram realizadas em diversos tipos de imagens como, imagens clinicas, [18F]-FDG (imagem adquirida com PET) e EPI (imagem adquirida com MRI), e imagens de fantomas simulados, fantoma Utah e fantoma cerebral. Ao longo da dissertação foram realizados diversos estudos, como por exemplo, o estudo da influência da estatística de aquisição e do número de iterações do método de reconstrução de imagem na estimação do movimento. A estatística de aquisição influencia qualitativamente as imagens de PET, uma vez que quanto maior a estatística menor é o ruido. Ao mesmo tempo esta também é influenciada pelo número de iterações, visto que à medida que se aumenta o número de iterações o ruído da imagem aumenta, no entanto quando a imagem contém um número de iterações menor esta apresenta um *bias* maior. O ITK estima o movimento a partir de uma comparação de valores de intensidade das imagens, por conseguinte estas alterações qualitativas na imagem levam a diferentes estimações dos parâmetros do mesmo movimento simulado. Como um dos objetivos da tese consiste em verificar se o ITK pode ser utilizado para estimar o movimento no Instituto *Forschungszentrum Juelich* (FZJ), foram, adicionalmente, testadas imagens de cinco exames diferentes adquiridos rotineiramente no *scanner 3TMR-BrainPET* deste instituto.

Em todas as imagens o movimento foi estimado utilizando o ITK. Este *software* apresenta um método iterativo para estimação do movimento. O ITK necessita de duas imagens de *input*, uma imagem fixa e uma imagem movida, enquanto o *output* deste *software* consiste em três translações e três rotações de acordo com os eixos cartesianos (transformada de Euler) que correspondem aos parâmetros do movimento rígido da cabeça. Ulteriormente, para corrigir esses movimentos, foram aplicadas transformadas inversas nas imagens afetadas pelo movimento. Estas transformadas podem ser aplicadas por outro programa, como por exemplo o PRESTO (*PET REconstruction Software Toolkit*), um *software* de reconstrução constituído por bibliotecas desenvolvidas em

programação C++. Neste trabalho, utilizou-se o PRESTO para a aplicação das transformadas, na correção do movimento e na simulação dos fantomas e dos movimentos nas imagens.

Atualmente o FZJ utiliza um *software* diferente do ITK para corrigir o movimento, o PMOD (*PMOD Technologies Ltd*, Zurique, Suíça). No entanto este apresenta algumas limitações, como por exemplo, o facto de ser um *software* comercial e este não poder ser incorporado no *script* de reconstrução, sendo necessário um processo adicional trabalhoso, ao contrário do ITK que permite que a correção do movimento seja feita automaticamente durante a reconstrução, corrigindo o movimento diretamente nas linhas de resposta (acrónimo em inglês: LORs). Adicionalmente o PMOD requer um utilizador com conhecimento prévio sobre o *software* para conseguir manuseá-lo. Para confirmar a viabilidade do ITK e verificar se este pode substituir o PMOD na correção do movimento no instituto, foi feita uma comparação entre os resultados dos dois *software*. Os resultados obtidos revelaram-se muito semelhantes, exceto quando se utiliza imagens de PET com baixa estatística ou imagens com grandes movimentos.

Como as imagens sem correção de atenuação apresentam maior diferença de intensidades entre as fronteiras do objeto em estudo e o fundo da imagem, pensou-se na hipótese de os parâmetros do movimento obtidos pelo ITK ou pelo PMOD poderem apresentar erros menores utilizando imagens sem correção de atenuação. Ao mesmo tempo, como a correção do movimento atualmente no instituto está a ser realizada depois da reconstrução, um mapa de atenuação errado (mapa que não considera o movimento) está a ser aplicado à imagem. Neste sentido, o impacto do mapa de atenuação aplicado às imagens afetadas pelo movimento foi também estudado nesta dissertação. Os maiores erros foram encontrados quando se utilizou imagens sem correção de atenuação. Os bons resultados do PMOD revelaram-se mais dependentes da aplicação do mapa de atenuação correto. Em conclusão o ITK apresentou melhores resultados que o PMOD e a diferença entre as três imagens testadas pelo ITK não se revelou muito significativa.

Com o objetivo de melhorar os resultados obtidos, três métricas diferentes do ITK (*Mutual Information, Mean Squares e Normalized Correlation*) foram comparadas entre si, aplicando diferentes imagens de PET e de MRI como *input*. Este teste mostrou que a métrica é um parâmetro altamente dependente do problema que se tenta resolver. A métrica *mutual information* é a melhor métrica para corrigir o movimento utilizando imagens de diferentes modalidades, enquanto a métrica *normalized correlation* é a melhor nos estudos com imagens da mesma modalidade.

De acordo com todos os resultados obtidos, pode-se afirmar que o ITK é um método viável para a estimação dos parâmetros do movimento rígido e tem capacidades de substituir o PMOD. Esses parâmetros, posteriormente, podem ser utilizados para a correção do movimento no pós-processamento de imagens de PET ou MRI.

Palavras-chave: Correção do movimento, Estimação do Movimento, PET/MRI, BrainPET, ITK

ABSTRACT

The Siemens 3TMR-BrainPET scanner is a hybrid system which allows simultaneous acquisition of MRI and PET. There are medical exams that have long acquisition time and then it is inevitable introducing blurring in images. Therefore motion correction strategies are mandatory. In PET/MRI context, both PET and MRI images can be used for this purpose. Head motion is considered as rigid motion and the motion parameters can be estimated with image registration algorithms. In this thesis a software which has available these algorithms, Insight Toolkit (ITK), will be presented and tested. First MPRAGE images were acquired to check the maximum motion range inside the scanner head coil during acquisition. Therefore four motion ranges were simulated in translation and rotation with respect to the three Cartesian axes. Testing the software versatility, these simulations were realized in different images: simulated and clinical data. Several studies were made with these images e.g. the influence of statistics and number of iterations in motion estimation. Additionally images from five different exams performed in FZJ were also used. The motion was estimated by ITK. The ITK output is three translations and three rotations which correspond to the rigid motion parameters. Subsequently, to correct the motion, inverse transformations were applied in moved images. Actually FZJ uses other software, PMOD (PMOD Technologies Ltd, Zurich, Switzerland) to motion correction. For the purpose of confirm the viability of ITK and to verify if it can replace the PMOD, ITK results were compared with PMOD results. Other tests were made with the aim to improve the results such as study the impact of the attenuation map in motion estimation and the comparison between ITK results using three different metrics. According to results, ITK is a viable method of motion parameter estimation which can be used for PET or MRI post-processing motion correction.

Key-words: Motion Correction, Motion Estimation, PET/MRI, BrainPET, ITK

ACKNOWLEDGEMENTS

I would like to express my gratitude for those that made this work possible.

Primary I want to express a special thanks to Professor Shah to give me the opportunity to work in INM-4 at Forschungszentrum Juelich and to participate in all the PET and MRI meetings.

Secondly I would like to express my deepest gratitude to my external supervisor, Liliana Caldeira, for all contributions of ideas, all dedicated time to my work and for help me to participate in three conferences and in my first training school PET/MR.

I also wish to thank to my intern supervisor, Nuno Matela, for his regular feedback even far away and for providing the contact with the PET group at the Forschungszentrum Juelich.

I am extremely grateful to Dr. Elena Rota Kops and Dr. Jürgen Scheins for all your support, interesting discussions and reviews of my work. I also wish to thank to Lutz Tellmann for all the provided data and suggestions.

I also have to refer others workers of INM-4 at Forschungszentrum Juelich, Nuno Silva, Philipp Lohmann, Christoph Weirich and Michaela Gaens for all the friendly talks during the lunch and for all the fun activities outside of work.

I would like to thank Udo Koehl and his family for all the care and help in my integration at Germany.

I am grateful to all my family, especially to my grandparents, my parents and my sister for all the love and encouragement that they have given me over all the years.

A special thanks to my boyfriend, Pedro Fonseca, for all the love and support during these five years, for his presence in Aachen (Germany) to cheer me up and for his incentive during all 7 months of internship.

I could not forget my colleagues of MIEBB, especially Rita Gigante, Tiago Martins, Danielle Baptista, Mauro Sousa, David Soares and Vasco Verissímo, thanks for your moral support and encouragement. At the same time I want to express thanks to others friends from FCUL for all the great times during these five years. I would also like to thank to my old friends, particularly, Inês Borges for the visit at Aachen giving me some days of fun, and Silvia Almeida for all the help and interest in my work. Finally I would like to thank my friend Ana Morgado for sharing the apartment with me and put up with me during 7 months.

Contents

LIST OF ABBREVIATIONS

[11C]-Flumazenil	Ethyl 8-fluoro-5-methyl-6-oxo-5,6-dihydro-4H-benzo[f]imidazo[1,5-a][1,4]diazepine-3-carboxylate
[11C]-Raclopride	3,5-dichloro-N-{[(2S)-1-ethylpyrrolidin-2-yl]methyl}-2-hydroxy-6-methoxybenzamide
[18F]-FDG	[18F]-Fluor-Deoxy-Glucose
[18F]-FET	O-(2-[18F]-Fluorethyl)-L-tyrosin
[15O]-Water	Oxygen-15 Water
AIF	Arterial Input Function
AMIDE	Amide's Medical Image Data Examiner
APD	Avalanche Photodiodes
ASIC	Application-Specific Integrated Circuit
BGO	Bismuth Germanate
CSF	Cerebrospinal Fluid
CT	Computed Tomography
DICOM	Digital Imaging and Communications in Medicine
EPI	Echo Planar Imaging
FBP	Filtered Backprojection
FID	Free Induction Decay
FLASH	Fast Low Angle SHot
fMRI	Functional Magnetic Resonance Imaging
FOV	Field of View
FZJ	Forschungszentrum Juelich
GE	Gradient-Echo
GM	Gray Matter
GMC	Generic Cylinder Model
ITK	Insight Toolkit
LOR	Line of Response
LSO	Lutetium Oxyorthosilicate
MC	Motion Correction
MAF	Multiple Acquisition Frames
MAP	Maximum a posteriori
MLEM	Maximum Likelihood Expectation Maximization

MOLAR	Motion-compensation OSEM List-mode Algorithm for Resolution Recovery Reconstruction
MPRAGE	Magnetization Prepared Rapid Gradient Echo
MR	Magnetic Resonance
MRI	Magnetic Resonance Imaging
MT	Motion Tracking
NAW-OSEM	Normalization Attenuation Weighted - Ordered Subset Expectation Maximization
NDI	Northern Digital Ins.
NIH	National Institutes of Health
NLM	National Library of Medicine
NMR	Nuclear Magnetic Resonance
OPOSEM	Ordinary Poisson Ordered Subset Expectation Maximization
OSEM	Ordered Subsets Expectation Maximization
PET	Positron Emission Tomography
PMT	Photomultiplier Tube
PRESTO	PET REconstruction Software Toolkit
PSF	Point Spread Function
PVC	Partial Volume Correction
PVE	Partial Volume Effect
RF	Radio Frequency
ROI	Regions of Interest
SE	Spin-echo
Si APD	Silicon Avalanche Photodiode
Si PM	Silicon Photomultiplier
SPECT	Single-Photon Emission Computerized Tomography
SNR	Signal-to-Noise Ratio
TE	Echo Time
TI	Inversion Time
TOF	Time-of-Flight
TOR	Tube of Response
TR	Repetition Time
UTE	Ultrashort Echo Time
WM	White Matter

CHAPTER 1

Introduction

The introduction is divided in two sections. In the first the summarised context of the thesis work is presented and in the second section aim and outline of the thesis are described.

1.1. Context

PET exam provides biochemical and metabolic information however it does not provide detailed anatomical information. Therefore this exam benefits from a fusion with other modality with morphological image information, such as CT, allowing higher diagnostic value than separate modalities (Herzog et al. 2010). Recently MR came to replace CT in this context, hybrid PET/MRI scanners have become commercially available with potential to change medical imaging, especially in cancer area, providing image information with very high resolution. Comparing with CT, MR presents more anatomical capabilities and better soft tissue contrast.

The Siemens 3T MR-BrainPET scanner is a hybrid system for simultaneous acquisition of MRI and PET providing PET images with high resolution (3 mm) (Scheins et al. 2013). Generally PET exams have long acquisition time and because of that the probability of motion during the acquisition is very large, especially for children or patients suffering from medical condition that keeps them from staying still. Motion introduces blurring, distortion and artifacts on acquired images, degrading the achievable image quality in brain images. Because of the motion the image quality can be below acceptable levels for clinic diagnostic for both static and dynamic PET. Therefore the patient diagnostic can be adulterate due to a simple and small motion during the acquisition. Consequently it is fundamental to be able to correct the motion to ensure a precise diagnostics, mainly when the magnitude of motion is substantial in comparison to the image resolution (Jin et al. 2013). One method to try to avoid the motion consisted on the use of restraining devices, however even using it, the head motion cannot be sufficiently reduced to eliminate the image degradation. Other approach is the administration of anesthesia but it is

expensive and commits the patient safety (Maclaren et al. 2013). Therefore, strategies of motion correction (MC) are the best choice to prevent significant quantitative errors in PET images. Several methods have been proposed to solve the head motion problem. Most of them consider the head motion as a rigid motion with six degrees of freedom, three rotations and three translations along the Cartesian system (Jin et al. 2013) (Qin et al. 2009). Estimating these parameters the effect of motion on the image data could be compensated.

Some software provide the motion correction after the reconstruction of the images (e.g. PMOD (Menda et al. 2009)). PMOD is considered the reference tool for PET tracer characterization in Forschungszentrum Juelich (FZJ), but it does not allow to correct for motion the attenuation correction map and to use this corrected map for reconstruction (Multiple Acquisition Frame method). Furthermore motion correction after the reconstruction introduce interpolation effects leading to resolution degradation and possibly artifacts (Gravel et al. 2013). Another proposed method is to include the motion correction in the reconstruction process (Ullisch et al. 2013). Here the lines-of-response (LORs) are individually corrected by applying spatial transformations in list-mode data. For that, PET data can be segmented into frames (discrete parts of similar head positions). Now, it is important to find an automatic motion estimation method that can be easily included in the clinical framework. In this context, Insight Toolkit (ITK) can be used for motion estimation. ITK is an open-source image registration software toolkit that employs algorithms for registering multidimensional data and without the use of tracking devices or markers. After the motion being estimated its correction can be achieved by applying the inverse transformation on moved images, in which each movement of the patient's head has an individual transformation. These inverse transformation have to be applied by a different software such as PRESTO. ITK is a software already used for image registration such as in motion estimation (Akbarzadeh et al. 2013) (Rao et al. 2005).

1.2. Thesis objectives and outline

The overall purpose of the thesis is to evaluate if the ITK can be used to estimate the motion of images acquired by the Siemens 3TMR-BrainPET scanner, i.e. PET and MR images. The motivation of this work is to verify if ITK is able to replace PMOD, software used to correct the motion at FZJ. Comparing with PMOD, ITK has the advantages of it can be implemented in the reconstruction script, therefore the LORs with motion can be corrected during the reconstruction. Therefore an additional step is not required contrary to PMOD. ITK is also an open-source software unlike PMOD.

The thesis report is organized in six chapters. The first chapter introduces the context, aim and organization of the thesis. The second chapter describes different image modalities and it is subdivided on four sections: hybrid systems, Positron Emission Tomography (PET), Magnetic Resonance Imaging (MRI) and PET/MRI. It begin with a resume of hybrid systems and then on a section dedicated to PET, the basic principles, data acquisition and correction and image reconstruction are described. In the other section, the basic and image principles of MRI modality are presented and the image sequences briefly described. In the multi-modalities section the advantages, design difficulties, and applications of the PET/MRI system are presented. On the third chapter the state-of-art of PET motion correction i.e. strategies described on the literature to correct the motion are discussed. In fourth chapter the material used in this work, equipment, software and data, is described. At the same time, this chapter also describes a summary of the performed tests developed in the thesis. In chapter five the results and the respective discussion of all performed tests, described in the previous chapter, are presented. Chapter six includes the overall thesis conclusion and future work. Finally in the appendix an enumeration of conference posters made with this work are listed.

CHAPTER 2

Hybrid medical systems

In the last few decades there has been an increasing interest in multimodal imaging, especially in the field of nuclear medicine. Hybrid systems allow simultaneous acquisition (intrinsically align multi-modality image information within a single exam) of two modalities and besides integrating the strength of modalities also eliminate some weaknesses of the individual modality. Dual-modality imaging systems have been introduced in 1990 by Hasegawa et al. with the combination of single photon emission computed tomography and computed tomography (SPECT/CT) (Tellmann et al. 2011). Here the axial displacement between the CT and SPECT imaging fields are taken into account in images coregistration. An example of SPECT/CT system is shown in Figure 2. 1. In 1998, a prototype system combining PET and CT within a single gantry was presented. However the commercial PET/CT systems only became available in 2001 (Townsend 2008) (see Figure 2. 2). These scanners had such a successful impact that is now almost impossible to buy a PET scanner without an integrated CT scanner (Cherry 2009). PET/CT is now the clinical standard.

Figure 2. 1: Modern hybrid SPECT/CT scanner which incorporates multidetector CT (Hicks et al. 2007).

Figure 2. 2: The first commercial PET/CT scanner to become available. Both CT and PET components operated on independent computer platform (Hicks et al. 2007).

The several advantages of PET/CT in oncological imaging is attracting more interest on bimodal imaging modality. Recently an alternative to PET/CT was presented, PET/MR. The first attempts of simultaneous MRI and PET imaging was reported more than 15 years ago by Simon Cherry's group (Yiping Shao et al. 1997). Comparing with PET/CT, PET/MR provides high spatial resolution (anatomical, functional and molecular imaging) and high soft tissue contrast, and a significant reduction on radiation exposure to patients. At the same time, allows different applications from functional imaging (fMRI), spectroscopy, diffusion imaging and perfusion imaging. PET/MRI also provides shorter acquisition times and allows exact spatial and temporal images coregistration (Weirich et al. 2012). Contrary to PET/CT, PET/MRI has a simultaneous acquisition and therefore the patient does not have to be repositioned for the two acquisitions. The MR information can then be used to identify, stage, and predict several diseases, such as neurodegenerative disorders and cardiovascular disease (Daftary 2010) (Schwenzer et al. 2012). Successful tests of a 3T MR-BrainPET prototype, developed by Siemens Healthcare (Erlangen, Germany) (see

Figure 2. **3**) for simultaneous PET/MRI human brain studies, were performed (Schmand et al. 2007) (Schlemmer et al. 2008). Recently the first integrated hybrid MR-PET scanners for whole-body imaging have been installed (Weirich et al. 2012).

Figure 2. 3: The whole-body PET/MRI hybrid system (Biograph mMR) developed by Siemens Healthcare (www.siemens.com/press/photo/SOH201002-14e).

In the following sections PET, MRI and PET/MRI modalities are individually described in more detail.

2.1. Position Emission Tomography

Positron emission tomography (PET) is a powerful nuclear imaging technique that allows measurement of physiological and biochemical processes *in vivo* using a radiotracer in the body (Bendriem & Townsend 1998). PET provides many physiological information which only would be available with surgeries or more expensive exams. Therefore this modality allows early abnormalities detection in the function or structure of organs, enabling treatment in initial stages and therefore it increases the probability of patient recovery. Before the data acquisition, a radiopharmaceutical or radiotracers is administered to the patient, in a small amount, by inhalation, deglutition or mainly intravenously. The injected patient dose has an optimum value, if is too low there will not be sufficient data for statistics calculations and the image will not represent the true tracer distribution. On the other hand, if the dose is too high it can be dangerous for the patient.

Radionuclides (unstable isotopes) are chemically incorporated into a biological molecule which subsequently will be involved in a metabolic process. This is distributed throughout the body according to the chemical structure of substrate-radionuclide complex which has different tissues affinities. Therefore the choice of radiopharmaceutical will depend on the desired study. The radioactive material concentrates in areas that have high levels of chemical activity that typically correspond to areas of disease. The positron-emitting radionuclides used in PET scanning are typically isotopes with relatively short physical half-life which can be produced mainly in a cyclotron. PET radiopharmaceuticals are based on four major radioisotopes: Carbon (^{11}C), Nitrogen (^{13}N), Oxygen (^{15}O) and Fluorine (^{18}F) (Zimmer & Luxen 2012). Their half-life time are: 20.4 min, 9.96 min, 2.07 min and 109.8 min respectively. The first three can only be used to study rapid uptake processes while the last one allows imaging of longer physiologic processes. Currently, the most widely used PET tracer is fluorodeoxyglucose (FDG or also called fludeoxyglucose and fluorine-18 labeled), an analogue of glucose.

In 1928, the existence of the positron was postulated by Paul AM Dirac, however it only was proved in 1932 by Carl Anderson (Olesen 2011). Both received the Nobel Prize in physics. The first PET scanner used for studies with phantoms was built in the 1970s by Ter-Pogossian, while the first camera for human studies (also called PET camera) was built in 1974 by Phelps and Hoffman (Suetens 2009). In 1977 the first whole-body PET scanner appeared. Currently, there are PET scanners with septa to fully 3D scanners and, in more modern systems, a higher time resolution is possible, using a technique called Time-of-Flight (TOF). With the development of new techniques and methods of acquisition and the use of analytical and iterative reconstruction algorithms it is possible to improve the resolution and sensitivity, making this technique more

generally used. Today PET exams have applications in several areas such as oncology, neurology, cardiology, development of drugs and new tracers.

2.1.1. Basic Principles

Searching stability, radionuclides emit positrons (antimatter equivalent of the electron) due to neutron radioactive decay (beta decay), making it possible to measure the concentration of the radiotracer during the observation period. The positron travels in the tissue for a short distance (few millimeters), also called positron range, which depends on the energy of the isotope. During this time it loses kinetic energy, slowing down and then it interact with an electron. The encounter annihilates the electron and the positron, converting their masses into a pair of annihilation photons of 511 keV moving in approximately opposite directions.

If the positron is at rest, due to conservation of momentum and energy, the photons would be emitted at an angle of 180° and then detected by opposing detectors. The angular deviation from 180 º (± 0.5 °) is known as non-collinearity and it is independent of the radionuclide. Figure 2. 4 shows a basic physics scheme of PET.

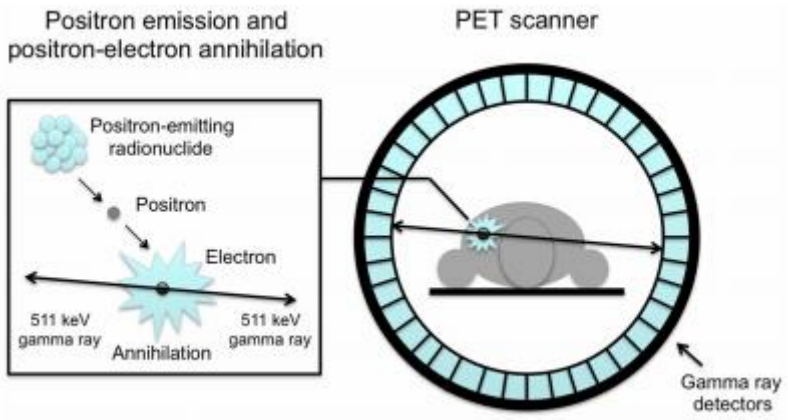

Figure 2. 4: Basic physics of Positron Emission Tomography (van der Veldt et al. 2013).

The annihilation photons are detected when they hit scintillation detectors which are made of scintillation crystals. These convert the photon energy in photons in the visible range, which are detected by, for example, photomultiplier tubes. Here the scintillation light is then converted into electrical current. The electrons are accelerated and amplified by a series of diodes. This is followed by an analogue/digital converter. Several scintillators can be used in PET, e.g. Bismuth Germanate (BGO) or Lutetium Oxyorthosilicate (LSO). In the scintillator choice, many material

properties should be considered, such as the decay constant, energy resolution, stopping power, among others.

The line connecting the two detectors that were hit by the annihilation photons is called line-of-response (LOR) or tube-of-response (TOR), depending on the model used for reconstruction and it is used to obtain the tomographic image.

2.1.2. Events detected in PET

In reality, the annihilation photons are not detected simultaneously due to two main factors: time resolution of the detection system and the difference between the distance of the annihilation site and each detector (Mendes 2012). An event is recorded if the annihilation photons arrive within the user-defined time (usually 4-12 ns) and energy windows, if not they are ignored. At the same time the formed LOR has to be within a valid acceptance angle of the tomograph (Bailey 2005). These events are called prompt events.

An event can be classified as: single, true, random, multiple and scatter. A single event occurs when only one photon of annihilation is detected. The true events are those corresponding to an ideal situation, i.e., the two annihilation photons are detected within the time window without interacting significantly with matter. Random events are detected, within the time window, simultaneously accidentally while the corresponding annihilation photon are not detected. Multiple events are produced when three or more photon, usually from two annihilations, are detected within the same coincidence time window. Usually these events are discarded (Bailey 2005). The scattered events are those in which one or both of annihilation photons change direction due to Compton scattering, introducing wrong LOR/TOR information and then deteriorating the image quality. The amount of these events depends on the object under study and the distribution of radioactivity. Figure 2. 5 shows the five PET events: true, scatter, random, multiple and single.

There are other events that are not even detected because the photon escapes the field of view (FOV) of the scanner or they are absorbed by the body (attenuated), resulting in loss of PET signal.

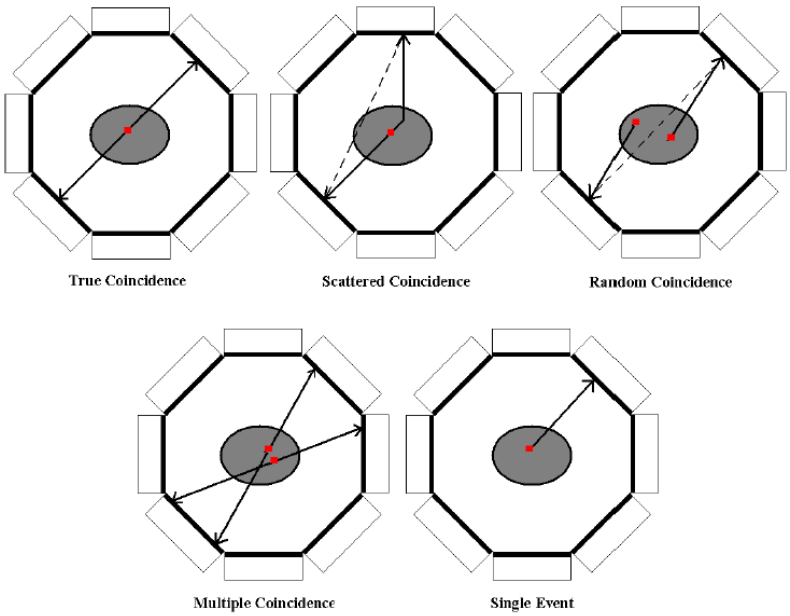

Figure 2. 5: PET events: True, scatter, random, multiple and single events (Mendes 2012).

2.1.3. Data correction

The PET raw data can be store in two different ways: histogram or list-mode. Data correction is an essential step in or before the image reconstruction. This involves the motion, scattered (more than 35% in 3D mode) (Mourik 2009), attenuation and random events corrections. At the same time, factors relating to the scanner characteristics such as normalization and the partial volume effect, should also be taken in account on PET data reconstruction.

2.1.3.1. Normalization Correction

When there are changes in the detection efficiency of the different LORs, artifacts are introduced on reconstructed images, making impossible to recover quantitative information. However these can be compensated by the normalization coefficient. The scanner geometry and non-uniformity of the individual efficiencies of detectors are some causes that contribute to these effects. The first factor is observed in 3D acquisition mode, where not all voxels in space are crossed by the same number of LORs. The central voxels are crossed by a larger number of LORs, so they are more sensitive than the detectors on the edge of the scanner. The second factor occurs when some detectors have different efficiencies, i.e. considering the same acquisition, some detectors detect more counts than others.

An estimation of these factors can be obtained by two methods: direct measurements or components-based methods. The first uses a planar or rotating linear positron source with low activity avoiding dead time and pile-up effect. However this has the disadvantage that scans have to be long enough to obtain adequate counts per LOR (Bai et al. 2002). In the second method the coincidence detection efficiencies of a detector pair are modelled as a product of factors that can be measured (Guerreiro et al. 2009) independently. At the FZJ the normalization data is derived from a rotational plane source (Oakes et al. 1998).

2.1.3.2. Attenuation Correction

The Attenuation effect can be described by Beer's law (Zeng 2010). Here a fraction of the photons do not cross through the object under study. This occurs because the annihilation photons interact with matter primarily through Compton interactions resulting in a decrease in photon energy (increase in wavelength) or through photoelectric effect. Attenuation depends on the photon energy, the electron density and atom number of the absorber. As attenuation is independent of the location of the annihilation along the LOR, it can be corrected by acquiring two scans of transmission, one without any object of study (black scan) and other with the object (Mourik 2009), providing the attenuation map or μ-map.

Each detector pair (and thereby each LOR) corresponds to a particular bin in the sinogram (where the PET data are stored) depending on its orientation angle and distance from the center of the gantry (Fahey 2002). Figure 2. 6 shows the sinogram formation of a brain scan. Attenuation correction factors are given by the ratio between sinograms of the two scans. This allows a precise estimation of the factors, but for that a long period of acquisition is required. Another approach to find the LOR attenuation is to use the source position and the position of the detector hit by the photon. Here a more active source can be used however this leads to an underestimation of the attenuation correction (Mendes 2012). In PET/CT scanners the anatomical images are used to measure the attenuation coefficients. Compared with the direct measurements, this method allows to obtain faster coefficients and with less noise. Disadvantages of this approach are the use of ionizing radiation, low contrast between soft tissues and the low CT data must be converted into a corresponding attenuation estimator of 511 keV. These disadvantages could be excluded using MRI instead of CT, however precise attenuation map defined by PET/MRI is still a research area. This is one of the design difficult of the hybrid system that are better explained in the PET/MRI section of this chapter.

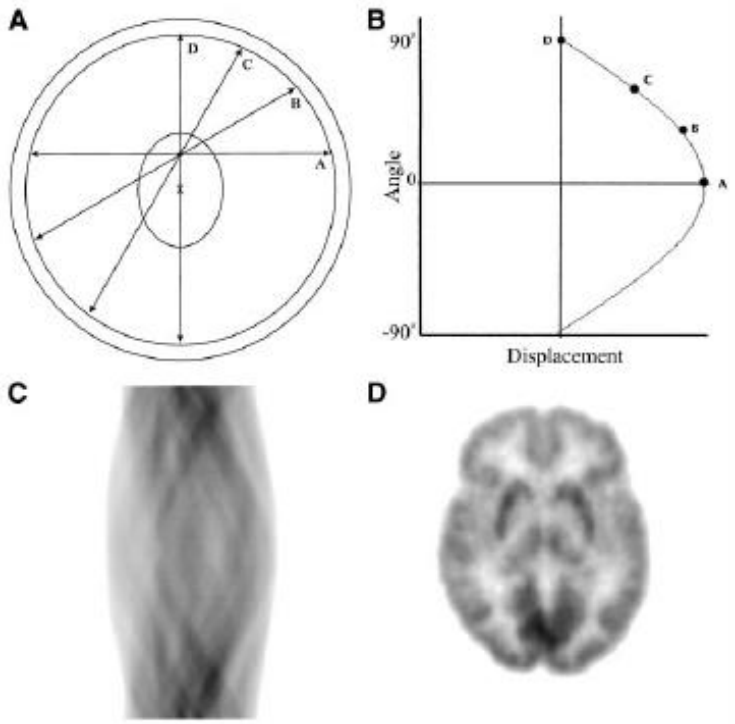

Figure 2. 6: Sinogram formation of brain scan. (A) Four LORs labeled A, B, C and D pass through locus of interest which is noted by ellipse. Center of gantry is noted by a cross (X). (B) The LORs are plotted on a sinogram as function of angular orientation (y-axis) and displacement from center of gantry (x-axis). (C) Sinogram of brain scan and (D) Reconstructed brain image corresponding to sinogram in (C) (Fahey 2002).

2.1.3.3. Scatter Correction

The scattered photons lost some of their energy and changed their direction due to Compton scattering, resulting in erroneous LORs which give a wrong positioning of the annihilation site. Therefore dispersion also has a considerable impact on the image, degrading the quantitative accuracy of the image and reducing contrast. The amount of the scatter events depends on the object under study and the distribution of radioactivity. Three types of approach to the estimation of scattered events have been proposed: analytical approach (Cherry & Huang 1995), methods based on energy window (Ferreira et al. 2002), and simulation methods (Watson 2000) which can be done based on a model or using Monte Carlo methods. At the FZJ, in the BrainPET scanner, the scatter correction method is based on the single scatter simulation algorithm (Watson 2000).

2.1.3.4. Random Correction

Random coincidences result in loss of image contrast and they occur due to the width of the defined time window. The random coincidence rate increases with the square of activity, while the rate of true coincidences only increases linearly (Cherry et al. 2012). In order to correct

random events two methods may be considered, one which uses a single time window and the other that uses two time windows, called the delayed time window. The first method takes into account the rate of single counts for each detector pair and the width of the coincident time window. However this tends to overestimate the amount of random coincidences. The second approach assumes that prompt events are detected in a time window and the delayed window only measure random events and not true events. The delayed window is placed few ns after and it has the same width as the time window. These windows are used to correct the bias introduced by random events (Suetens 2009). There is a variance in the estimation of random coincidences and to reduce this, analytic (Defrise et al. 1991) and iterative (Panin et al. 2007) techniques using sinograms of delayed coincidences were proposed.

2.1.3.5. Motion Correction

In long acquisition exams, the patients cannot be still during the entire exam, introducing blurring on the images. The motion has to be corrected to achieve a good image quality. In order to prevent patient motion (non-physiological) locking devices may be used. However, they are very uncomfortable to patients and only reduce the motion. Movement tracking systems can be alternatively use, however the systems are not always available. Motion correction methods can be used to overcome these limitation. Some of these methods are described in chapter 3.

2.1.3.6. Partial Volume Correction

The Partial Volume Effect (PVE) degrades the image quality, introducing bias in the quantification. PVE does not cause any loss of signal, it shifts the signal from place and then burring the image. PVE refers to two phenomena: spatial resolution and image sampling grid of voxels (Soret et al. 2007). Because of the finite spatial resolution of a scanner, spill-in or spill-out effect of activity between adjacent regions can be observed. These effects are shown in Figure 2. 7. The second phenomenon is caused by the contours of voxels not matching the contours of the distribution of the tracer. Consequently, image voxels include different types of tissue. This is called tissue fraction effect. Even if a PET scanner had perfect spatial resolution, there is still some PVE due to voxels having finite size (image sampling).

PVE is combated by applying partial volume correction (PVC) methods, which can be sorted into two groups: the first is based on regions of interest (ROI), which uses anatomical information extracted from segmented MRI or CT images, and the second group consists in techniques based on voxels, which are applied to partition or multiresolution methods. An alternative to PVC is the resolution modelling (or point-spread-function, PSF), which allows modelling all phenomena that

degrade the resolution in the reconstruction algorithm (Rahmim et al. 2013). PVE complicates the motion estimation because this affects the accurate quantification in PET.

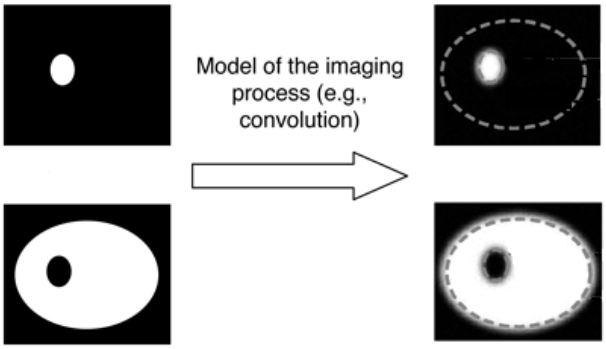

Figure 2. 7: Partial volume effect: spill-in and spill-out (Soret et al. 2007). Due to the spill-out effect the radioactivity of hot area spreads to the background, resulting in a smaller signal within a small structure. On the other hand, due to spill-in, a small structure with a low concentration (cold) that is positioned in a hot background becomes less cold radioactively because the hot area around spreads to it.

2.1.4. Image Reconstruction

The aim of the reconstruction is to determine the relationship between the projection data (the total counts number which are detected along every LOR over the scan duration) and an image which represents the distribution of activity in the FOV. The quality of reconstructed images depends on an accurate model of this relationship (Panin et al. 2006). There are two types of reconstruction algorithms used in PET data processing: analytical and iterative. Analytical methods calculates the tracer distribution directly from the measured coincidences while iterative reconstruction methods estimate the tracer distributions that are iteratively compared to measured data and updated.

Analytical methods allow rapid reconstruction and easy control of the resolution and correlations of noise. Analytical reconstruction is based on a solution of the inverse Radon transform: with the projections along different angles from the sinograms it is possible apply the inverse Radon transform to determine an image from the distribution of activity in the FOV. This transformation is called backprojection. However this method introduces blurring and artifacts in the images. Therefore a high-pass filter is often applied leading to so-called filtered backprojection (FBP), which is a classic and standard algorithm of tomography (Olesen 2011). Analytical algorithms lost their popularity due to the rise of excellent computers available for image reconstruction.

Iterative reconstruction methods are nowadays used in standard clinical practice. They are less sensitive to both detectors geometry and non-uniform resolution for the detectors. Therefore these

methods have improved the image quality (high resolution and the higher signal at regions of low counts) and allow the incorporation of a priori information about the distribution of activity. Figure 2. 8 shows the general model of the most iterative reconstruction algorithms. In iterative reconstruction methods, the process begun with some initial image estimate and then a projection step is applied, yielding a set of projection values. The estimated projection is compared with the acquired projection (measured sinograms) taking into account a given criterion. This comparison creates a set of projection-space error value and they are mapped back to the image space through a backproject operation, producing image-space error values. Finally the image estimate is updated using these error values and a new estimate is created. This process is repeated until the comparison criterion is satisfied. Each of these repetitions is called iteration. The contribution of each image voxel to each projection is described by a system matrix which can be calculated based on numerical integrations, Monte Carlo simulations or experimental measurements (Zhou & Qi 2011).

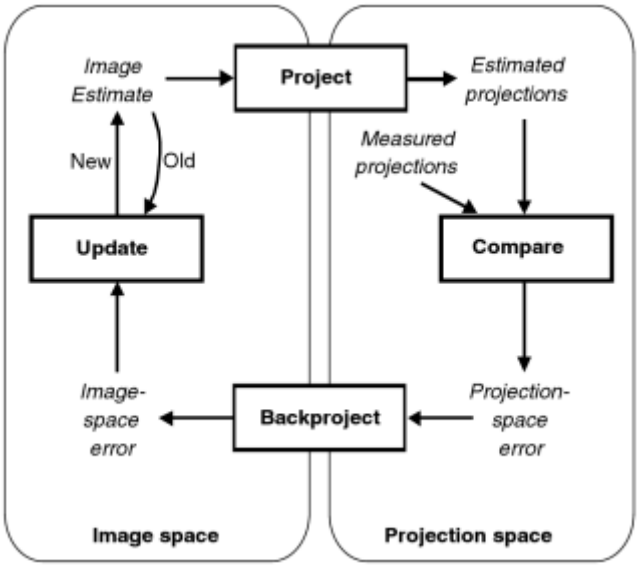

Figure 2. 8: Scheme of the general iterative reconstruction algorithms (Wernick & Aarsvold 2004).

Several algorithms were proposed in the literature, being the maximum likelihood expectation maximization (MLEM) algorithm the most popular (Moehrs et al. 2008) (Cloquet et al. 2010). However, it needs many iterations to converge. The ordered subsets expectation maximization (OSEM) algorithm (Michel et al. 1998) was proposed to replace this slow algorithm. Iterative algorithms are more versatile and flexible than FBP because both pre-corrected data and not pre-corrected data can be used. At the same time some studies have shown that iterative reconstructions should achieve better noise characteristics than FBP (Riddell et al. 2001).

However they are computationally intensive (Pratx et al. 2006). Corrections can be included during the iterative process, for example, normalization and attenuation correction are included in normalization attenuation weighted OSEM (NAW-OSEM). This reconstruction method is preferred in clinical practice because it shows less noise and artifacts.

2.2. Magnetic Resonance Imaging

Purcell and Bloch discovered the physic phenomenon of nuclear magnetic resonance (NMR) in the early 1940s, however it first application as medical imaging was only realized in 1973 by Paul C. Lauterburg. He made the first NMR image by introducing gradients in the magnetic field. Paul Mansfield, in 1974, presented the mathematic theory for fast scanning and image reconstruction but only in 1977 Damadian et al. (Damadian et al. 1977) published the first images of the human body. The Nobel Prize in Medicine or Physiology in 2003 was shared by these two scientists, Lauterburg and Mansfield. Magnetic Resonance Imaging (MRI) is a medical imaging technique that allows acquiring images *in vivo* of morphology and body functions. MRI can provide high soft-tissue contrast and spatial resolution of anatomic images. The images are obtained non-invasively, safely and without ionizing radiation (Suetens 2009). Despite a relatively high cost, magnetic resonance imaging has become an indispensable technique in the diagnosis of various diseases. The MRI device is constituted by a magnet, magnetic gradient coils and a radio frequency (RF) transmitter and receiver. Additionally, to control the signal acquisition a computer is fundamental.

In essence, MRI measures magnetic properties of the tissue. It is based on magnetic fields and electromagnetic energy. In magnetic resonance (MR) a particular atomic nucleus is chosen to generate the signal and then obtain the images. This signal depends on the nucleus and its location in the body. The most common nucleus is hydrogen.

2.2.1. Basic Principles

Besides the electron, the proton and the neutron also have spin angular momentum (or spin for short). The spin of an atomic nucleus consists in the vector sum of the constituent neutrons and protons spins, and its value depends on atomic mass and atomic number.

The human body is rich in water, so it is also rich in hydrogen. When applying an external static magnetic field B, the spins magnetic moment of protons begins to precess around an axis parallel to the direction of the field. This is explained by Boltzmann statistics (Brown & Semelka 2010):

at room temperature, there are less spins in the higher energy level than spins at the lowest energy level. For protons (^{1}H) two orientations are possible: parallel and anti-parallel to B, corresponding to a lower and higher energy states, respectively. The precession has a frequency, ω_0 (Larmor frequency), which is directly proportional to the field B. It is given by the equation:

$$\omega_0 = \gamma B \tag{1}$$

Where γ is the gyromagnetic constant and B is the magnetic field strength in Tesla. This equation explains the basic idea behind data acquisition in MR: the precessional frequency of a given nucleus is a linear function of the magnetic field experienced by that nucleus. For protons, the Larmor frequency is approximately 42.6 MHz in a magnetic field of 1 T.

Magnetic resonance occurs when transitions between the lower and the upper energy stage were performed and this can be achieved using an electromagnetic wave with a radio frequency spectrum range which is equal to the Larmor frequency (so-called RF pulse). The tissue protons absorb the energy and then they are going to occupy higher energy levels (number of antiparallel spins increased), at the same time the spins are force to rotate in phase. The flip angle consist on the angle of rotation relative to the main magnetic field direction. Due to changing energy levels, the net magnetization vector has both longitudinal (higher component in B direction) and transverse component. The net magnetization vector is oriented along the external field and represents the sum of all magnetic moments of the volume of protons. Figure 2. 9 shows the protons in the external magnetic field and the net magnetization are also represented. The appearance of a transversal component is due to an increase in coherence between spinning dipoles. This enables the detection of a signal using a RF receiver coil, according to Faraday's induction law (Freire 2003).

The effects of pulsed RF spins depend on the amplitude and duration of these pulses (applied by means of a coil). The energy absorption process is called excitation. If a pulse of 90° is applied the total magnetization is no longer parallel to the magnetic field B and becomes perpendicular to B, being called transverse magnetization.

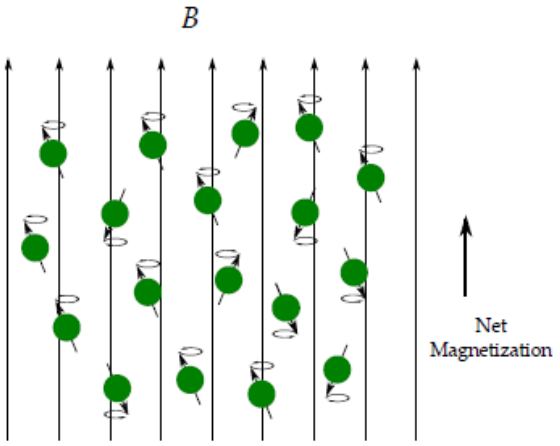

Figure 2. 9: External magnetic field effect on protons (Silva 2012).

When RF pulse ceases to act, the system gradually tends to return to the initial/equilibrium state with emission of energy, a process that is called relaxation. Here the transverse component returns to zero. The relaxation comprises two processes: the spin-lattice interaction (T1 relaxation) and spin-spin interaction (T2 relaxation).

The spin-lattice interaction is the mechanism which results in recovery of the initial situation (after applying a RF pulse), i.e., the value of longitudinal magnetization increase, returning to baseline (protons in the states of higher energy return to the lower states). Recovery occurs in an exponential manner and involves release of energy into the medium, characterized by a spin relaxation time T1. T1 is the time it takes for the longitudinal magnetization to recover 1 - (1 / e) of its maximum value. Its values depend of the strength of B (the higher the field, the higher T1), the flip angle and the composition of the tissues imaged.

T2 relaxation, also called spin-spin relaxation, results in the decrease (following an exponential relation) and then disappearance of transversal magnetization of the net magnetization vector after applying a RF pulse. This occurs due to the incoherent exchange of energy among neighboring spins (individual dipoles do not experience the same magnetic environment). T2 relaxation is a much faster decay mechanisms than the T1 relaxation and it value depends on the tissue under study. When the field inhomogeneities are taken in account it will cause the observable relaxation time, T2* instead of T2. This is cause by susceptibility differences between tissues, non-uniformity of the applied magnetic field and diffusion. T2* will be much shorter than T2 resulting in a more rapid signal loss.

2.2.2. Image Principles

MR signal is generated by an alternating voltage, which happens because during the relaxation process, protons emit an electromagnetic wave with Larmor frequency, called the free induction decay (FID), which is shown in Figure 2. 10. FID does not have a spatial discrimination therefore to obtain a tomographic image using MR techniques is fundamental the use of three spatial encoding steps with the purposes of slice/volume selection and position encoding within the selected slice/volume. This is done by superimposing three linear magnetic field gradients, each one in the x, y and z directions onto the z-component of the main field (Suetens 2009).

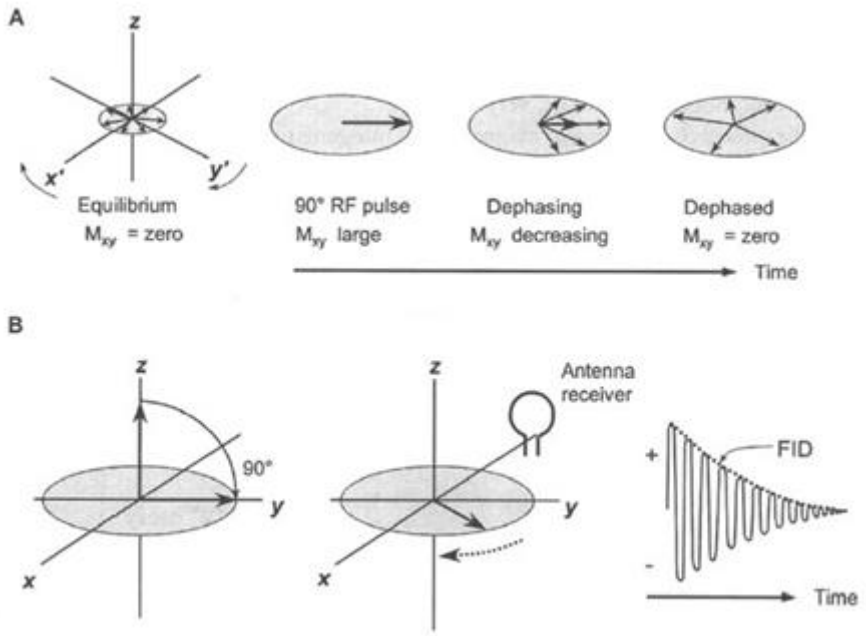

Figure 2. 10: In section A of the figure is shown the conversion of longitudinal magnetization into transverse magnetization, Mxy, and then then the T2 relaxation occurs, which results in dephases i.e. decrease with time and finally the disappearance of Mxy. In section B a 90º RF pulse is applied at equilibrium. Initially Mxy has a maximum amplitude (spins rotate in phase) and then the Mxy precesses and induces a signal in an antenna receiver. A FID signal is produced, oscillating between positive and negative variations at the Larmor frequency. Due to the phase coherence loss the signal decays (Bushberg et al. 2002).

In the most acquisition sequence, the 3D image is reduced to 2D image (or slices). In each slice a RF excitation pulse, with a specific frequency spectrum, is applied in the presence of a magnetic field gradient parallel to B. Here a slice selection is made since only the protons with the Larmor frequency that matches the frequency profile of the RF pulse are excited (Silva 2012). Therefore this gradient is used to change the Larmor frequency of the protons along z direction.

The other two field gradient, phase encoding and frequency encoding gradients, are applied to the selected slice in order to differentiate between the protons within this slice. Phase encoding is

applied in y direction and allows that the individual dipoles precess at different speeds, according to their position along the y-axis. After the gradient is turned off, the dipoles returns to initial frequency, while their phases not. Frequency encoding is applied in x-direction and it will cause a variation on spin frequency of each protons in the selected slice, according to their position along the x-axis.

This raw data are represented by k-space and it was used a 2D Fourier transformed in order to determine the spatial distribution of the signal.

2.2.3. Image Sequences

Different types of image contrast can be acquired with MRI by changing the RF pulse and gradient design through time. The two basic sequences are: spin-echo (SE) pulse sequence and the gradient-echo (GE) pulse sequence. The SE pulse sequence is the most often used in clinical MR and it starts with the application of a slice selection gradient together with RF excitation pulse of 90º followed by other pulse of 180º (Suetens 2009). After the first pulse the protons begin to diphase and then a phase and frequency encoding gradients are applied. In order to undo the dephasing the polarity of the first slice-selection gradient need to be reversed. It is possible when the pulse of 180º is applied because the protons became rotate back towards coherency, promoting the rephrasing of the spinning dipoles. The spin-echo sequence is characterized by very long acquisition times.

The gradient-echo sequence starts with a slice selection gradient simultaneously with an excitatory RF pulse. However, this time, the pulse has a flip angle lower than 90º which can be used to improve acquisition speed. As in the previous sequence, when the RF pulse is turned off, the protons begin to dephase and a phase encoding gradient is applied. Nevertheless the rephrasing step is achieved by alteration of the polarity of the frequency encoding gradient. Figure 2. 11 represents these two sequences.

The time between the excitatory pulse and the echo reading is the echo time (TE) while the time between consecutive excitatory pulses is known as repetition time (TR). These time intervals are used to control the image contrast.

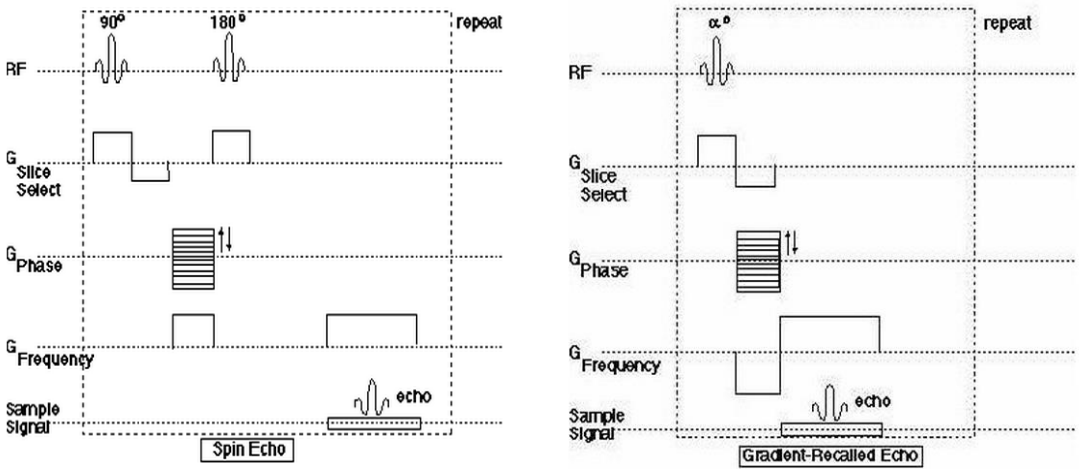

Figure 2. 11: MR sequences: spin-echo (left) and gradient-echo (right). The ∝ is lower than 90º (Zientara 1995).

In this work, three different MR sequences were used: MPRAGE (Magnetization Prepared Rapid Gradient Echo), EPI (Echo-Planar Imaging) and FLASH (Fast Low Angle Shot) sequences. They are briefly described below.

MPRAGE sequence involves three periods: preparation period, data acquisition period and magnetization recovery period before the next preparation, avoiding saturation effects (Bluml et al. 1996). In the first period the T1 contrast are introduced in the image, applying a RF pulse with a flip angle of 180º. The data acquisition period start when the GE sequence is applied (rapid gradient echo) (Silva 2012). Images from MPRAGE sequences present high tissue contrast between gray matter (GM) and white matter (WM) which can be obtained in extremely short time. Changing TR, TE and flip angle parameters, the image contrast can be manipulated (De Lange et al. 1991), being possible get an optimum white-gray matter contrast. At the FZJ, the MPRAGE sequence is acquired in all MR acquisitions after the localizer image (i.e. MPRAGE is the 2nd sequence of the acquisitions).

EPI sequence can be classified as single-shot echo planar sequence and multi-shot planar sequence. The first EPI pulse sequence, and more common, consists in an excitation pulse that is followed by multiple gradient-echoes within a single pulse repetition time (TR) i.e. all the signal information needed to reconstruct the image is obtained in a 'single shot' (Borthakur et al. 2006). Subsequently an alternating frequency-encoding gradient was applied. This acts to diphase and rephrase spinning dipoles, yielding several echoes. The second differs from the first since the range of phase encoding steps is equally divided into several "shots" or TR periods and not acquired in one TR. The EPI sequence is mostly a GE-based, however a SE-EPI can also be performed. An EPI image slice can be acquired in 40 – 150 milliseconds and full 3D images in 1

to 3s (Freire 2003). The EPI sequence allows image acquisition in “real-time” and this is why it is the favorite in functional bold studies.

The FLASH sequence is characterized by two periods. The first period consists in magnetization preparation for tissue contrast while the second is the data acquisition period. This sequence allows longitudinal magnetization to recover faster and then reduce the TR. The FLASH sequence is a fast gradient echo-sequence which uses short RF pulses, resulting in small flip angles (Freire 2003). Using spoiling gradients or an RF spoiling pulse, the FLASH sequence eliminates the residual transversal magnetization prior to each RF pulse. The technique can provide T1- and T2-weighted images with high image contrast at high field strength (De Lange et al. 1991).

2.3. PET/MRI

PET/MRI is a hybrid system that combines the functional imaging with excellent sensitivity of PET and the high resolution, high soft-tissue contrast and great flexibility from MRI. The combination of PET/MRI allows the simultaneous acquisition of multifunctional data such as PET tracer uptake, MR spectroscopy, or fMRI (B. J. Pichler et al. 2008). The first true hybrid PET/MRI system for humans was proposed in 2008, the BrainPET insert which is a head dedicated PET insert system developed by Siemens Healthcare (Sauter et al. 2010). Despite it being a recent system, the first approach was published in 1997 by Shao et al. (Y. Shao et al. 1997). The PET/MRI systems are mainly implemented by Philips (Netherlands), Siemens (Germany) and GE Health Care (Milwaukee) (Jadvar & Colletti 2014). Several challenges were made over the years, however others significant challenges still exist before this hybrid system becomes a routine part of clinical imaging.

Merging these two techniques the limitations of both individual modalities can be reduced offering the prospect of improved diagnostics, treatment and preclinical research (Boss et al. 2010). MR information can be used to improve PET image quality into image reconstruction and post-reconstruction process, increasing the SNR and contrast (Caldeira et al. 2010) and reducing the PVE (Baete et al. 2004). MR information can also be used to smooth the activity within the tissues and make the edges steeper in PET images (Caldeira et al. 2013). Using simultaneous PET/MRI system, the motion parameters can be extracted by MRI and then be applied to correct the PET data. Therefore the motion can be corrected and then the coregistration can be improved.

2.3.1. Design Difficulties

It is important to assure that these modalities can operate together without compromising the performance and with minimal interference. For this hybrid system there are three major concerns in the designing: 1) the photomultiplier tubes (PMTs) of PET are very susceptible to magnetic fields and therefore cannot be used in PET/MR, 2) creating attenuation maps for PET images and 3) find a proper construct for the PET/MRI system.

PET system has photomultiplier tubes (PMTs) which are used to convert the scintillation light from the crystal to an electrical signal with high gain. However PMTs are extremely susceptible to magnetic fields of the MRI scanner. Strategies to combat this interference were proposed. One of them consists in using optical fibers for detection defended by S. Cherry at UCLA (Y. Shao et al. 1997). However long optical fibers attenuates the light emitted by the crystals resulting in a loss of performance (Yamamoto et al. 2010). Other strategy is replacing the PMTs for avalanche photodiode devices (APDs) proposed by Pichler et al. (Pichler et al. 2006) and it has being explored the hypotheses of replacing PMTs for avalanche silicon photomultiplier (SiPM) (Wehner et al. 2014). A third approach consists in shielding the PMTs from surrounding magnetic field.

The attenuation maps are important because attenuation and scatter corrections depends on it. However in a PET/MRI context, creating attenuation maps for PET images is a concern because the map cannot be directly derived from MR images, due to the MR image intensities are not proportional to electron density (Hofmann et al. 2008). There are some approaches to MR-based attenuation correction: segmentation method and template/atlas-based method. In the first method, the attenuation map, which is generated by a transmission scan, is coregistered to the MRI images. This image is then divided into several areas with different attenuation values. After that the attenuation map is applied to the PET images. The atlas-based methods uses an MRI template and an attenuation map template. The MR template is adapted/registered to patient MR image using a non-rigid registration. Therefore the same non-rigid transformation is applied to attenuation map template and then the attenuation values can be assigned to the PET image, based on the attenuation values assigned to the MRI. The attenuation map template is constructed as an average image from several transmission scans. One such approach was proposed by Kops and Herzog (Kops & Herzog 2007) and it is routinely used in FZJ. The method consists in using coregistered measured attenuation maps and MR images to create the template pair (Malone et al. 2011). They applied separate spatial normalization to the MR images and attenuation maps.

A proper construct for the PET/MRI system is essential. It requires a minimal disturbance between the PET ring and magnetic field and the PET detector must have an external read-out or be resistant to magnetic field (Daftary 2010). Additionally to avoid electromagnetic interference all

parts must be shielded. Currently the ideal construct for a PET/MRI system is not found yet, three models were proposed: sequential, insert, and integrated. The sequential system consists in two separated scanners with a moveable table which allows sequential imaging of PET and MRI with minimal patient movements (Cherry et al. 2008). The insert system allows simultaneous acquisition and it consists in a removable PET detector ring that can be placed around the subject or within the MR gantry. In the integrated PET/MRI the PET is already located within the bore of the MRI scanner and simultaneous measurements became possible. Here PET and MR cover the same field of view (Kolbitsch et al. 2014). Figure 2. 12 shows the difference between different PET/MR configuration systems.

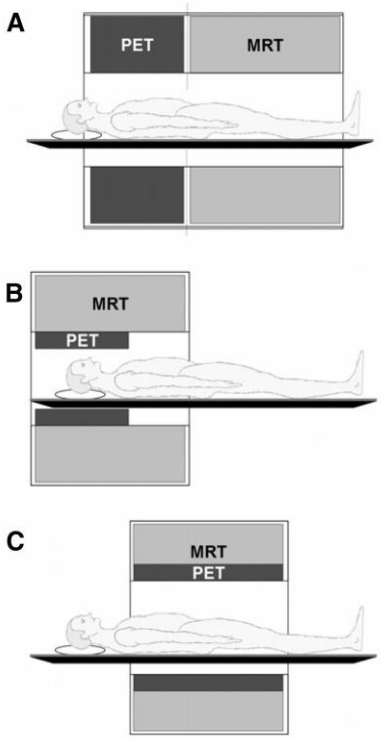

Figure 2. 12: The three possible geometries for combined PET/MRI scanners. (a) the sequential, (b) the insert and (c) the integrated configurations (B. Pichler et al. 2008).

PET/MR may play in the future a larger role in the area of cardiac, head and neck, upper abdominal, and musculoskeletal (Jadvar & Colletti 2014) (Nensa et al. 2014) (Antoch & Bockisch 2009) (Schwenzer et al. 2012). However the area that shows to be more promising is neuroimaging once the brain consists in a relatively symmetric, stationary and rigid structure, which makes it ideal for imaging (Daftary 2010). Others example where the used of hybrid technique introduces clinical value when compared with the separate devices is non-rigid extremities (Miese et al. 2011) and in gliomas imaging (Pauleit et al. 2005). The MR and PET information can be used to study the anatomy and physiology at a macro, microscopic, and molecular level.

CHAPTER 3

Motion Correction

Subject motion is not uncommon during long acquisition time, being the head motion the major cause of image quality degradation i.e. degradation of the spatial resolution and quantitative accuracy in brain imaging (Tsoumpas et al. 2010). Despite introducing artifacts in the images, the motion can lead to wrongly detected signals in the region of interest (ROI). This causes fatal distortions on functional analysis. The intracranial motions are usually not taken into account because they are very difficult to measure. Simultaneously, the brain movements caused from both circulatory and respiratory systems are discarded because they are very small (Olesen 2011). Therefore the brain is considered to be fixed to the skull as a rigid body.

There are several motion correction algorithms that were initially proposed for brain imaging and after were adopted for non-linear cardiac and respiratory motion. The simplest method to reduce the head motion during scanning is the use of restraints e.g. thermoplastic mask (Herzog et al. 2005), which is known from radiotherapy, or neoprene caps (Rahmim et al. 2007). However they are very uncomfortable and some patients cannot used rigid head fixation such as patients with traumatic brain injury or obsessive-compulsive disorder. Furthermore all these restraints devices do not eliminate the motion only reduce it. In PET/MRI, the information can be obtained through the PET or MRI data (or both) allowing the more complete characterization of the motion.

A complete strategy of motion correction (MC) involves two separate stages. First, motion information must be detected using an external motion tracking (MT) system during the scan or estimated from reconstructed images. Secondly the motion is compensated to form motion corrected data. MT is obtained from technologies using alternative hardware devices attached to the patient's head e.g. stereoscopical detectors; optical online motion tracking system (Zhou et al. 2013) (Mourik et al. 2009); or the Polaris systems from Northern Digital Ins. (NDI, Waterloo, Canada) which, at the moment, is regarded as "the state of the art technology" (Olesen 2011). Using this system the information can be accurately determined by direct measurement. Motion

correction techniques can be classified into two categories according to the moment in which they are applied: event domain approaches (during the image reconstruction) and image domain approaches (after the image reconstruction). Event based motion correction techniques consist in correcting the individual LORs affected by motion i.e. each event is relocated to the LOR where it belongs. While in image based motion correction the PET data is divided into discrete time frames which are coregistered, using motion parameters measured by an external device or by using the data itself. Event domain techniques allows to produce motion free images whereas image domain methods will always have intra-frame motion and then can only be considered as motion reduction. These approaches are following described.

3.1. Image domain motion correction approaches

In image-domain MC the frames are independently reconstructed and coregistered to compensate the motion using a reference position. Several image-domain MC methods were proposed over the years. Picard and Thompson (Picard & Thompson 1997) proposed a multiple acquisition frames (MAF) method in which is acquired the data as a series of dynamic frames. These frames are partitioned according to motion magnitude using a threshold value i.e. a new acquisition frame begins when the motion exceeds a threshold of acceptable motion. An optimum threshold is required. If the threshold is too large, the number of frames that will be reconstructed are smaller and they will have good statistics. However, the frames can present high levels of intra-frame motion, blurring the image. On the other hand if the threshold is very small, a large number of frames will be reconstructed but with poor statistics. Here little intra-frame motion is observed. Nonetheless short-duration frames is more expensive in terms of reconstruction time and memory. To solve this problem, iterative reconstruction can be additionally applied, however short time frames can be problematic because significant positive bias was introduced. In MAF method the frames are reconstructed individually, corrected for motion and them they are summed to create the final image (Fulton et al. 2002). The frames are aligned to the others via rigid-body transformations. Here the coregistration can be achieved using automated methods or by manual realignment of the reconstructed frames. The main disadvantage of this method is its inability to correct the motion that occurs during a frame. In addition, interpolation errors will be introduced in transformation. Despite the limitations, the MAF method is widely used nowadays due to its simplicity.

An alternative method was proposed by Menke et al. (Menke et al. 1996) to reduce the image blurring due to head motion during the frame acquisition. This method consist in a post-processing of reconstructed images using deconvolution operators. Kernels which are generated by the motion data are used. The method did not have much success because the deconvolution process

amplifies the noise in the PET data compared to other techniques. Spatially variant deconvolution filters can be used, however, they introduce artifacts and increases the computational costs (Rahmim et al. 2007).

3.2. Event domain motion correction approaches

As previously stated event based MC corrects all the individual LORs into the position as if no motion had occurred using a simple spatial transformation. LOR rebinning is a very attractive technique due to its high temporal resolution and ability to correct individual coincidence events knowing the head pose. The correction of LORs can be made within histogram space or list-mode. Histogram-mode methods may require more time-consuming interpolations than list-mode methods however list-mode correction has a theoretical potential of accurately correcting for all types of motion (Olesen 2011). The event domain MC methods presents some limitations: the scatter distribution changes after the realignment; and some data is discarded because some events are now out of FOV after realignment, reducing the signal, increasing the noise and introducing artifact if the they are not compensated for. At the same time an event that is normally not detected may be detected because of the motion. Several methods of event domain MC was presented over the years and some solutions are reviewed in the following paragraphs.

Daube-Witherspoon et al. (Daube-Witherspoon et al. 1990) was the first to suggest the LOR rebinning method for PET motion correction. Here a coincidence event is extracted from list mode data and represented as an LOR. Each LOR is spatially adjusted according to the measured motion of the head. This compensation of motion is performed before the LORs were recorded in the sinogram.

According to the method implemented by Menke et al. (Menke et al. 1996), due to hardware limitations, the normalization factors for the transformed LORs were used to correct the LORs instead of normalization factors that corresponded to the original detector pairs. Nonetheless this normalization mismatch introduce artifacts. To overcome this limitation, it is required scanners capable of either accurate on-the-fly normalization correction followed by LOR-transformation or the capability to record data in list-mode format, performing the LORs correction later on (post-acquisition) (Rahmim et al. 2008). This method requires much disk space.

Thielemans et al. (Thielemans et al. 2003) suggested a method which allows correcting the events lost due to motion. For that the counts recorded in the motion-corrected sinogram bins are scaled. Using the measured motion information, the scale factors are computed by averaging LOR weighting factors. This method is applied to the sinogram bins before the image reconstruction.

When the number of movements and/or the number of possible LORs is large, this method is computationally expensive. An similar technique was defended by Buehler et al. (Bühler et al. 2004), which the total counts in each motion-corrected sinogram bin are divided according with the motion information. The difference between the two approaches is that in this method the detected events are pre-correct using the normalization factors prior to histagramming while in the method defended by Thielemans et al. it is not possible because the normalization correction is made after the motion-corrected histogramming (Rahmim 2005). However both methods do not resolve the problem of detected events that normally are not detected, which can result in a reduced SNR in the images. Additionally they also present considerable noise.

Bloomfield et al. (Bloomfield et al. 2003) developed a method which accurately monitors the position of the head during a list mode PET acquisition using an optical tracking system, Polaris. In this method, each event is corrected for motion and transformed into the transmission space. The motion is corrected prior to image reconstruction i.e. the spatially re-orienting of each LOR is performed before the sinogram binning process. As Buehler et al., Bloomfield et al. proposed a method which take advantage of the full potential of the PET list-mode data. Rahmim et al. (Rahmim et al. 2004) extended this work using axially rebinned list-mode data (Catana et al. 2011). This method incorporate the motion information into expextation-maximization (EM) reconstruction algorithms however the author defended that the algorithms must be modified including motion-compensated sensitivity correction factors. Carson et al. (Carson et al. 2003) design a the Motion-compensation OSEM List-mode Algorithm for Resolution-recovery Reconstruction (MOLAR). Here the individual events are repositioned in space using motion data from an external tracking devices. The reconstruction is performed directly from the list mode with no pre-corrections. This algorithm is routinely use in human brain PET reconstructions, however has a highly computationally demand to calculate the sensitivity factor and because of that only a small selection from the data is used to calculate an overall sensitivity factor. However if the sensitivity factor is incorrectly calculated, artifacts are introduced and noise is amplified (Noonan 2014).

To combat these problems Qi and Huesman (Qi & Huesman 2002) defended a method which consists in modifying the probability system matrix of the iterative EM algorithm. This algorithm can be written in histogram-mode or in list-mode. In this approach the normalization correction can be included in two ways: as an intrinsic component of the system matrix element or as a pre-correction factor (Rahmim et al. 2007). The advantages of this methods are: it incorporate all detected events in reconstruction, unlike the LOR rebinning method; and it does not requires interpolation, avoiding errors caused by it. On the other hand this method is computationally expensive.

Besides the limitation previously approached (sensitivity loss cause by LORs either moving in or out of the FOV), the event based MC also presents some difficulties in calculating the differential sensitivities of the transformed LORs. However, comparing with the image based MC, the event based MC has some benefits: prevents intra-frame motion and the need of the reconstructed PET images transformation, avoiding the interpolation effects; allows MC on low statistics frames; and data reframing was not required (Noonan 2014).

Summarising, in brain PET imaging, event domain motion correction has the potential for the highest accuracy for making the maximal use of the time resolution of data. Nonetheless ITK, an image based method, is the method used in this thesis to estimate the motion and comparing with event based methods, these methods are generally less computationally demanding and because of that they are more popular. These methods are more straightforward and therefore they are widely used for multi-image modalities coregistration such as PET or MRI. Despite ITK is an image domain method, it can be implemented in the reconstruction script, being possible to correct the LORs individually using the motion parameters estimated by it.

CHAPTER 4

Materials and Methods

Chapter 4 concerns the equipment, the software and all the data used in this work. Additionally a briefly description of the performed tests are also presented.

4.1. Equipment

Besides a computer, the only equipment used to perform this work is the 3TMR-BrainPET scanner for data acquisition.

4.1.1. 3TMR-BrainPET scanner

In the FZJ, the hybrid scanner MR-BrainPET is a Siemens 3 Tesla Tim-Trio system (MAGNETOM MRI) with an integrated Siemens BrainPET insert of high resolution (Miese et al. 2011). The BrainPET is located inside of the MR bore (see Figure 4. 1) and is fixed with the use of an air cushion. This hybrid scanner allows simultaneous data acquisition of MR and PET, opening new opportunities especially for brain studies.

In technical terms the BrainPET consists in a compact cylinder with a length of 72 cm, an outer diameter of 60 cm and an inner diameter of 36 cm (Chun et al. 2012). The BrainPET presents an axial field-of-view (FOV) of 19.2 cm. This scanner has a gantry with 32 copper-shielded detector cassettes arranged in a ring (Figure 4. 1). Due to electronical and mechanical limitations in the scanner design, there are gaps between the cassettes (6 mm of wide) and between the detector blocks (2.5 mm of wide) (Shah et al. 2014). In this scanner there are five axial gaps and in transaxial direction, there are gaps corresponding to 3 crystals. (Caldeira et al. 2012).

In front end of the detector modules, each cassette contains 6 compact detector blocks with 12 × 12 = 144 LSO crystal array, which measure 33 × 33 × 63 mm^3. The crystals have the dimension of 2.5 × 2.5 × 20 mm^3 and they are coupled to 9 (3 × 3 array) avalanche photodiodes (APD), each with an area of 5 × 5 mm^2 (Kolb et al. 2012). The small width of the crystals leads to an image resolution of approximately 3 mm. In total, the system comprises 27648 individual crystals resulting in approx. 250 millions LORs. Each detector module has a high voltage board which supply 500 V to the APDs, a board with a custom 10-channel charge sensitive pre-amplifier ASIC (application-specific integrated circuit), a pulse-shaping and mapping board and ASIC output driver board (Herzog et al. 2011). Each cassette is copper shielded, avoiding interference with the MR radio-frequency field.

In BrainPET exams a dual head coil was used: an inner eight channel coil that only receives signals and a single channel birdcage element used for both transmitting radiofrequencies pulses and receiving the signals. Therefore the annihilation photons need to traverse the RF coils before reaching the scanner, which causes little attenuation of radiation for 511 keV photons. At the same time the coils allow regular MR excitation and signal acquisition.

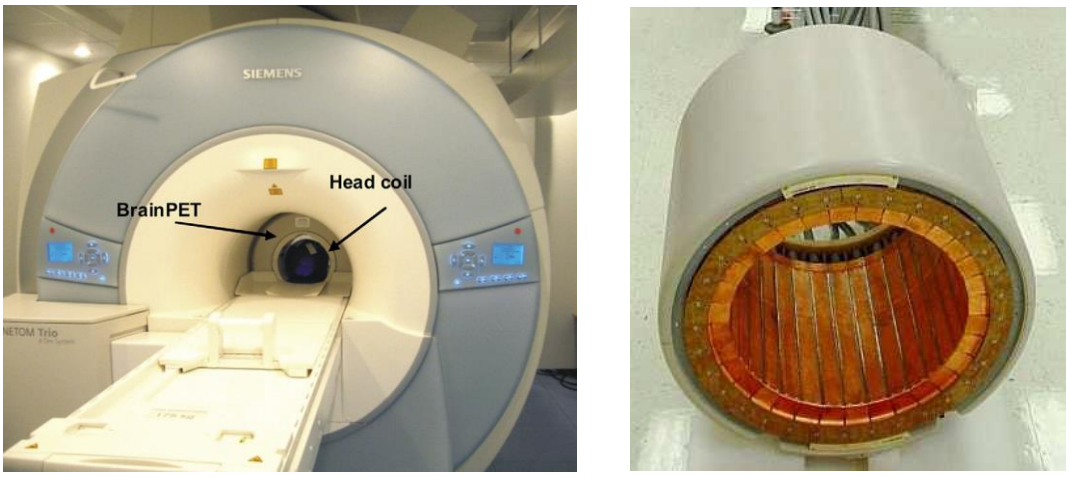

Figure 4. 1: On the left image is represented the 3TMR-BrainPET hybrid scanner for brain studies in humans installed at the Forschungszentrum Juelich and on the right image is shown the MR-compatible BrainPET scanner with 32 copper shielded cassettes (Weirich et al. 2010).

The pre-amplified analog signals of each detector cassette are transmitted to the filter plate through shielded cables with 10 m of length and thereafter to the data acquisition electronics. Most of PET electronics is isolated from MR cabin avoiding interferences. The rest of signals processing is performed on hardware which are located outside the MR cabin. The BrainPET temperature is stabilized with cooled air because the APDs are temperature dependent (Herzog 2012) since any temperature fluctuation strongly influences their internal gain. Temperature

sensors are placed in the detector heads and their information are sent to the acquisition computer, allowing the temperature regulation.

The PET and MRI data acquisition systems are independent of each other. A standard console is used to control the MR sequences and to display the reconstructed MR images, whereas the PET acquisition is manipulated by commands within the PC command window (Herzog et al. 2011). The synchronization of the two modalities is made by feeding the output trigger of the MR scanner into the PET trigger signal port (Ullisch et al. 2012). It was proved that there are no relevant interferences between the two modalities (Herzog et al. 2014). All PET data are recorded in list mode which can be divided into time frames with duration from several minutes to a few seconds.

The 3T MR-BrainPET is not a commercial product. Therefore it can only be used in human studies that were approved by the local ethical committee, and a prior informed consent must be obtained from the patients (Herzog et al. 2011). The BrainPET was the first prototype of an MR-compatible PET scanner for human imaging. Four prototypes have been installed between 2006 and 2010 at: Tübingen (University Hospital), Boston (Massachusetts General Hospital), Jülich (Forschungszentrum Juelich) and Atlanta (Emory University). At FZJ, the BrainPET was installed in 2008 and it operates with an energy window from 420 to 580 keV and the coincidence window is 9 ns (Herzog 2012).

4.2. Software

For any type of medical image analysis it is vital to have access to computational resources as software. On this work different software were used: PRESTO, ITK, PMOD and AMIDE. They are described below.

4.2.1. PRESTO

PRESTO (PET REconstruction Software Toolkit) is a novel and competitive reconstruction software C++ library which was designed to approach some physical limits in image quality (J J Scheins et al. 2011). The software has been successfully demonstrated for the Siemens 3TMR-BrainPET scanner (Caldeira et al. 2010), ECAT HR+ human whole body PET scanner and for the ClearPET Neuro small animal scanner (Scheins & Herzog 2008). Therefore PRESTO can be considered a versatile reconstruction framework. In PET/MRI context, the precise head motion tracking information derived from Echo Planar Imaging (EPI) volumes of the MR can be used to

correct measured LORs before image reconstruction. Figure 4. 2 shows the fusion of MRI and PET images, the PET images were reconstructed using PRESTO.

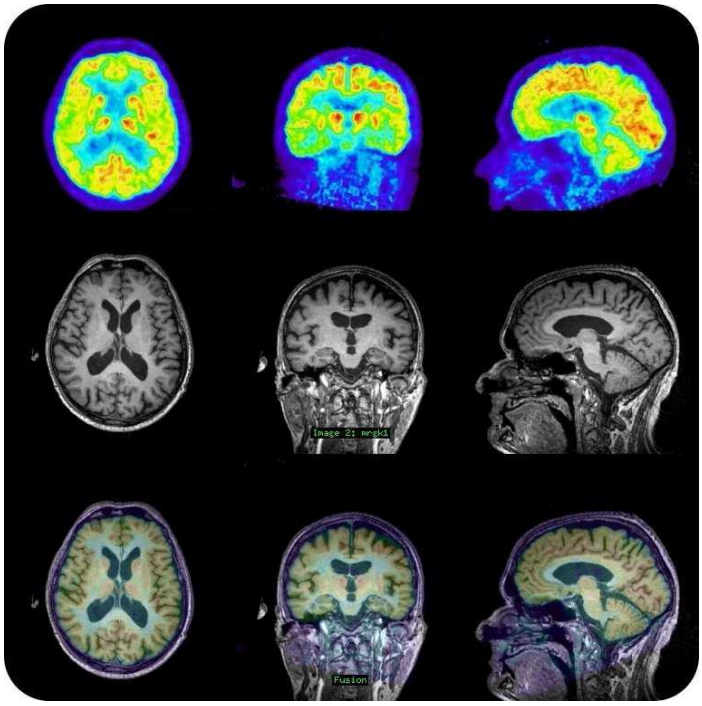

Figure 4. 2: Simultaneously measured PET and MR images. First row: [18F]-FDG image. Second row: T1-weighted MR image (MPRAGE). Third row: Fusion of FDG and MPRAGE image. The PET images were reconstructed using the image reconstruction platform PRESTO (Weirich et al. 2010).

This software provides a new and straightforward method to reconstruct motion corrected LOR data taking the detector sizes into account. The transformation of the patient head position has been calculated and then for any head position an individual rigid transformation of the physical detector system is applied. PRESTO consists in a basic geometrical interface called Generic Cylinder Model (GCM) and it uses idealized generic projection space instead of conventional sinograms. Additionally axial (span) and transaxial (mashing) data compression (Scheins et al. 2013) or rebinning are not used (Scheins et al. 2009). The software focus in improving the PET image quality, in terms of better resolution and less noise, rather than focusing on computational effort. The effort is based on all motion-corrected LORs converted into highly accurate generic projection data. The very high number of generic LORs are independently considered in the reconstruction, avoiding the degradation of motion-corrected projection data. PRESTO uses the OSEM algorithm (Scheins & Herzog 2008).

4.2.1.1. Generic Cylinder Model

Considering a simple cylindrical surface in a regular polar grid, any combination of two points on the surface defines a unique 3D LOR (see Figure 4. 3). Each one has 4 degrees of freedom which are characterized by geometrical parameters, two in transaxial orientation, radial shift (ρ) and angle of vision (θ), and other two in axial orientation, shift in axial direction (z) and inclination relative to transaxial plan (Φ).

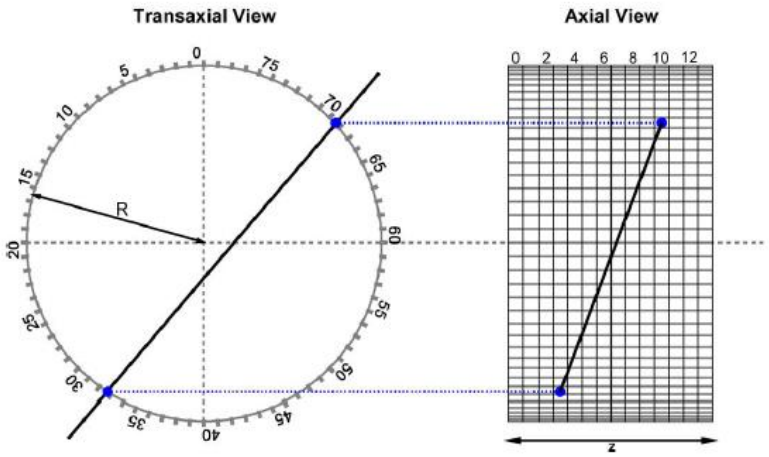

Figure 4. 3: GCM with an intersecting LOR. This figure shows a cylinder with radius R and axial length z (J J Scheins et al. 2011).

The generic cylinder can be used as an abstract LOR generator (J J Scheins et al. 2011). Some parameters such as the cylinder diameter and the full axial width can be adapted by the user. If these values are the same the generic cylinder have identical size. For a viable reconstruction is vital to obtain a finite number of LORs. Therefore the cylinder surface can be divided into generic crystals of equal size in the transaxial plane arranged in multiple generic rings along the axial direction. Here a combination of generic crystals, in a uniform grid, is addressed by two integral values, the ring and the crystal identifiers. Each combination covers a unique 3D TOR which can then be addressed by a combination of specific crystals. Due to physical constraints, some crystal combinations contain non-relevant data. An idealized PET system is represented by the GCM which allows modelling correctly the TOR sampling pattern (J J Scheins et al. 2011).

Projection Data Manager is the C++ class where the generic projection data are implemented. The maximum possible difference between rings (axial acceptance) and the maximum field-of-view radially (transaxial acceptance) can be user-defined, limiting the total number of evaluable TOR. The adjustment between effort and accuracy is essential. A higher granularity provides more but smaller TORs.

Any given detected 3D LOR are uniquely assigning to a corresponding "best-matching" TOR (Figure 4. 4), minimizing parallax errors and geometrical divergences (Scheins et al. 2009). For any detected LOR the user provides the signal strength and then the 3D points of intersection on the cylinder surface are calculated.

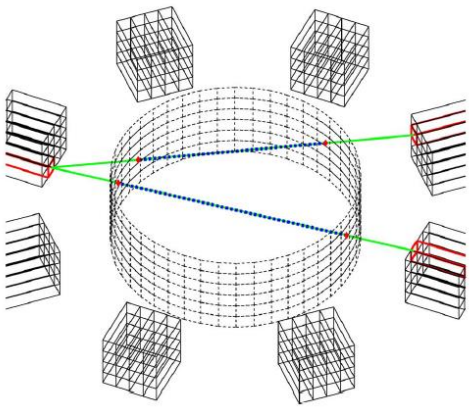

Figure 4. 4: Sketch of the data conversion between physical LORs and generic TORs (J J Scheins et al. 2011).

As the generic crystal patterns are closely related to the scanner system, some GCM basic parameters have to be individually adapted. The gaps structures of the scanners are considered, being the generic crystals modelled as dummy rings. For fully 3D PET image reconstruction, intrinsic symmetries can be implemented to significantly reduce the size of the system matrix and therefore the computing demands (J J Scheins et al. 2011).

The PRESTO library is still under development, further improvements with respect to image quality and computing performance have to be done. However this is depending on the available computing resources. Besides all the PRESTO advantages it do not allows motion estimation, therefore ITK software can be used for this purpose. Nonetheless, in this work, all the motions and its corrections are simulated by PRESTO and the phantom images too.

4.2.2. ITK

Motion correction in medical images is the focus of the thesis, therefore an open-source software was used for motion estimation: Insight Segmentation and Registration Toolkit (ITK). ITK employs several functions and leading-edge algorithms for medical images especially for registering (Andres & Isoardi 2007) and segmenting (Todd et al. 2009) multidimensional data (http://www.itk.org/). The library is implemented in C++ and is compatible on Linux, Mac OS and Windows platforms. ITK has about seven core libraries and third party libraries. Using ITK

it is possible to continuously update the toolkit content: new algorithms can be added while simultaneously improving and extending existing ones. The medical image community built a platform to share the daily workflow that includes the true practices of the scientific method. Here a publication with full details of the methodology was required.

The US National Library of Medicine (NLM) of the National Institutes of Health (NIH) was responsible for the introduction of ITK in 1999. Since then ITK was used, upgraded and followed by several developers around the world. The ITK repository currently contains over 2.5 million lines of source code (McCormick et al. 2014). Actually ITK is considered a standard open source environment for medical image processing (Muller et al. 2006). In 2005, the open publication scientific journal, the Insight Journal, was created by ITK community. Here the introduction and presentation of new algorithms were made. All published articles must include the full set of source, data, parameters and auxiliary documents, making the future code integration easier. All this information is immediately made available to reviewers and readers. Since 2005 it has published 256 articles with 477 public reviews and it has more than 2400 subscribed readers (McCormick et al. 2014).

It is important to ensure the code quality and growth of the ITK community, avoiding defects in the code and ensuring consistency and coherency across the toolkit. The synergy of some tools such as the configuration system CMake, the online quality control dash board CDash, the revision control Git and the code review system Gerrit are responsible for this implementation (McCormick et al. 2014). It is complemented by several tools e.g. mailing lists, wikis, weekly phone calls, and regular online video conference meetings.

4.2.2.1. ITK metrics

ITK provides several metrics that can work with any transform or interpolation method. Nonetheless, only three of them were approached in this work: Mutual Information, Normalized Correlation and Mean Squares. The ITK metric quantitatively measures how well the moved image fits the reference image. This is made by comparing the gray-scale intensity of both images (Johnson et al. 2015). The used metric is an important registration prerequisite. However there are no clear-cut rules as to how to choose a metric. The three metrics will be described below. The fixed image is referred as image A and the moved image as image B.

Mutual information: In this metric, as the name implies, the mutual information between image A and image B was computed i.e. it was measured how much information one random variable (image intensity in one image) tells about another random variable. Using this metric it is not necessary to specify the actual form of dependency and because of that it allows to model a

complex mapping between two images. Therefore Mutual information is the metric of choice when images from different modalities need to be registered.

Mutual information is defined in terms of entropy which is calculated using the probability of the outcome occurring. Being $H(A)$,

$$H(A) = -\int p_A(a)\log \mathrm{p}_\mathrm{A}(a)da \tag{2}$$

and $H(B)$ the entropy of random variables A and B respectively, the $H(A,B)$ is the joint entropy of A and B.

$$H(A,B) = -\int p_{AB}(a,b)\log p_{AB}(a,b)dadb \tag{3}$$

Mutual information, $I(A,B)$, is calculated in the following way:

$$I(A,B) = H(A) + H(B) - H(A,B) \tag{4}$$

Mutual information can be implemented in different ways. The method used in this work was defended by Mattes et al. (Mattes & Haynor 2001). The parameter *Set Number Of Spatial Samples* defines the number of random pixels (sample points) used to compute the metric. Increasing this parameter improves the smoothness of the metric from one iteration to another, however a trade-off is necessary because large number of samples result in longer computation times.

Normalized correlation: The normalized correlation metric computes pixel-wise cross-correlation and then a normalization is made using the square root of the autocorrelation of the images A and B.

$$\mathrm{NC(A,B)} = \text{-1 x } \frac{\sum_{\mathrm{i=1}}^{N}(\mathrm{A_i}.B_i)}{\sqrt{\sum_{\mathrm{i=1}}^{\mathrm{N}}\mathrm{A_i^2}.\sum_{i=1}^{N}B_i^2}} \tag{5}$$

A_i is the i-th pixel of Image A

B_i is the i-th pixel of Image B

N is the number of pixels considered

-1 is the optimal value of this metric. Small values correspond to misalignment between the fixed and moved images. Contrary to Mutual Information, Normalized correlation is not based in an

information theory concept, then it is a more simple method and requires the use of images obtained by the same modality. Using this metric is possible registering objects whose intensity values are related by a linear transformation. Normalized correlation metric is insensitive to multiplicative factors between the two images.

Mean Squares: The mean squares metric performs the mean squared pixel-wise difference in intensity between image A and B over a region.

$$MS(A,B) = \frac{1}{N}\sum_{i=1}^{N}(A_i - B_i)^2 \tag{6}$$

A_i is the i-th pixel of Image A

B_i is the i-th pixel of Image B

N is the number of pixels considered

This metric assumes that intensity representing the same homologous point must be the same in both images (Johnson et al. 2015). Therefore this is a simple metric which is also restricted to images of the same modality. The optimal value is zero and large values of the metric correspond to poor matches between images A and B.

4.2.2.2. Motion Correction using ITK

ITK is already used to obtain the motion transform for both rigid and deformable PET motion corrections for simultaneous PET/MRI scans (Liu et al. 2014) (Cheng & Laforest 2013). The ITK motion estimation consists in a match of the intensity between the images i.e. a histograms match of the two images at a user-specified number of quantile values. For motion estimation is necessary a fixed and moved images, an interpolator, a transform and an optimizer. The aim of this iterative process is find out the transform needed to align the moved image to the fixed image. The interpolator is used to compute the moving image intensity at the mapped position. The optimizer component is used to optimize the quantitative criterion over the search space defined by the transform parameters. Figure 4. 5 shows this registration framework. ITK can be incorporate in the reconstruction and then it can be used to correct all the LORs individually.

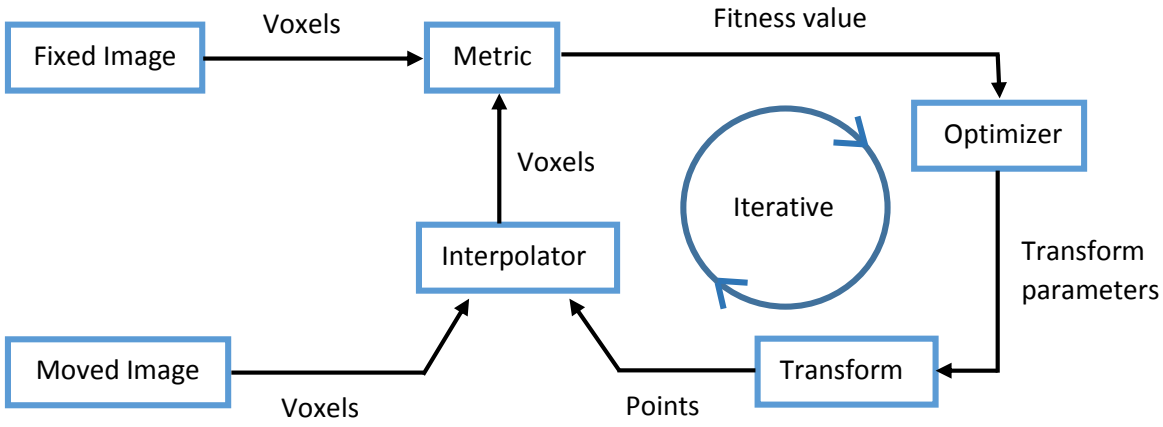

Figure 4. 5: Components of the multi-resolution registration framework. Adapter from (Johnson et al. 2015).

ITK provides six parameters representing the underlying motion: three translations and three rotations (Euler Transform), which can be used to apply the inverse transform on the moved images using an additional software as PRESTO.

4.2.3. PMOD

PMOD is an imaging software that consists in a set of user-friendly and powerful tools especially used for PET and MRI data analysis (Shah et al. 2014) (Maramraju et al. 2011) (Beer et al. 2007). Using this software the researchers do not have to focus in programming. It has a simple and straightforward interface that allows quantify images in biomedical research such as in Nuclear Medicine. PMOD can be used for time-activity data analysis and subsequent kinetic analysis (Schnell et al. 2009) (Beer et al. 2005). Here images can be read and written in multiple formats such as DICOM and ECAT. This software is a Java application compatible with Windows, Linux and MacOS X. PMOD runs on standard computer platforms and it can be acquired as a stand-alone or a network license protected by a USB key. The user community has more than 400 sites with over 1000 users worldwide. The PMOD application for researching is documented in over 840 peer-reviewed publications (http://www.pmod.com/).

PMOD's fusion tools (PFUS) (version 3.204) can be used for motion correction on dynamic studies (Menda et al. 2009) and it is used in this thesis with this purpose. The tool provide a registration of multi-modal images with interactive precision adjustment of the alignment and brain image normalization (User's Guide PMOD 2008). At the same time the user can explore the functional images in detail.

4.2.3.1. Motion Correction using PMOD

As PMOD is a recognized viable program to correct the motion, one important step for this thesis is to compare the ITK uncertainties with PMOD uncertainties. Using PMOD it is also possible to calculate the spatial transformations and then apply the inverse transformations on the moved images. However, in this case, the motion can be only corrected after the reconstruction. PMOD differs from ITK because it cannot be implemented in the script of reconstruction and therefore an additional and hard-working step is needed.

For motion correction it is necessary to load the reference frame and the frames affected by motion. After the correction, values of the affine transform can be extracted. The 3D affine transform which express the translations is:

$$Translation: \begin{bmatrix} 1 & 0 & 0 & \Delta x \\ 0 & 1 & 0 & \Delta y \\ 0 & 0 & 1 & \Delta z \\ 0 & 0 & 0 & 1 \end{bmatrix} \tag{7}$$

In addition, the matrices which represent the three rotations are:

$$Rotation\_about\_the\_x\_axis: \begin{bmatrix} 1 & 0 & 0 & 0 \\ 0 & \cos\phi & -\sin\phi & 0 \\ 0 & \sin\phi & \cos\phi & 0 \\ 0 & 0 & 0 & 1 \end{bmatrix} \tag{8}$$

$$Rotation\_about\_the\_y\_axis: \begin{bmatrix} \cos\theta & 0 & \sin\theta & 0 \\ 0 & 1 & 0 & 0 \\ -\sin\theta & 0 & \cos\theta & 0 \\ 0 & 0 & 0 & 1 \end{bmatrix} \tag{9}$$

$$Rotation\_about\_the\_z\_axis: \begin{bmatrix} \cos\psi & -\sin\psi & 0 & 0 \\ \sin\psi & \cos\psi & 0 & 0 \\ 0 & 0 & 1 & 0 \\ 0 & 0 & 0 & 1 \end{bmatrix} \tag{10}$$

With appropriate calculations the motion range (translation and rotation with respect to the three Cartesian axes) can be found. These rigid-body equations of motion, which correspond to Euler transform equations, are represented by:

$$Translation: \begin{bmatrix} \Delta x \\ \Delta y \\ \Delta z \end{bmatrix} \tag{11}$$

$$Rotation: \begin{bmatrix} \phi \\ \theta \\ \psi \end{bmatrix} \tag{12}$$

4.2.4. AMIDE

Amide's Medical Image Data Examiner (AMIDE) is an open-source software tool for viewing, analyzing and registering simple and multimodality volumetric medical imaging datasets, such as PET, CT, MRI (Loening & Gambhir 2003). These datasets can be handled with differing voxel sizes and dimensions. The software is a tool easily manipulated, the images can be shifted, rotated and viewed, among others. AMIDE allows to overlay the images and change their colormaps.

This software runs on Linux, Mac OS X and Microsoft Windows platforms. AMIDE was used to view the images during the experimental work and to extract all the images to present in the thesis.

4.3. Data

In this subsection all the data used in this work such as images and phantoms are described.

4.3.1. MPRAGE images

MPRAGE images from volunteers were used because they have an excellent spatial resolution (Nelson et al. 2008) and provide high contrast between gray and white matters and cerebrospinal fluid (CSF), which can be helpful to evaluate the motions and their corrections. This sequence is obtained in extremely short imaging times (De Lange et al. 1991). The images were acquired in the Siemens 3TMR-BrainPET scanner at FZJ and each MPRAGE sequence took 5 minutes and 14 seconds of acquisition. Information about MPRAGE sequence is shown in Table 4. 1.

Table 4. 1: MPRAGE sequence information.

Datasets	Matrix Size	Voxel Size (mm)	Sequence parameters
MPRAGE images	256 x 256 x 176	1	Flip Angle: 9º TE: 3.03 ms TR: 2250 ms TI: 900 ms GRAPPA Factor: 2

4.3.2. Utah phantom

A Utah phantom was used in some studies throughout the experimental work. The images were simulated analytically with three different statistics (1.00E6, 2.25E7 and 1.00E9) and it was included realistic fractions of scatter (35%) and random events (35%) with respect to true detected events. These simulations were made by PRESTO. The data was reconstructed using Ordinary Poisson Ordered Subset Expectation Maximization (OPOSEM) (J. J. Scheins et al. 2011). The images were reconstructed with 41 iterations because it is the value normally used in FZJ.

The next table (Table 4. 2) shows some important information about Utah data such as statistics and matrix and voxel sizes.

Table 4. 2: Dataset Utah information.

Datasets	Statistics (counts)	Matrix Size	Voxel Size (mm)
Simulated Utah Phantom	1.00E6	256 x 256 x 153	1.25
	2.25E7		
	1.00E9		

The Utah phantom is a cylinder that contains various compartments and each compartment has independent access. However emphasis is given only two cylindrical compartments that were filled with different radioactivity concentration (see Figure 4. 6 D and E compartments), one with greater and the other with less than the surrounding region (compartment B). The activity proportion is 5:1:0.2. In this case, the compartments were not truly filled because the images were simulated and not acquired from a real phantom.

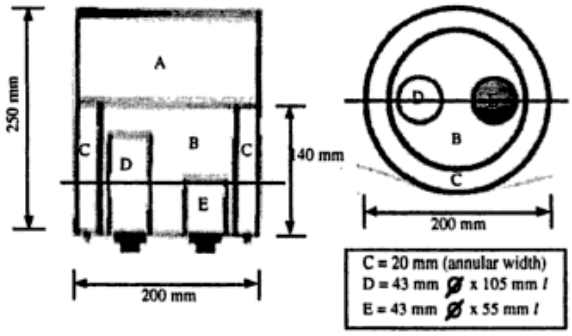

Figure 4. 6: Scheme of Utah phantom (Bendriem & Townsend 1998).

4.3.3. Brain phantom

A simulated brain phantom was used in almost all the tests performed in this thesis work. As the Utah phantom, it was simulated using PRESTO. An Ordinary Poisson Ordered Subset Expectation Maximization (J. J. Scheins et al. 2011) was used in the reconstruction. The data was simulated analytically with different statistics. Scatter and random fractions were both 35% with respect to true detected events.

Two different datasets of brain phantoms were simulated: one of PET, dynamic [18F]-FDG data, and one of MRI, FLASH sequence data.

The dynamic dataset has 23 frames as applied in the clinical protocol in FZJ center: 8x5s; 2x10s; 2x15s; 1x30s; 1x60s; 1x120s; 5x300s; 3x600s. Figure 4. 7 shows the frame 23 of the brain phantom.

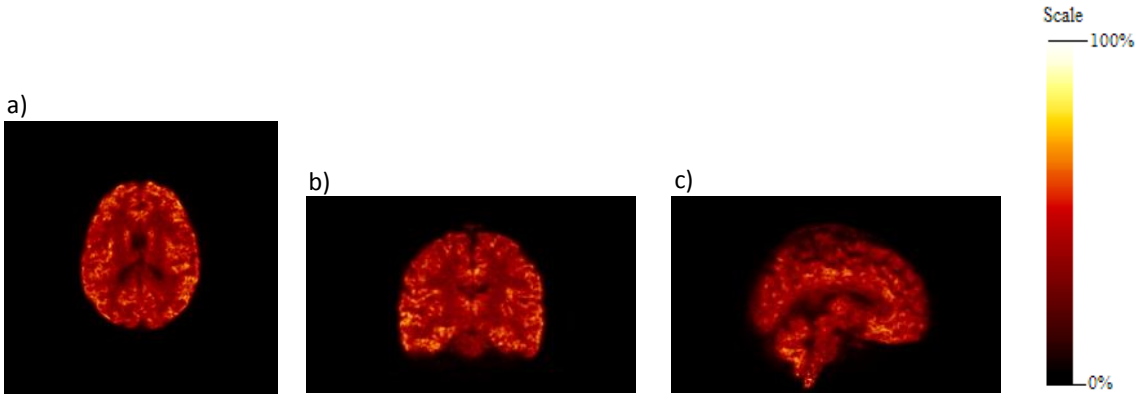

Figure 4. 7: [18]-FDG Brain phantom (frame 23): a) transversal, b) coronal and c) sagittal view.

The time activity curve of arterial input function and white and grey matters are shown in Figure 4. 8. The total number of true counts was set to 600 million (for one hour acquisition).

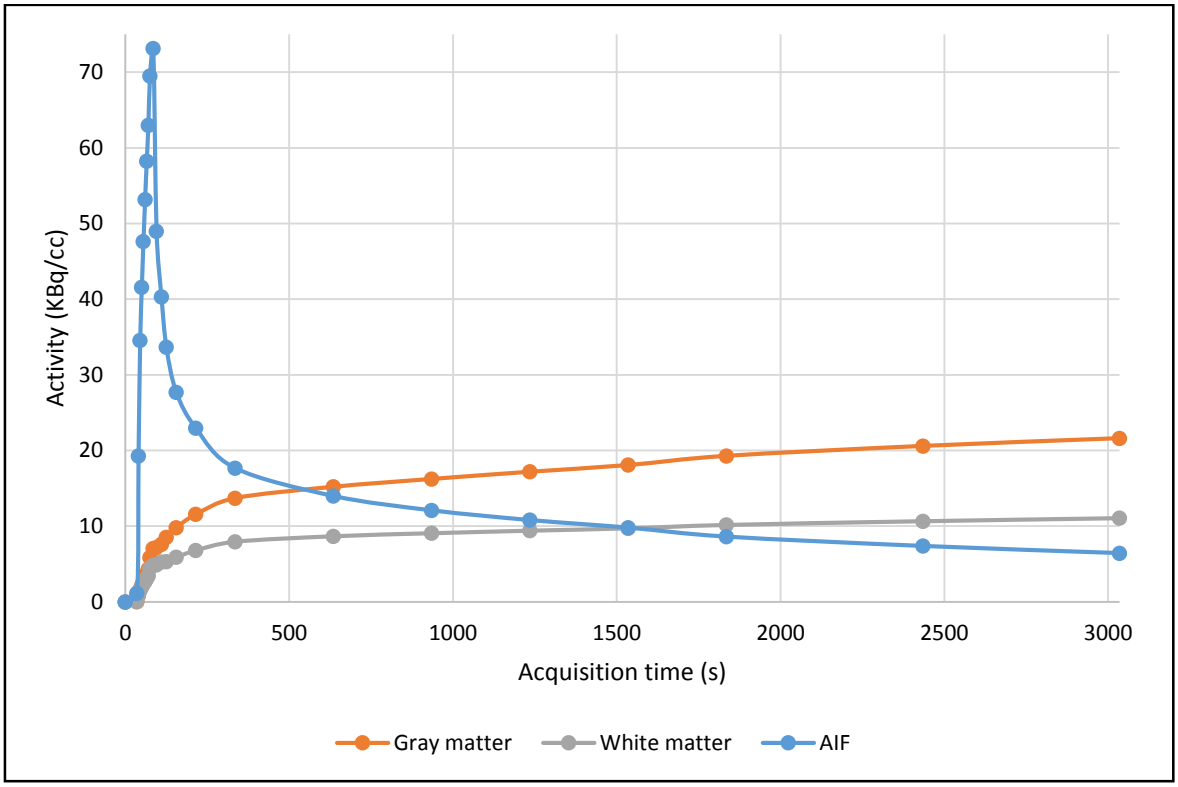

Figure 4. 8: Time activity curve of the brain phantom dynamic dataset. Arterial input function and gray and white matter were shown.

Table 4. 3 shows some important information about the simulated dynamic data such as statistics and matrix and voxel sizes. The dynamic frames were simulated with 11 and 41 iterations.

Table 4. 3: Dynamic [18F]-FDG datasets information.

Datasets	Frames	Frames Duration (s)	Statistics (counts)	Matrix Size	Voxel Size (mm)
Brain phantom images	Frame 1	5	4.06E3	256 x 256 x 153	1.25
	Frame 2	5	7.68E4		
	Frame 3	5	1.43E5		
	Frame 4	5	1.81E5		
	Frame 5	5	2.17E5		
	Frame 6	5	2.52E5		
	Frame 7	5	2.88E5		
	Frame 8	5	3.23E5		
	Frame 9	10	8.20E5		
	Frame 10	10	9.45E5		
	Frame 11	15	1.29E6		
	Frame 12	15	1.30E6		
	Frame 13	30	2.77E6		
	Frame 14	60	6.11E6		
	Frame 15	120	1.40E7		
	Frame 16	300	4.03E7		
	Frame 17	300	4.40E7		
	Frame 18	300	4.65E7		
	Frame 19	300	4.87E7		
	Frame 20	300	5.09E7		
	Frame 21	600	1.08E8		
	Frame 22	600	1.14E8		
	Frame 23	600	1.19E8		

A MR image (transversal, coronal and sagittal views) from the FLASH sequence data is shown in Figure 4. 9 and some information about this sequence is described in Table 4. 4. More detail information about the simulation can be found in Brainweb (Aubert-Broche et al. 2006) (Kwan et al. 1996).

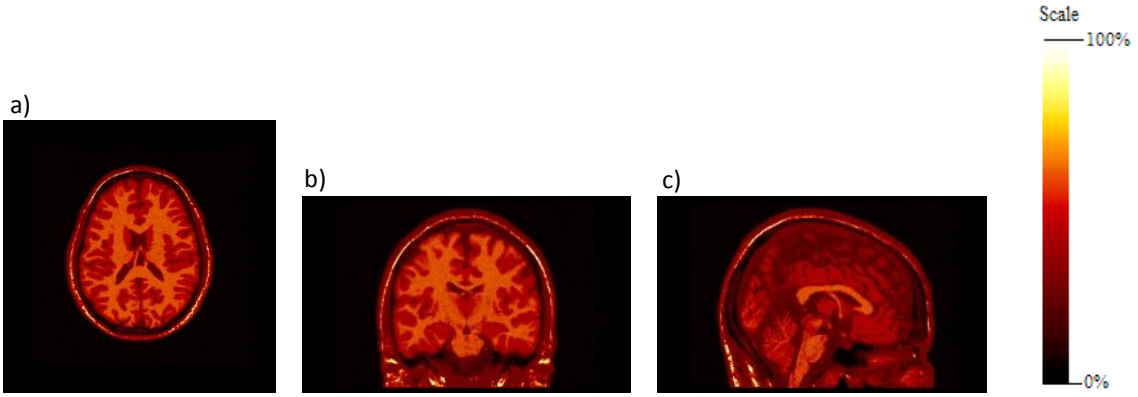

Figure 4. 9: Simulated brain phantom: FLASH sequence image. a) transversal, b) coronal and c) sagittal views.

Table 4. 4: FLASH sequence information.

Datasets	Matrix Size	Voxel Size (mm)	Description
FLASH Image – MRI	256 x 256 x 153	1.25	Flip Angle: 30º TE: 10 ms TR: 18 ms

4.3.4. FDG and EPI clinical images

Clinical images of healthy volunteer were used on some studies throughout the thesis: [18F]-FDG image (PET) and EPI image (MR). Relatively to [18F]-FDG data, the volunteer was administrated with 310 MBq and the acquisition took about 35 min (96 min p.i.). The volunteer data was also reconstructed using OPOSEM. The EPI sequence was acquired with a temporal resolution of 2,220 seconds (Ullisch et al. 2012). The reconstructed PET image has a flat format while MR image has DICOM format. These two images belong to the same patient.

Information about the clinical images, PET and MR, is described in Table 4. 5.

Table 4. 5: Information about the clinical images, [18F]-FDG and EPI images.

Datasets	Matrix Size	Voxel Size (mm)	Description
Clinical Images – [18F]-FDG	256 x 256 x 153	1.25	Number of frames:12 Duration: 60s Statistics:
Clinical Images – EPI	64 x 64 x 45	3.70	Flip Angle: 80 ° TE: 30 ms TR: 2,220 ms GRAPPA Factor: 4

4.3.5. Patient images

Datasets from five different exams were used on the final study: [18F]-FDG, [18F]-FET, [11C]-Raclopride, [11C]-Flumazenil, [15O]-Water. For each exam was analyzed two different patients. These acquisition were made in the Siemens 3TMR-BrainPET scanner at FZJ. Information about these exams is represented in Table 4. 6. However information about their datasets such as matrix and voxel sizes, total number of frames and respective reference frame used in thesis are shown in Table 4. 7.

Table 4. 6: Information about the acquired data from five different exams.

Exam	Volunteer	Inj. Activity (MBq)	Exam duration (min)
[11C]-Flumazenil	1	394	100
	2	408	
[11C]-Raclopride	1	175	60
	2	186	
[18F]-FET	1	220	60
	2	191	
[18F]-FDG	1	189	60
	2	194	
[15O]-Water	1	538	20
	2	537	

Table 4. 7: Information about the ten datasets (two dataset from each exam).

Exam	Volunteer	Matrix Size	Voxel Size (mm)	Total number of frames
[11C]-Flumazenil	1	256 x 256 x 153	1.25	10
	2			
[11C]-Raclopride	1	256 x 256 x 153	1.25	12
	2			
[18F]-FET	1	256 x 256 x 153	1.25	16
	2			
[18F]-FDG	1	256 x 256 x 153	1.25	14
	2			23
[15O]-Water	1	256 x 256 x 153	1.25	30
	2			

4.4. Performed Tests

Several tests were performed during this work to test the viability and versatility of the ITK motion estimation. They are briefly described below and more information can be find in the next chapter (Chapter 5).

4.4.1. Volunteer MPRAGEs

MPRAGE images of volunteers were used to check the maximum range of motion inside the BrainPET head coil. The volunteers were asked to stay still during the sequences. Nevertheless they changed the head position between sequences. Two volunteers did four different positions of motions (head up, head down, head rotated to the right and to the left around the z-axis), however the third volunteer did two more motions (head rotated to the right and to the left around the x-axis). Figure 4. 10 shows the representation of these axes in relation of the body planes. Figure 4. 11 represents the four types of motion made by the three volunteers and Figure 4. 12 shows the additional two motions made only by the third volunteer. The first acquisition was always the image used as reference image (head in the normal/standard position). In order to avoid the influence of the first positions, the acquisition order of the different motions for all the three volunteers was different.

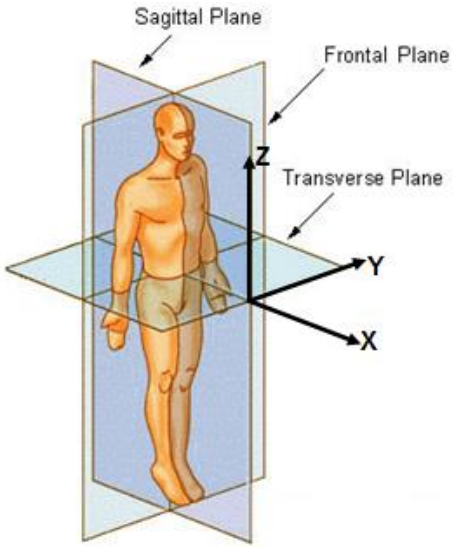

Figure 4. 10: Body planes and allocentric reference frame (Courreges 2011).

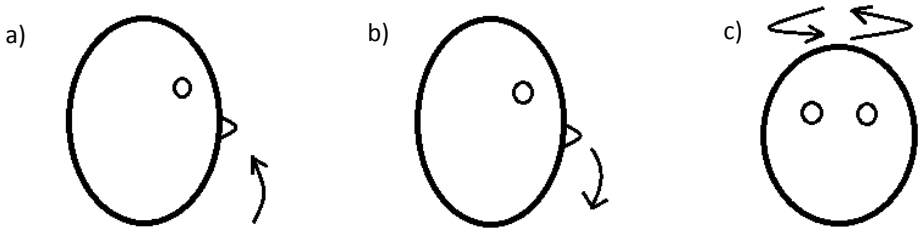

Figure 4. 11: Volunteers motions: a) head up, b) head down, c) head rotated to the right and to the left around z-axis.

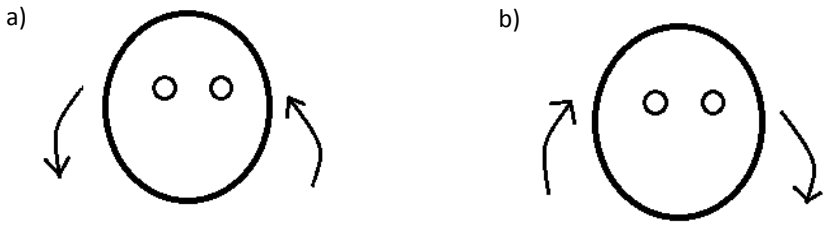

Figure 4. 12: Additional volunteer motions: a) head rotated to the right and b) to the left around x-axis.

For this analysis MPRAGE images were chosen because they have an excellent resolution and the brain structures were very well defined. As ITK estimates the motion using the image, these type of image can help to estimate the different motions and then correct them. MPRAGE sequences are widely used in clinical practice. Therefore this study can be also used to show that ITK motion estimation can be used in real data.

4.4.2. Simulated data

Simulated images from Utah and brain phantoms were used in almost all studies throughout this thesis. Furthermore PET ([18F]-FDG) and MR (EPI) images were also used. Using a PRESTO script, four different motions were applied to the images: 1 mm and 1º; 5 mm and 5º, 10 mm and 10º; and 30 mm and 30º. The motions were estimated by ITK and PMOD. A Gaussian filter with sigma = 6 mm was applied to all the images before the motion was estimated. The filtering is used to reduce the image noise i.e. improve the signal-to-noise (Yoshida et al. 2012) and, therefore, to decrease the motion parameters errors calculated by ITK. The Gaussian filter with sigma = 6 mm was chosen because it is used in 3D clinical studies for motion correction at FZJ using PMOD. An additional comparison between filtered and unfiltered images was made to confirm the importance of the filtering in motion estimation.

4.4.2.1. Evaluation of estimation

A quantitative analysis is essential to evaluate the motion estimation and for that absolute errors sums of translation and rotation were calculated for all simulated cases:

$$\sum Error = \sum |m_s - m_e| \tag{13}$$

m_s is the simulated motion and m_e the estimated motion (ITK and PMOD output).

The sums consider the errors in x, y and z axes. These calculations were possible to perform because the motion was simulated and hence the motion is known. This evaluation of motion estimation was made in most performed tests in this work. The motion was corrected applying the inverse transform in the moved images using PRESTO. The inverse transform parameters correspond to ITK or PMOD output motion parameters.

4.4.2.2. Influence of statistics

PET images can have different statistics and the influence of that in motion estimation using ITK was also studied. The image quality is directly influenced by the statistics. Higher the statistics, lower is the noise level of the images. Hence it is expected that the motion parameters estimated by ITK are different when images with different statistics are used. [18F]-FDG images from Utah and brain phantoms with different statistics were used. In all these images, four simulated motions of 1 mm and 1º; 5 mm and 5º; 10 mm and 10º; and 30 mm and 30º were applied. A comparison between the translation and rotation error sums of images with different statistics was made. Using

ITK output, the motions were corrected by a script of PRESTO. A visually comparison between reference and moved images and the respective corrected image was also made.

4.4.2.3. Influence of number of iterations

The influence of image reconstruction iterations on motion estimation is also analyzed in this thesis because it is a flexible variable and it is important to know if ITK is able to estimate the motion using images with different number of iterations and which works better. Two different numbers of iterations, which correspond to a different convergence levels of reconstructions, were used: 11 and 41. These two numbers of iterations were used in studies at FZJ. Frames 5, 11, 17 and 23 of dynamic [18F]-FDG data were used for the comparison. In this study the motions were not corrected only estimated and then the absolute errors sums (of translation and rotation) were calculated and compared. It is expected that reconstructed images with a different number of iterations are different because this number introduces different levels of noise and bias in the image. As ITK is an image-domain method for motion correction, any difference in the image can influence the motion estimation error. Therefore this parameter can be used to achieve more accurate parameters of motion.

4.4.2.4. Estimation using PET and/or MR images

Clinical images of the same volunteer, [18F]-FDG and EPI, were used to evaluate the versatility of ITK motion estimation. In other words, the study has the aim to verify if this software can be used to correct the motion of real data from two different modalities (PET and MRI) or not. At the same time a comparison between these two imaging modality was made to check if the absolute errors were very different of each other. In a PET/MRI context, the motion parameters of one-modality image can be used to correct the image from the other modality. In each image, all four motions were also simulated by PRESTO: 1 mm and 1º; 5 mm and 5º; 10 mm and 10º; and 30 mm and 30º.

Using ITK for motion estimation it is necessary images with interfile format. However EPI images have DICOM format and PET images have flat format. Therefore conversion programs were implemented (*Matlab* script).

4.4.2.5. Choice of reference frame

In real dynamic data it is necessary to choose a reference image to correct the others frames that are affected by motion. In the previous studies the reference and the moved image is the same, i.e. the motion was simulated on the reference image, but in clinical practice this is impossible. The analysis focus in studying the importance to choose the best frame as reference and the impact of this choice in motion estimation. First, a comparison between using the same frame as reference and moved image and using the frame 13 (one of the middle frames from dynamic brain phantom data) as reference image to correct the others frames was made. A second comparison was performed between using the frame 13 and the frame 23 (frame with highest statistics) as reference frame. Here the moved image used was the frame 16. Finally to reinforce the importance of the reference frame, it was calculated the absolute error sums of using the frame 13 as reference and frame 23 as moved and vice-versa.

4.4.2.6. Choice of metrics

In the previous studies the Normalized Correlation ITK metric was the only metric used. However this metric may not be the best to solve this problem. ITK has several available metrics and three of them were compared in this work: Mutual Information, Normalized Correlation and Mean Squares. Two different values of the parameter *Set Number of Spatial Samples* on Mutual Information metric, 10 000 and 200 000, were also tested. This analysis has the aim to check the better metric i.e. check if it is possible to get smaller translation and rotation error sums than the previous results. Two metric comparisons were made. First, the reference and moved images from the same modality were used separately: [18F]-FDG of brain phantom and EPI clinical images. These types of images were chosen because one is a PET image and the other is a MR image. At the same time one is from a phantom and other from a volunteer. Posteriorly a comparison using multi-modality images to motion estimation was performed. Image from the FLASH sequence and [18F]-FDG image (frame 23 of dynamic data) were the chosen images for this last analysis.

4.4.2.7. Comparison of PMOD and ITK

PMOD is a viable software used in FZJ to correct the motion. A comparison between PMOD and ITK was made to test the viability of the ITK motion estimation and to know if it can replace PMOD in FZJ. Several datasets were used in this study: simulated Utah and brain phantoms, clinical PET and EPI images. The three ITK metrics (normalized correlation, mutual information and mean squares) were compared with PMOD. The PMOD metric is the Mean Squares. The

translation and rotation errors sums using PMOD and ITK were calculated and then compared. The PMOD output consists in affine transforms, therefore some calculations were required to find out the translation and rotation motions with respect to the Cartesian axis (Euler angles).

4.4.2.8. Influence of attenuation map

After the attenuation map (spatial distribution of the attenuation coefficient) is determined, it is projected into a sinogram form and applied to the PET emission data during the image reconstruction process, correcting the PET emission sinogram data. Therefore the attenuation corrected PET sinogram is reconstructed to obtain the corrected PET images. Hence different attenuation coefficient can originated different images. For this reason, the influence of attenuation correction in the presence of motion was also studied. Frame 22 and 23 from dynamic [18F]-FDG brain phantom data were used. 1 mm of translation and 1º of rotation on all the three axes (at the same time) were simulated. Three different images from each frame were tested: image with the correct attenuation map (map with the simulated motion), images with the wrong attenuation map (map without the simulated motion) and images without attenuation correction. The motion was estimated using PMOD and ITK and then the two software outputs are compared by absolute error sums. The ITK metric used was Normalized Correlation.

4.4.3. Acquired data

^{11}C, ^{15}O and ^{18}F are radionuclides used in PET brain imaging to locate epileptic focus and for dementia, psychiatry and neuropharmacology studies. ^{11}C and ^{18}F can be used to label the sugar glucose, which is the only energy source of the brain, while ^{15}O can be used to label water molecules, which can help measure blood flow in brain. In this study, five different exams which are routinely made in the Siemens 3T MR-BrainPET at FZJ were used: [18F]-FDG, [18F]-FET, [11C]-Raclopride, [11C]-Flumazenil, [15O]-Water. Images from two patients of each PET/MR exam were studied. The motion was estimated by the ITK metric Normalized Correlation and PMOD and then compared. As the range of motion is unknown it is not possible to calculate the error between the real motion and the estimated motion. Therefore the quantitative analysis of absolute translation and rotation error sums, in this study, was made comparing the motion parameters of ITK output with the parameters of PMOD output. This analysis was made to confirm if ITK can be used in clinical practice for different types of exams at FZJ.

CHAPTER 5

Results and Discussion

In the chapter 5, the results and respective discussion of all performed tests described in chapter 4 are presented.

5.1. Volunteer MPRAGEs

MPRAGE images of three volunteers were used to check maximum range of motion inside the BrainPET head coil in different positions. The motion of the head was blocked with a tape that passes over the volunteer forehead and is stuck from one side to the other of the coil. Additionally, for the second and third volunteers, it was used sponge around the head to fill in the empty spaces also blocking the head motion. The volunteers were still during the sequences keeping the head in the same position and they changed the head position between sequences. Each MPRAGE sequence took around 5 minutes of acquisition, so for the volunteers is not difficult to stay still during the sequences acquisition.

In clinical practice an average of the first frames were used as reference to correct the motion of the other ones. Therefore for this study the reference image, which represent the position without motion (head in normal/standard position), is the first position in acquisition. At the same time the first motions can influence the following ones and then the reference position is no longer really head in standard position.

All three volunteers did not make the same positions and the positions order was different during the protocol. As previous mentioned, different position orders avoid that the first motions influences in the same way the last ones and then the last positions do not have the same viability than the first positions. The third volunteer performed two more position than the other two. This happened because the acquisition of the third volunteer was made in a different day.

Two volunteers experienced four types of motion: head up, head down, head rotated to left and to the right around z-axis considering the Cartesian axis represented in Figure 4. 10 and, as previously stated, the third volunteer did two more movements: head rotated to left and right around the x-axis. The different movements acquisition orders are represented in Table 5. 1.

Table 5. 1: Movements acquisition orders of the three volunteers.

First Volunteer	Second Volunteer	Third Volunteer
Head in standard position	Head in standard position	Head in standard position
Head up	Head rotated to the right (z-axis)	Head rotated to the right (z-axis)
Head down	Head rotated to the left (z-axis)	Head rotated to the left (z-axis)
Head rotated to the right (z-axis)	Head down	Head rotated to the right (x-axis)
Head rotated to the left (z-axis)	Head up	Head rotated to the left (x-axis)
-	-	Head up
-	-	Head down

The Figure 5. 1 to Figure 5. 6 show the six examples of motion listed above in different volunteers.

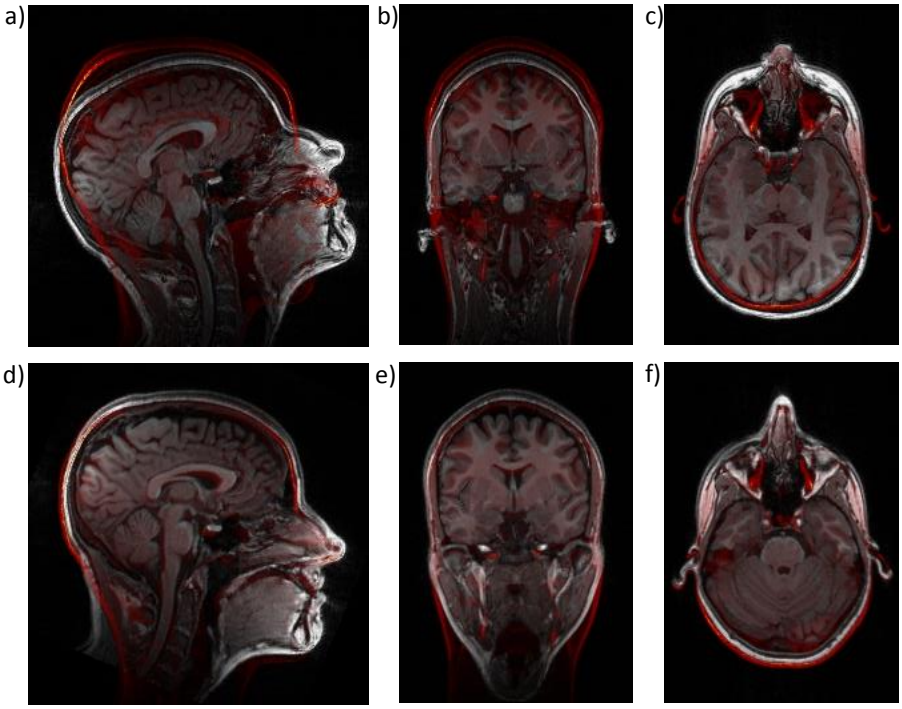

Figure 5. 1: MPRAGE images (volunteer 1). The first row (a), b) and c)) shows overlaid images without and with motion (head up). The image without motion is in hot metal color and the image with motion is in grey scale. The second row shows the overlaid image without motion (reference image) and the corrected image. The image without motion is in hot metal color and the correct image is in grey scale. a) and d) transversal, b) and e) coronal, and c) and f) sagittal views. As ITK metric, Normalized Correlation was used.

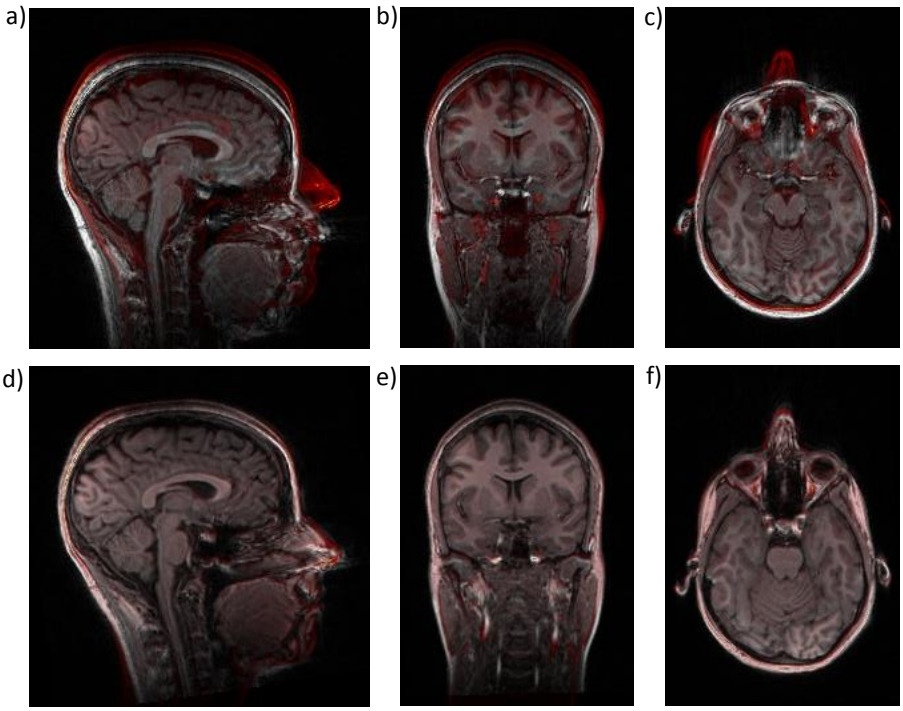

Figure 5. 2: MPRAGE images (volunteer 1). The first row (a), b) and c)) shows overlaid images without and with motion (head down). The image without motion is in hot metal color and the image with motion is in grey scale. The second row shows the overlaid image without motion (reference image) and the corrected image. The image without motion is in hot metal color and the correct image is in grey scale. a) and d) transversal, b) and e) coronal and c) and f) sagittal views. As ITK metric, Normalized Correlation was used.

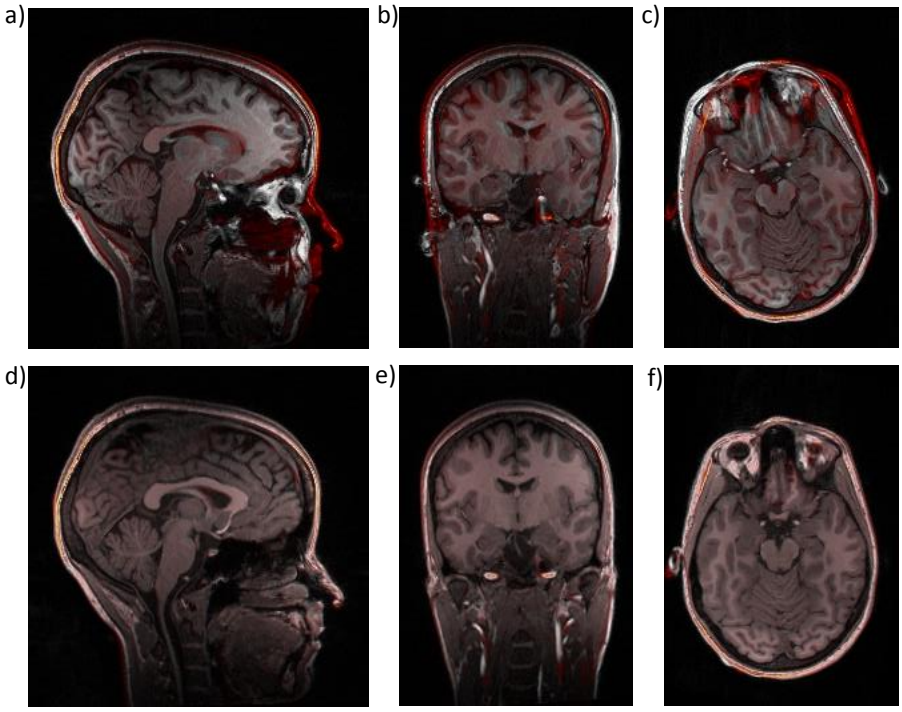

Figure 5. 3: MPRAGE images (volunteer 2). The first row (a), b) and c)) shows overlaid images without and with motion (head rotated to the right around z axes). The image without motion is in hot metal color and the image with motion is in grey scale. The second row shows the overlaid image without motion (reference image) and the corrected image. The image without motion is in hot metal color and the correct image is in grey scale. a) and d) transversal, b) and e) coronal and c) and f) sagittal views. As ITK metric, Normalized Correlation was used.

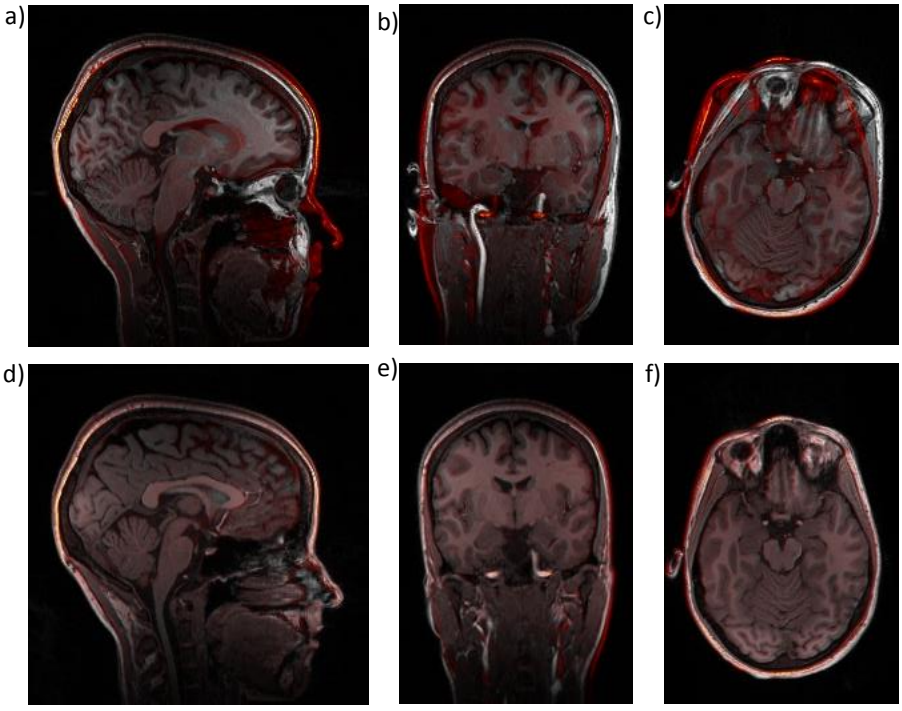

Figure 5. 4: MPRAGE images (volunteer 2). The first row (a), b) and c)) shows overlaid images without and with motion (head rotated to the left around z axes). The image without motion is in hot metal color and the image with motion is in grey scale. The second row shows the overlaid image without motion (reference image) and the corrected image. The image without motion is in hot metal color and the correct image is in grey scale. a) and d) transversal, b) and e) coronal and c) and f) sagittal views. As ITK metric, Normalized Correlation was used.

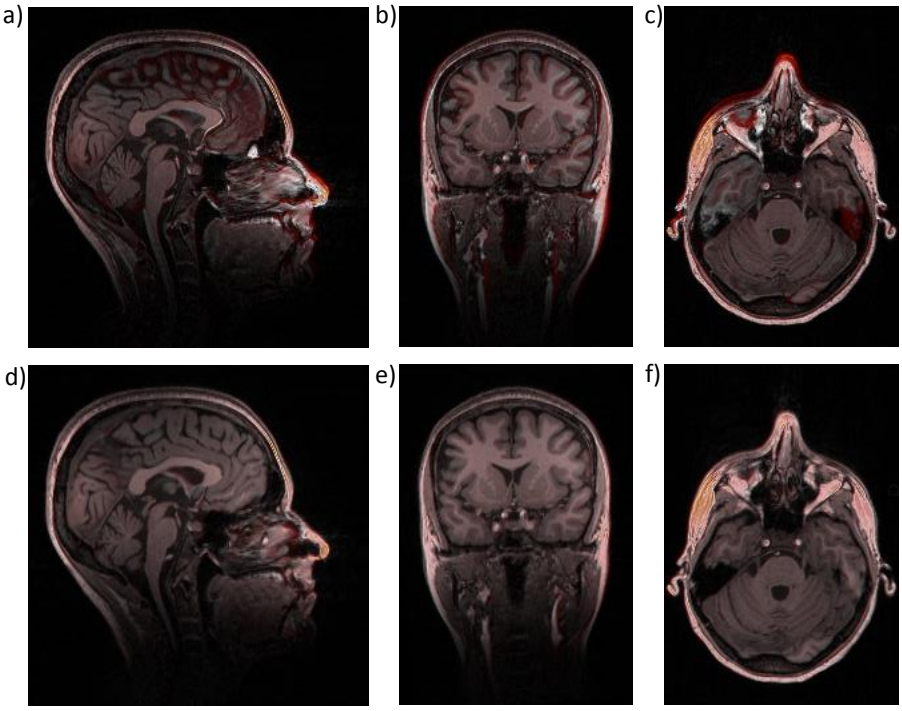

Figure 5. 5: MPRAGE images (volunteer 3). The first row (a), b) and c)) shows overlaid images without and with motion (head rotated to the right around x axes). The image without motion is in hot metal color and the image with motion is in grey scale. The second row shows the overlaid image without motion (reference image) and the corrected image. The image without motion is in hot metal color and the correct image is in grey scale. a) and d) transversal, b) and e) coronal and c) and f) sagittal views. As ITK metric, Normalized Correlation was used.

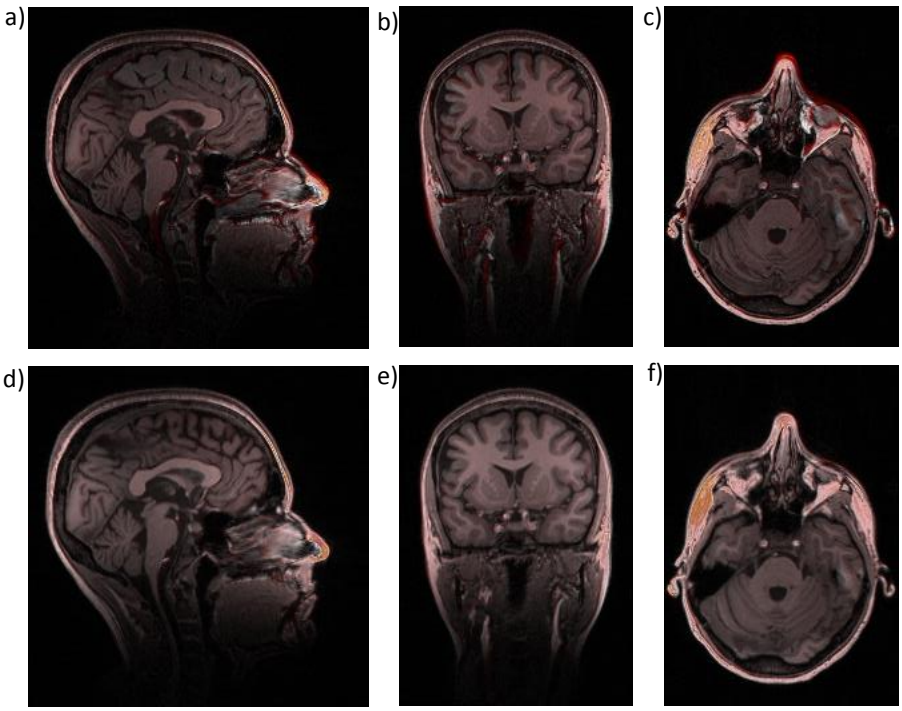

Figure 5. 6: MPRAGE images (volunteer 3). The first row (a), b) and c)) shows overlaid images without and with motion (head rotated to the left around x axes). The image without motion is in hot metal color and the image with motion is in grey scale. The second row shows the overlaid image without motion (reference image) and the corrected image. The image without motion is in hot metal color and the correct image is in grey scale. a) and d) transversal, b) and e) coronal and c) and f) sagittal views. As ITK metric, Normalized Correlation was used.

Figure 5. 1 and Figure 5. 2 correspond to the first volunteer, Figure 5. 3 and Figure 5. 4 to the second and the last two figures (Figure 5. 5 and Figure 5. 6) correspond to the third volunteer. The first row of each figure represents two overlaid images: fixed and moved image. The second row also represents two overlaid images: fixed and corrected image. As previously described the corrected images are obtain by applying the inverse transform in the moved image (using PRESTO) and the parameters of this transform are estimated by ITK. Using overlaid images with different colors makes it possible to distinguish the motions from the reference and the corrected images. The three views (transversal, coronal and sagittal) are shown since there are motions which are not visible in all views.

The motion in the first two figures was bigger than the other four. In the next two figures (Figure 5. 3 and Figure 5. 4), a considerable head motion can also be seen. However the last volunteer did not experience a big motion, therefore the motion in Figure 5. 5 and Figure 5. 6 are hardly noticeable. In the last rows of the six figures it can be observed that the reference image and the corrected image are coincident, being impossible to visually distinguish the image in the hot metal color scale from the grey scale image. This is true for large or small motions. In a qualitative analysis it can be concluded that ITK is able to estimate the head motion, regardless of the motion range, and the PRESTO script can be used to apply the inverse transform in the moved image.

ITK presents several metrics to estimate the motion. However here only one was used: Normalized Correlation. The choice of the metric was based in the type of image used in this study, one-modality. A quantitative analysis of the motions cannot be made because the exact range of motions was unknown. As already mentioned, the aim of this experience is to check the maximum range of motion. All the motions of the three volunteers inside the BrainPET head coil are registered in Table 5. 2.

Table 5. 2: Motion extensions inside the BrainPET scanner from three volunteers.

Volunteers	Motions	Translation (mm)			Rotation (º)		
		X-axis	Y-axis	Z-axis	X-axis	Y-axis	Z-axis
Volunteer 1	Head up	**12.35**	3.19	0.79	0.41	0.03	**23.14**
	Head down	10.76	**3.95**	1.83	1.83	1.40	8.29
	Head rotated to the right (z-axis)	10.72	2.69	0.25	5.14	**8.49**	3.07
	Head rotated to the left (z-axis)	9.68	2.74	1.71	4.76	2.72	3.69
Volunteer 2	Head up	5.35	3.06	0.75	1.63	0.06	9.07
	Head down	0.45	1.98	0.59	1.56	0.22	9.73
	Head rotated to the right (z-axis)	1.71	1.41	4.82	10.58	3.87	0.74
	Head rotated to the left (z-axis)	0.50	0.54	**6.81**	**16.88**	1.44	1.69
Volunteer 3	Head up	1.95	0.15	0.15	0.03	0.21	3.92
	Head down	1.32	1.30	0.29	0.82	1.30	3.49
	Head rotated to the right (z-axis)	0.14	0.18	1.57	4.09	1.44	0.37
	Head rotated to the left (z-axis)	0.18	0.39	1.28	2.89	1.38	0.95
	Head rotated to the right (z-axis)	0.99	0.79	0.18	1.20	3.13	1.50
	Head rotated to the left (z-axis)	0.55	0.70	0.40	0.31	1.92	1.04

Of all the motions recorded in Table 5. 2, the average and the maximum motions inside the head coil were summarized in Table 5. 3 and Table 5. 4 respectively. These motions correspond to translation and rotation on three cardinal axes (x, y and z).

Table 5. 3: Average of all the performed motions inside the BrainPET scanner.

	X-axis	Y-axis	Z-axis
Translation (mm)	4.05	1.65	1.53
Rotation (º)	3.72	1.97	5.05

It can be noticed that the motion average in rotation is higher than in translation with respect to y- and z- axis. Nevertheless, in y-axis, the difference between the two (translation and rotation) is the smallest. According to Table 5. 3 the average of motion in translation is between 1 and 2 mm, however in x-axis the motion average is 4 mm, which is about the double of the other two. Comparing the three axes, the motion average in rotation is more inconsistent. The bigger range of motion was observed in rotation around the z-axis, 5.05º, and the smaller one was observed in translation also in z-axis, 1.53 mm. The motion outliers were observed in x- and z-axis. Perhaps it is more difficult to move along y-axis when the volunteer is taped. This outliers may have influenced the motion averages which are represented in the previous table.

Table 5. 4: Maximum extensions of motion inside the BrainPET scanner.

	X-axis	**Y-axis**	**Z-axis**
Translation (mm)	12.35	3.95	6.81
Rotation (º)	16.88	8.50	23.14

The maximum motion that the volunteers could experience inside the coil was about 12 mm of translation in x-axis and 23º of rotation in z-axis. These two values are made by the same volunteer in the same position (first volunteer - head up). The rotation is considered very large, but this volunteer had not properly secured its head, the tape was not stuck and the sponge around its head and neck was not used. Because of that the volunteer had a lot of space to move its head. The maximum motions were not always experienced by the first volunteer, two of them were experienced by the second volunteer. The third volunteer did not contribute for any maximum motion. This is maybe because he was trapped in a different way. Therefore the motion is influenced by the way that the patient is taped and if he is comfortable. In clinical practice the sponge around the head is not used, only the tape.

These translation and rotation maximum motion with respect to all the axes were helpful to choose the motion range tested throughout this thesis.

5.2. Simulated data

Two simulated phantoms (Utah and brain phantom) and two clinical images ([18F]-FDG and EPI) were used to test the versatility of ITK motion estimation. At first, it is important to used simulated

data because it is easier to understand the results. Thereafter clinical images, which are more complex ones, have to be test to kwon if the ITK can be used in studies using real data or even in clinical practice. All these images were reconstructed with 41 iterations.

After knowing the maximum ranges of motion inside the head coil, it was decided to simulate four types of motion in the next studies throughout the thesis: 1 mm and 1º; 5 mm and 5º; 10 mm and 10º; and 30 mm and 30º. All these motions were simultaneously applied on x, y and z axes because in MPRAGE images it could be observed that one simple motion in one axis affects all the axes in rotation and translation. Motion range of 30 mm and 30º is very large but it was decided to use this motion because it is necessary to test the robustness of the method. This motion range can only be achieve if the patient is not properly secure and usually it does not happen in clinical practice.

Figure 5. 7 shows the reference image (image without motion) and the images with the simulated four motions. These images are from Utah phantom and they were analyzed because it is important to know the consequence of these motions in the image in order to better understand the future results. Motion such as 1 mm and 1º cannot be visually recognized (Figure 5. 7 a)-c)). However when 5º and 5 mm were simulated the motion can already be seen in the Figure 5. 7 d)-f). As the motion is not large, the FOV continues to cover the entire phantom. Contrariwise when 10 mm and 10º of motion were simulated, a small part of the phantom moved out the FOV (Figure 5. 7 k)) and finally when 30 mm and 30º were simulated a significant part of the phantom moved out of the FOV in all represented views. In Figure 5. 7 n) and o) it is impossible to distinguish the two cylinders of the phantom. Larger the motion higher the possibility of the phantom going out of the field of view. As ITK estimate the motion using the images, the results can be severely affected when the phantom moves out the FOV.

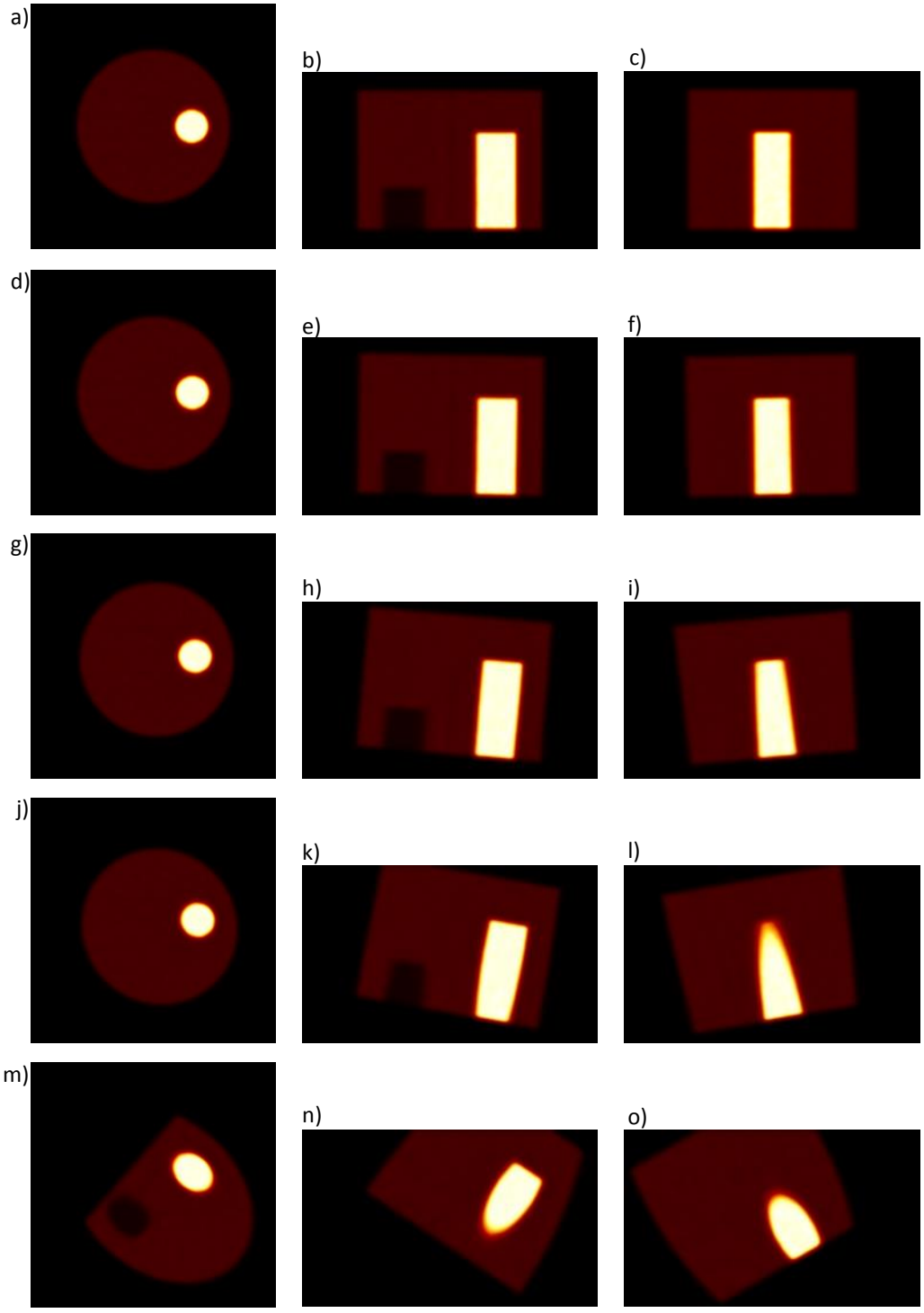

Figure 5. 7: Simulated images of Utah phantom (statistic of 1.00E9 counts). Phantom PET images without motion (reference image): a) transversal, b) coronal and c) sagittal view. d), e) and f) show the simulated images with a translational motion of 1 mm and rotation of 1° with respect to all three axes. g), h) and i) are images with motion of 5 mm and 5°. j), k) and l) are images with motion of 10 mm and 10° and finally in m), n) o) are represented images with 30 mm and 30° of motion with respect to three axes.

A Gaussian filter with sigma = 6 mm was applied in all the images before the motion estimation. While PMOD applies the filter automatically, ITK does not. Therefore a script in *Matlab* was used. The chosen filter was the Gaussian filter with sigma = 6 mm, because it is the filter used in

3D clinical studies in FZJ. In order to know the importance of the filter in motion estimation, a comparison between the absolute error sums of unfiltered and filtered images was made. For this, all [18F]-FDG dynamic data from brain phantom were used in the study, however only the results of two frames were shown: frame 4 (20 s after the acquisition start) and frame 10 (1 min after the acquisition start). All the four motions were considered: 1 mm and 1º; 5 mm and 5º; 10 mm and 10º; 30 mm and 30°. In Table 5. 5 the difference between filtered and unfiltered images was quantified comparing their errors.

Table 5. 5: Translation and rotation error sums from brain phantom motion estimation. Difference between filtered and unfiltered images were shown.

Frames (statistics in counts)	**Motions (° and mm)**	**Unfiltered Images**		**Filtered Images**	
		Translation Error Sum (mm)	Rotation Error Sum (°)	Translation Error Sum (mm)	Rotation Error Sum (°)
Frame 4 (1.81E5)	1	2.78	2.60	**1.26**	**1.35**
	5	3.67	14.72	**1.49**	**2.19**
	10	6.24	29.93	**2.53**	**4.59**
	30	18.62	89.93	**10.28**	**81.80**
Frame 10 (9.44E5)	1	**0.55**	2.49	1.01	**1.67**
	5	3.53	14.65	**1.69**	**2.45**
	10	4.95	29.88	**3.39**	**4.85**
	30	16.09	89.90	**13.71**	**76.04**

According to Table 5. 5 it can be concluded that, in motion correction, the absolute errors are generally smaller when filtered images are used. This is true for translation and rotation, independently of the image statistics. Even using large motions (30 mm and 30°) the behavior was the same, however when unfiltered images were used the motion in rotation was not detected by ITK (99% error). Generally the results are better after applying the Gaussian filter because the image gets less noisy. The noise can cover and reduce the visibility of certain features within the image which occurs especially in low contrast objects. When the noise is reduced these low contrast objects, generally, became visible. In translation the difference of the error sums, using filtered or unfiltered images, was smaller in frame 10 than frame 4. This is because the frame 10 has less noise than frame 4, so less noise was filtered and then the difference is narrower. Therefore image-domain motion correction methods benefits from noise reduction i.e. more accurate motion parameters can to be estimated.

In Figure 5. 8 it can be seen the importance of applying the filter. Here is shown one image (frame 3) without and with filter. Smaller the image statistics higher the difference between filtered and unfiltered image. In the image without filter only some intensity points in a black background are presented and the brain cannot be easily recognized. Visually, the filtered image has much less noise.

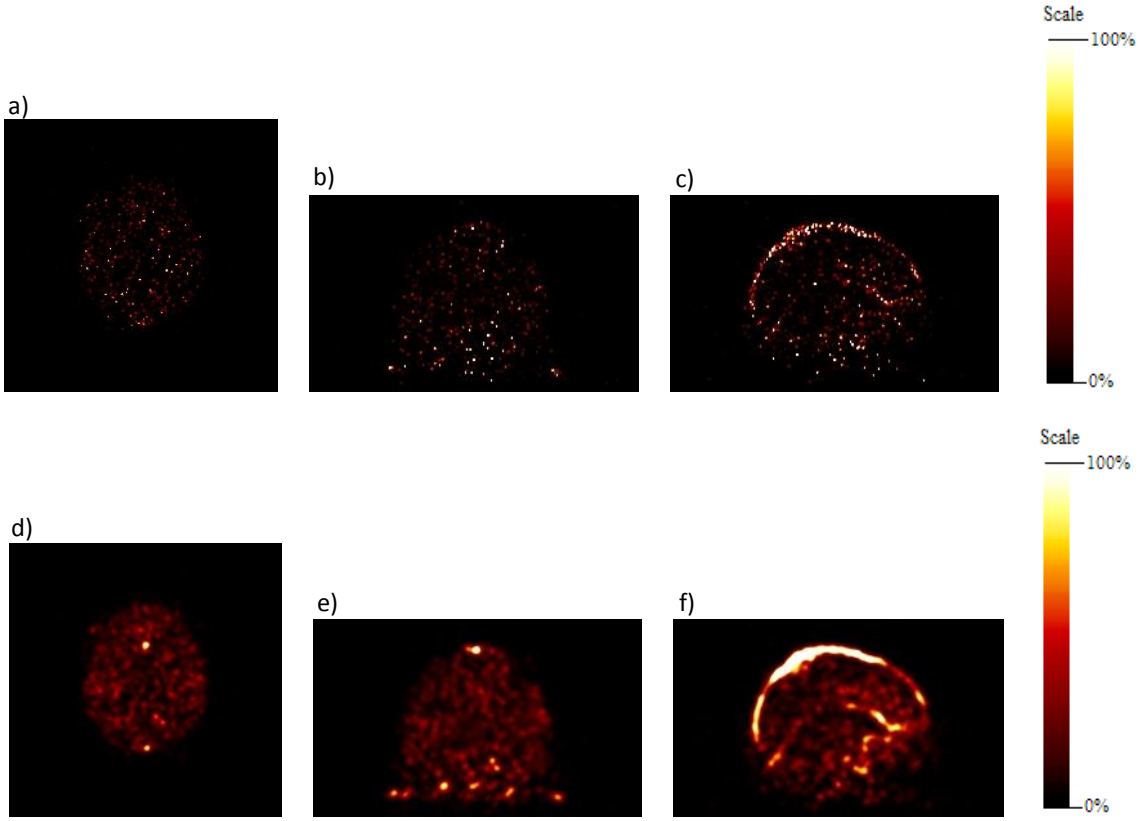

Figure 5. 8: [18F]-FDG images from brain phantom (frame 3): images without Gaussian filter are represented in the first row, images with Gaussian filter are in the last row. The images were represented in transversal (a) and d)), coronal (b) and e)) and sagittal (c) and f)) view. All these images are motionless.

All the images used in the thesis were always filtered before the motion estimation, using the Gaussian filter with sigma = 6mm.

5.2.1. Influence of statistics

In dynamic PET studies the data is divided into discrete time frames therefore these datasets have several images/frames with different statistics. Higher the frame number higher the statistics of the image. Image statistics directly affects the levels of noise in the image and consequently, it is expected that it also affects the ITK motion estimation, which uses these images as input. Therefore it is important to study the influence of statistics in motion estimation. The reconstructed images with 41 iterations from Utah and brain phantoms (all dynamic data) were

used. In each image, the four motions were simulated: 1 mm and 1°; 5 mm and 5°; 10 mm and 10°; and 30 mm and 30°. In this study the same image was always used as reference and as moved image i.e. the motion was simulated on the reference image using PRESTO. All the images were filtered with the Gaussian filter. After that the motion was estimated using ITK and then the absolute errors sums of translation and rotation were calculated by the equation 13. Therefore a quantitative analysis about the influence of statistics in motion estimation is possible. For both Utah and brain phantoms, only the Normalized Correlation ITK metrics were used.

Figure 5. 9 shows the Utah phantom with three different statistics, 1.00E6, 2.25E7 and 1.00E9 counts respectively. The Utah phantom was the first to be study because is a simple phantom and then it is easier to work with and afterwards to understand the results.

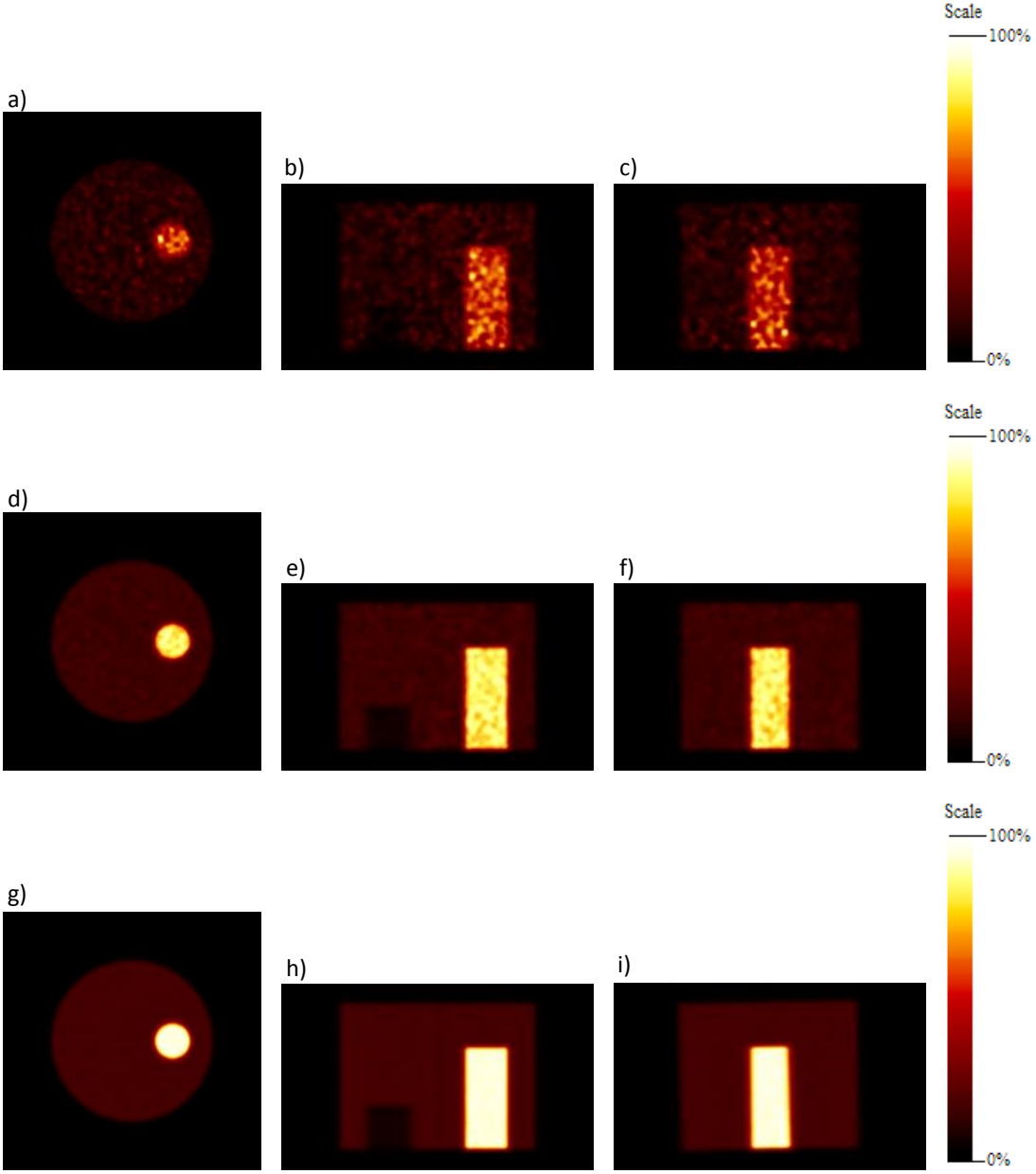

Figure 5. 9: Simulated images motionless from Utah phantom. Each row represents different statistics: 1.00E6, 2.25E7, 1.00E9 counts respectively. In each column transversal, coronal and sagittal views are shown.

Visually these images with different statistics are very different from each other. Higher the statistics better is the definition of the cylinders and then less noise and better resolution has the image, in this case is the image with 1.00E9 counts. Additionally, the phantom in this image has more intensity/bright than the other two images. Contrary, in the image with 1.00E6 counts the cylinders are hardly outlined and the contrast between the two cylinders and the background is smaller. This is because the image has too much noise. Observing this images it can be confirmed that the statistics influence very much the quality of the image.

Figure 5. 10 shows the Utah phantom without and with motion and the respective corrected image. 5 mm and 5º is the motion depicted in this figure. Here only the statistic of 1.00E9 counts was represented because is the image with highest statistics therefore is the best to observe the motion and its correction. The other motions were also simulated and then corrected however they are not represented in the figure. Nonetheless when it was used simulated images with 30 mm and 30º of motion, the movement seems not to be corrected. This is true for all Utah images with different statistics used. Additionally using the images with 1.00E6 counts the motion correction shows less accuracy.

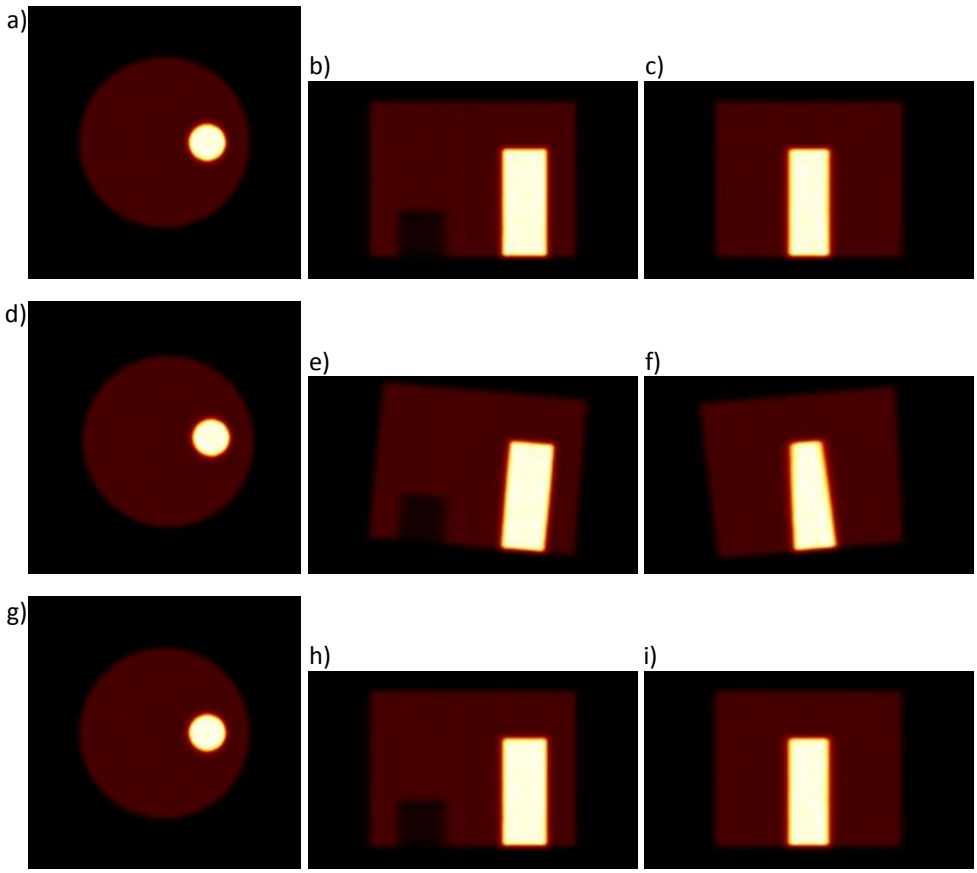

Figure 5. 10: Simulated images with Utah phantom (statistic of 1.00E9 counts). Phantom PET images (fixed image): a) transversal b) coronal and c) sagittal views. In d), e) and f) are represented the simulated images with a translational motion of 5 mm and rotation of 5° with respect to all three axes. g), h) and i) correspond to the corrected images. As ITK metric, Mutual Information was used.

The chosen statistic allows seeing very well the motion (difference between the moved image and the fixed image) especially on coronal and sagittal views. However it cannot be recognized on transversal view. Comparing, in Figure 5. 10, a)-c) with g)-i) it can be seen that, one more time, visually ITK is able to estimate the simulated motion and then PRESTO can correct it. However visual inspection is not a reliable method to confirm if this software can estimate the motion, thus quantitative values errors were calculated. Next figure shows a comparison of the translation and rotation error sums between the images with different statistics.

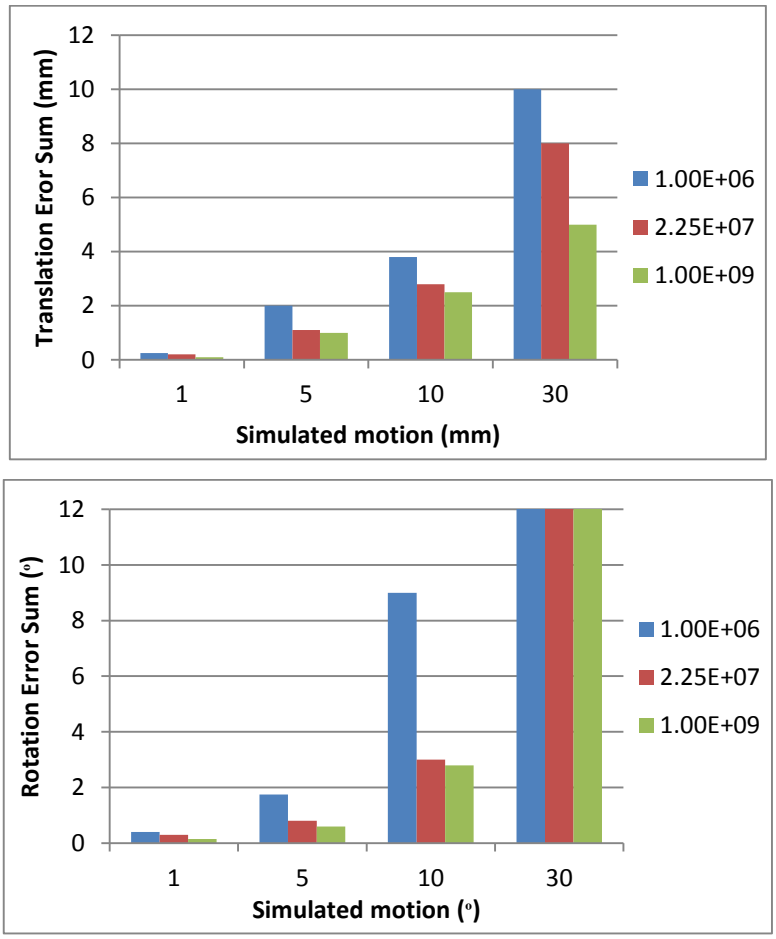

Figure 5. 11: Graphs representing the absolute errors sums of translation and rotation, respectively. Here the ITK output values from Utah phantom were used. The graphs show three different statistics (1.00E6, 2.25E7 and 1.00E9 counts) and four simulated motions (1 mm and 1º; 5 mm and 5º; 10 mm and 10º; and 30 mm and 30º).

Observing the Figure 5. 11 it can be concluded that ITK presents bigger errors when images with low statistics were used or/and when large motions were simulated. This is observed in both translation and rotation. Higher statistics (i.e. less noise) smaller are the errors of motion estimation. Applying 30 mm and 30º of motion the errors are considerably large regardless of image statistics. In rotation, when the largest motion was simulated, ITK hardly detects the

motion: the image with 2.25E7 counts presents an error sum of 89% in regard to the simulated motion while the image with 1.00E6 counts shows an error sum of 99%. In this analysis the ITK errors are bigger in rotation than in translation. Concluding ITK better estimates better the motion in translation than in rotation. Excluding the motion of 30 mm and 30º and the image with low statistics (1.00E6), Utah phantom shows a translation error sum of 9.6% and a rotation error sum of 11%.

Utah phantom structure is rather simple when compared to a human brain, therefore is important to also use a more complex phantom such as a simulated brain phantom. This phantom was simulated by PRESTO and it was possible to have access to all dynamic data, which means the activity of each region changes along the time. Figure 5. 12 shows images from different frames (different statistics – see Table 4. 3) of the brain phantom. In this figure only the frame 4 (1.81E5 counts), frame 9 (8.20E5 counts), frame 14 (6.11E6 counts) and frame 19 (4.87E7 counts) are represented.

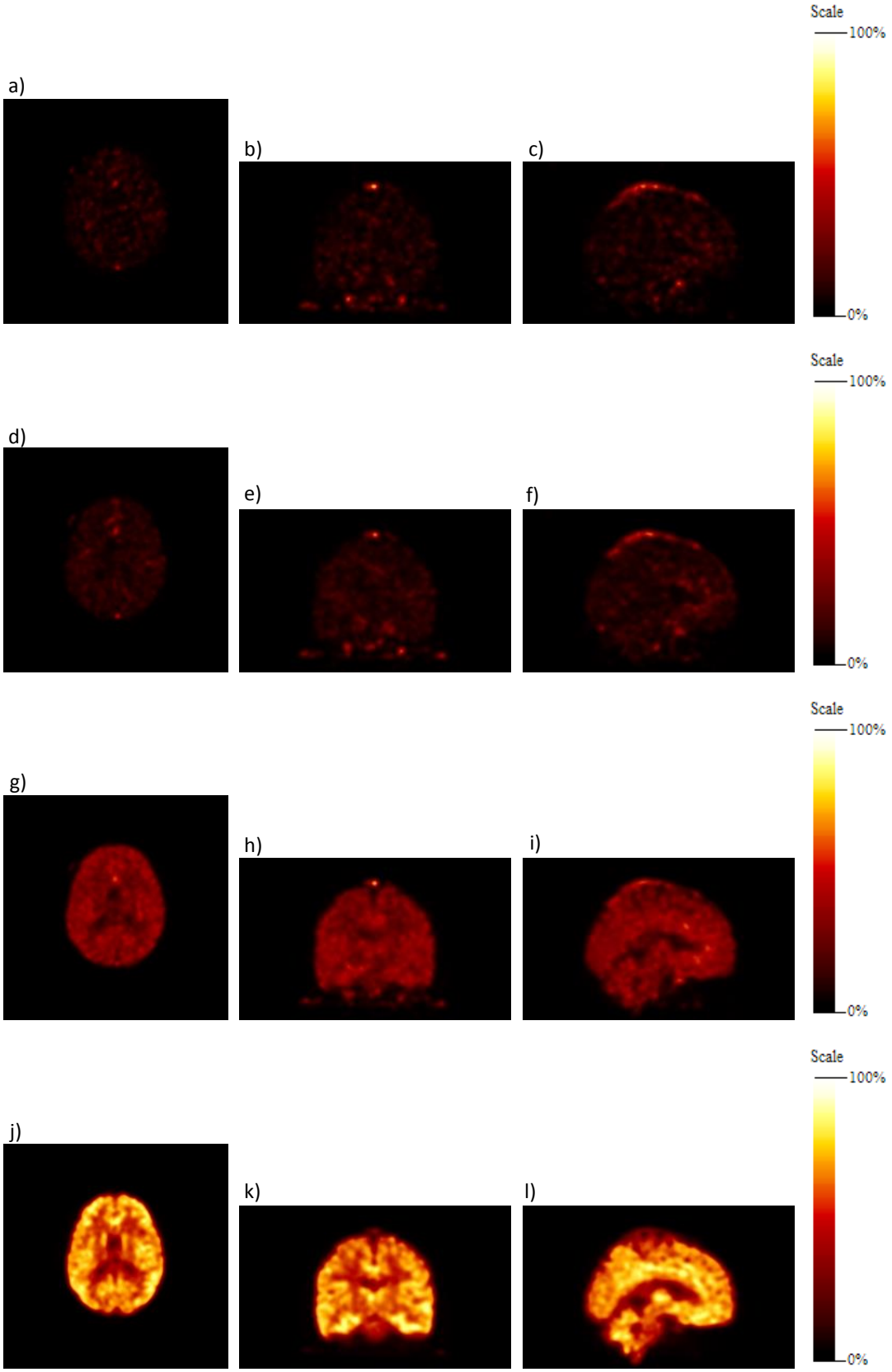

Figure 5. 12: Simulated images motionless from brain phantom. Each row represents different frames i.e. images with different statistics: Frame 4 (1.81E5 counts), frame 9 (8.20E5 counts), frame 14 (6.11E6 counts) and frame 19 (4.87E7 counts) respectively. In each row transversal, coronal and sagittal views were shown.

Observing the Figure 5. 12 it can be concluded the same as in Figure 5. 9: higher the statistics better is the brain structures recognized and delimited. Therefore the images that correspond to frame 19 have the less noise and more intensity. In frame 4 and 9, the brain cannot be recognized, mainly because there is little activity in the brain tissues and most activity is in the vessels still. The structure and projections of the brain became to be recognized in frame 14. One more time, it can be concluded that the statistics can greatly influence the image visually.

Figure 5. 13 shows three different images from brain phantom: fixed image, moved image and the respective corrected image. Here only frame 11 is represented because it is a middle frame from dynamic data. In the moved image were simulated 5 mm of translation and 5º of rotation with respect to the three cardinal axes. The others motions were simulated too, however they are not represented in the figure.

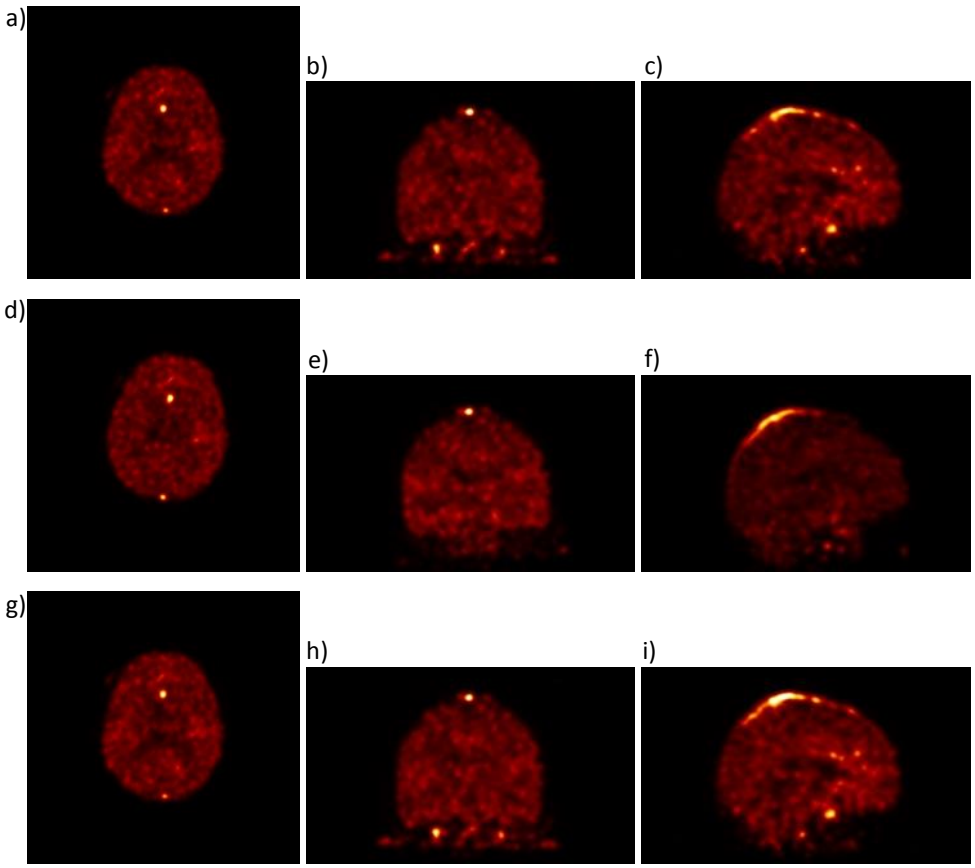

Figure 5. 13: Simulated images with brain phantom (frame 11). Phantom PET images (fixed image): a) transversal b) coronal and c) sagittal views. In d), e) and f) are represented the simulated images with a translational motion of 5 mm and rotation of 5° with respect to all three axes. g), h) and i) correspond to the corrected images. As ITK metric, Normalized Correlation was used.

In Figure 5. 13 it can be observed the motion comparing the three views of the first row of images with the second row. This phantom is more complex than Utah phantom therefore the motion is

more difficult to recognize. Observing the first and last rows, the corrected image match with the reference image, thus it can be concluded that, visually, ITK is able to estimate the motion using phantoms that are not too simple and resemble the human brain.

For the brain phantom is also necessary to quantify the errors for motion estimation using ITK. Figure 5. 14 shows this quantification of the four simulated motions (1 mm and 1º; 5 mm and 5º; 10 mm and 10º; 30 mm and 30º). For that the absolute error sum of translation and rotation were calculated. In the figure only the frame 5 (2.17E5 counts), frame 11 (1.29E6 counts) and frame 19 (4.87E7 counts) are represented, however the others frames shows similar results.

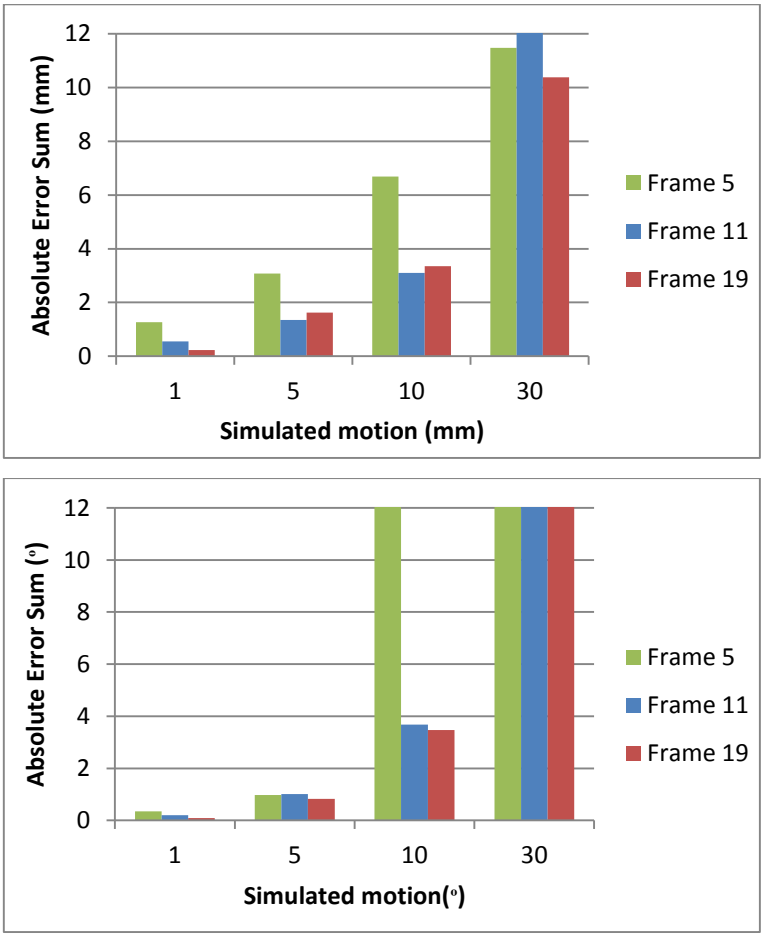

Figure 5. 14: Graphs representing the absolute errors sums of translation and rotation, respectively. Here the ITK output values from brain phantom images were used. In these graphics are represented only three frames: frame 5 (2.17E5 counts), frame 11 (1.29E6 counts) and frame 19 (4.87E7 counts). The other frames are not showed here but they show the same behavior.

In those graphs it can be seen the same as for Utah phantom: for simulated images with low statistics, i.e. high level of noise, and larger motions (30 mm and 30°), ITK shows considerable errors (Figure 5. 14) because the phantom moves out of the field of view resulting in unstable

motion corrections. Comparing Figure 5. 11 (image with 1E6 counts) and Figure 5. 14 (frame 11 with 1.29E6 counts) it can be concluded that the translation and rotation error sums, in generally, are bigger in brain phantom images than in Utah phantom images. This is maybe because of the complexity of the brain phantom and then ITK cannot estimate the motion with the same precision than with the Utah phantom.

With the last frames of dynamic data (frame 13-23) the errors average and errors standard deviation were calculated (see Table 5. 6). Only frames 13 to 23 were used in this analysis because the first frames have lower statistics and this will negatively influence the results. Most of the results are not high (less than 1 mm and 1°), therefore ITK could estimate the motion on most frames of dynamic data. When it was simulated motions of 30 mm and 30° the average of errors are much bigger than the other motions, around 3.5 mm (11.5% of the simulated motion) and 10° (33.7% of the simulated motion). Rotation estimation has bigger errors average than translation. Error standard deviation has the same behavior too. Therefore, once again, ITK motion estimation proved to be more accurate in translation than rotation.

Table 5. 6: Average and standard deviation from motion estimation errors. Dynamic brain phantom data (frame 13-23) was used.

Simulated motion (mm and °)		**Average (mm and °)**	**Standard deviation (mm and °)**
Translation	1	0.22	0.24
	5	0.34	0.30
	10	0.92	0.57
	30	3.45	1.85
Rotation	1	0.30	0.23
	5	1.01	1.19
	10	0.92	2.73
	30	10.11	7.36

Concluding this study shows that the motion estimation is directly influenced by the image statistics. Higher statistics better is the quality image and then better the ITK estimate the motion i.e. smaller are the errors. Furthermore when large motion are applied in the image, ITK shows also very large errors. Therefore it can be concluded that ITK motion estimation has these two limitations.

5.2.2. Influence of number of iterations

As the number of iterations is a user-defined parameter in image reconstruction it is important to study the influence of this parameter in motion estimation. Despite all the brain phantom frames were used in this study, only four of them are shown: frames 5, 11, 17 and 23. However the others frames presented identical behavior. Each of these images were reconstructed with two different numbers of iterations: 11 and 41. These two values were chosen because they are commonly used in studies at FZJ. The images were reconstructed by OPOSEM algorithm and it is relatively slow convergence, therefore, as previous referred, the noise amplifies and the bias decreases with increasing number of iterations. Therefore the image with 11 iterations should present less noise and more bias and the image with 41 iteration should present the opposite. A trade-off between noise and bias is almost always necessary.

In this analysis the normalized correlation ITK metric was used. All the images were filtered before the motion estimation. As in the previous studies, the reference and moved image are the same because the motion were simulated on the reference image. Figure 5. 15 shows the reconstructed frame 11 with the two different number of iterations: 11 and 41. Transversal, coronal and sagittal views are represented.

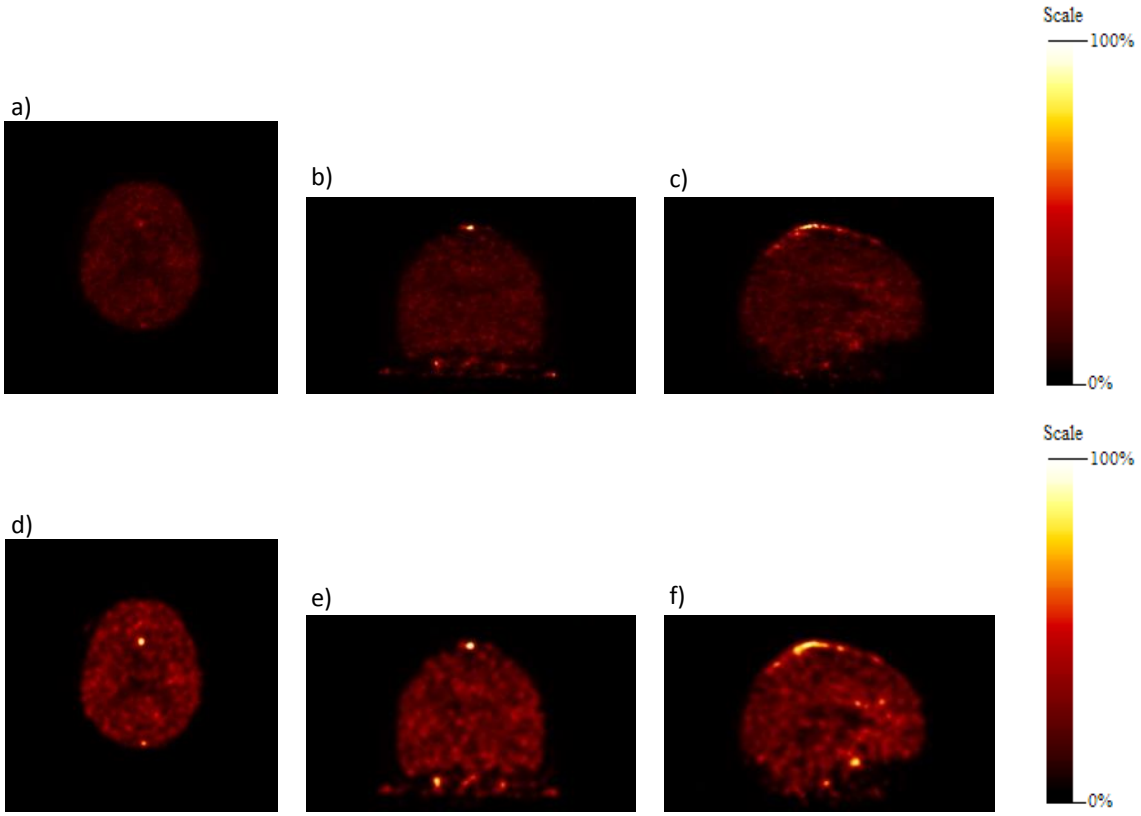

Figure 5. 15: Frame 11 (statistics of 1.29E6) from brain phantom image. In the first row are shown images with 11 iterations and last row 41 iterations. Transversal, coronal and sagittal views are represented.

In the previous images it can be observed that the number of iterations has also influence in the image. The image with 41 iterations has more noise than the image with 11 iterations. However, it should be underlined that this image has less bias than the image reconstructed with 11 iterations. The question which remains is: Will the number of iterations directly influence the ITK motion estimation results? Therefore to answer this question, a comparison between the absolute errors of reconstructed images with different number of iterations was made (see Table 5. 7). Here the translation and rotation error sums of the four types of motions are represented. Only the frames 5 (2.17E5 counts), 11 (1.29E6), 17 (4.40E7) and 23 (1.19E8) with 11 and 41 iterations are shown in this table.

Table 5. 7: Translation and rotation error sums about four different motions (1 mm and 1º; 5 mm and 5º; 10 mm and 10º; and 30 mm and 30º) from the frames 5, 11, 17 and 23 of brain phantom. Here 11 and 41 iterations were tested.

Statistics (counts)	**Simulated motion**		**Iterations**		**Simulated motion (º)**		**Iterations**	
			11	**41**			**11**	**41**
2.17E5 (frame 5)	Translation Error Sum (mm)	1	**0.39**	**0.39**	Rotation Error Sum (º)	1	**0.04**	**0.04**
		5	**1.89**	1.90		5	**0.87**	**0.87**
		10	**3.65**	3.67		10	**3.52**	**3.52**
		30	**18.37**	19.32		30	**89.77**	89.79
1.29E6 (frame 11)	Translation Error Sum (mm)	1	**0.37**	0.40	Rotation Error Sum (º)	1	**0.04**	0.07
		5	**1.78**	1.85		5	**0.87**	0.89
		10	**3.47**	3.55		10	**3.52**	4.48
		30	18.20	**10.90**		30	89.60	**35.70**
4.40E7 (frame 17)	Translation Error Sum (mm)	1	**0.35**	**0.35**	Rotation Error Sum (º)	1	**0.04**	**0.04**
		5	**1.72**	1.73		5	**0.87**	**0.87**
		10	**3.34**	3.36		10	**3.50**	3.51
		30	**9.96**	10.12		30	**35.50**	35.55
1.19E8 (frame 23)	Translation Error Sum (mm)	1	**0.35**	**0.35**	Rotation Error Sum (º)	1	**0.04**	**0.04**
		5	**1.72**	1.73		5	**0.87**	**0.87**
		10	**3.35**	3.36		10	**3.50**	3.51
		30	**10.05**	10.15		30	**35.50**	35.57

The results show that the motion estimation presents smaller errors when it was used images with 11 iterations than 41 iterations (see Table 5. 7). This occurs in all frames, however it cannot be concluded that lower the number the iteration better the results. The number of iterations must be

carefully selected so as to achieve reliable quantitative results while keeping noise within acceptable levels. Nevertheless the difference between the errors of this two numbers of iterations is very small (0.02 mm in translation and 0.06º in rotation). These values are the error sums difference average accounting for 1 mm and 1º, 5 mm and 5º and 10 mm and 10º motions. The largest motion expressed very high and inconsistent errors.

Therefore it was decided to use reconstructed images with 41 iterations in the others studies because this is the most used in FZJ.

As expected, the same results of previous studies were observed: using images with low statistics and simulated large motions present higher errors on motion estimations. When 30 mm and 30º was simulated the errors are extremely high, especially in rotation.

5.2.3. Estimation using PET and/or MR images

The aim of the thesis is to find out if ITK can be used for motion correction in a clinic PET/MRI context. Here the MR image can be used as additional source for motion parameter estimation of PET images. Therefore PET and MR images from the same volunteer were tested. [18F]-FDG (PET) and EPI (MR) images were chosen because they are widely used in clinical practice. Regarding the PET image, the volunteer was administrated with [18F]-FDG (310 MBq) and the acquisition took about 35 min (96 min p.i.). For both PET and MR images, the reference and moved image are the same because the motion were simulated on the reference image. The Gaussian filter was applied in all the images which were reconstructed with 41 iterations. The motions of the two images were estimated using Normalized Correlation ITK metric.

Figure 5. 16 shows the [18F]-FDG images while Figure 5. 17 shows the EPI images. In each figure are represented the fixed, moved and corrected images. The motion represented was 5 mm of translation and 5º of rotation. Here transversal, coronal and sagittal views are shown.

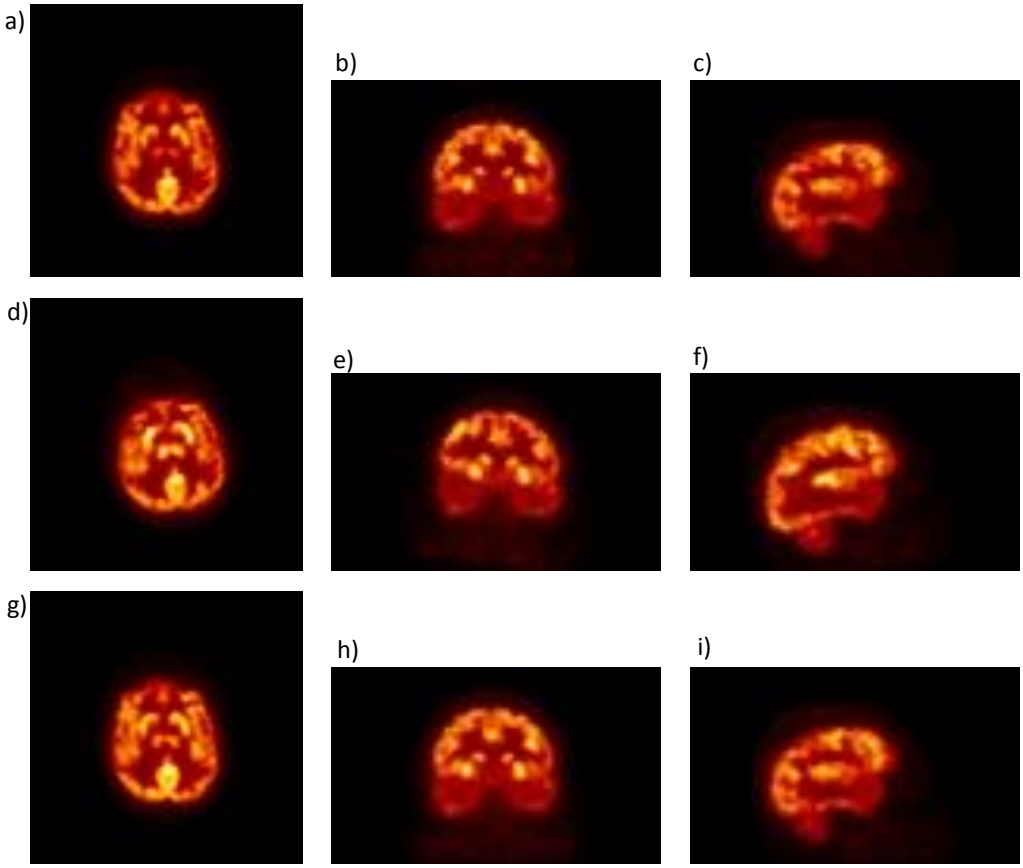

Figure 5. 16: Clinical images of PET ([18F]-FDG). Acquired PET images (fixed image): a) transversal, b) coronal and c) sagittal view. d), e) and f) represent the simulated images with a translational motion of 5 mm and rotation of 5° with respect to all three axes. g), h), and i) show the corrected images. As ITK metric, Normalized Correlation was used.

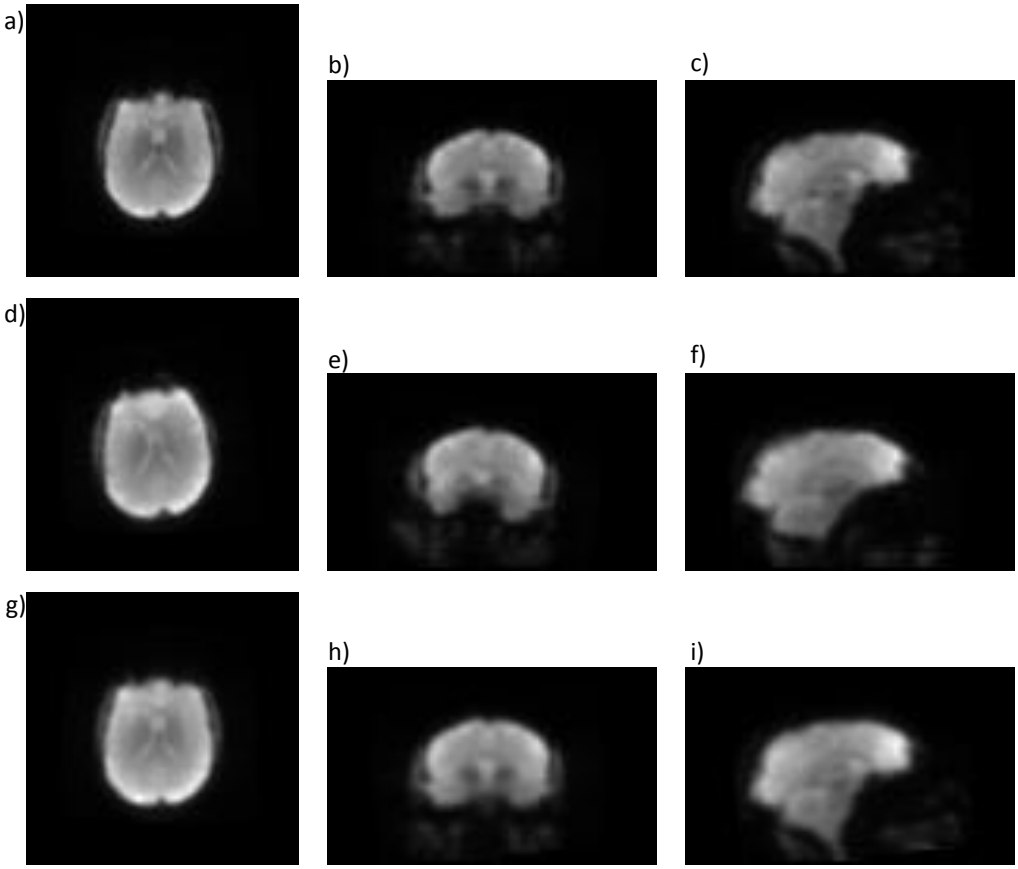

Figure 5. 17: Clinical images of MR (EPI). Acquired MR images (fixed image): a) transversal, b) coronal and c) sagittal view. d), e) and f) represent the simulated images with a translational motion of 5 mm and rotation of 5° with respect to all three axes. g), h), and i) show the corrected images. As ITK metric, Normalized Correlation was used.

In Figure 5. 16 and Figure 5. 17 the motion can be observed very well and the respective correction too. These differences can be better seen in Figure 5. 17 than Figure 5. 16. This is because the [18F]-FDG images have more noise than EPI images. Only the motion of 5 mm and 5° is shown because the motion can be recognized in the images and, at the same time, the volunteer brain does not move out the field of view. Visually, ITK is able to estimate the simulated motion in PET and EPI images. This is concluded because the corrected images seem to be similar to the fixed images i.e. in the same position. The other two motions (1 mm and 1º and 10 mm and 10º) were studied and they show the same behavior. The motion of 30 mm and 30° cannot be really corrected.

The PET and MRI absolute error sums were compared in order to confirm if this software really works with these two different image modalities (Figure 5. 18).

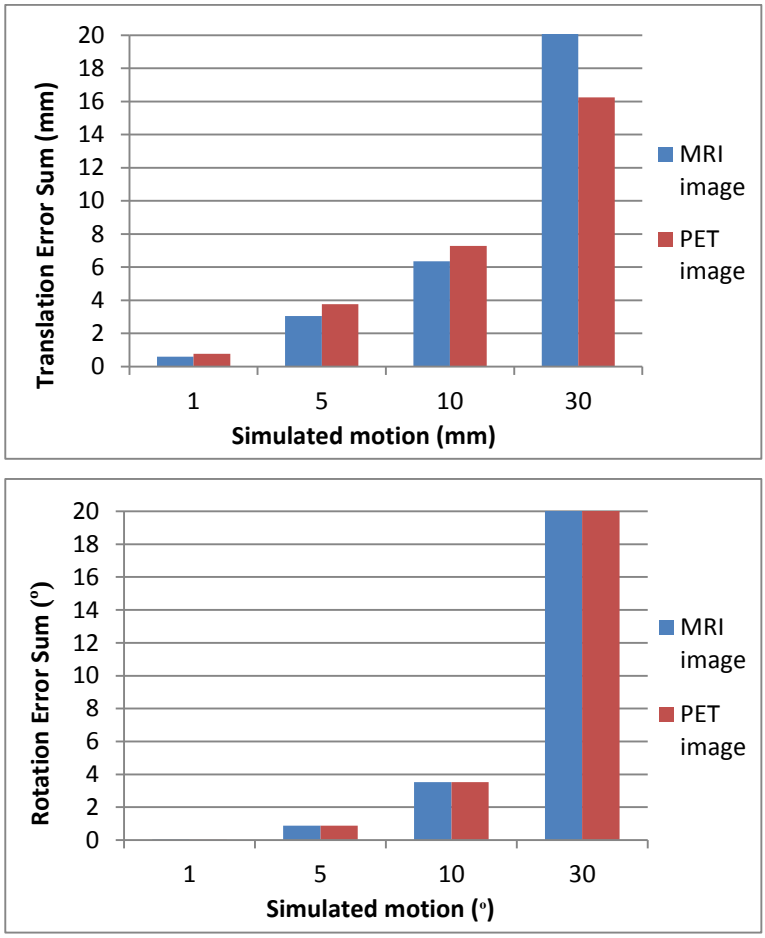

Figure 5. 18: Graphs representing the absolute errors sums of translation and rotation, respectively. Here ITK values from PET ([18F]-FGD) and MR (EPI) images were used. Four motions are simulated: 1 mm and 1º, 5 mm and 5º, 10 mm and 10º and 30 mm and 30º.

In general, these clinical images exhibit errors smaller than 6.3% of the simulated motion regarding translation for both MRI and PET images and smaller than 15% and 20% of the simulated motion regarding rotation for MRI and PET images respectively. One more time ITK revels higher errors in rotation than in translation. These percentages consist in the errors sums average of the motions except the simulated motion of 30 mm and 30º.

The absolute errors of using PET images are bigger than using MR images. [18F]-FDG generally have worst resolution than EPI image. Because of that ITK detected much better the motion in MR images than in PET images. Quantifying these differences (between PET and MR images) it can be concluded that the difference of translation error sum is around of 5% of the simulated motion and the difference of rotation error sum is around 0.15%. Once again, these numbers were calculated using the percentage errors average of the first three simulated motions. Motion of 30 mm and 30° was not included because the errors are very large.

PET images present worst results than MR images however in a previous study it was proved that if the PET image has higher statistics the results will be better. On the other hand if the PET images has lower statistics the results will be worst. Therefore the EPI images can then be used to correct the motion for the first frames and the PET images can be used when the frames have sufficient statistics. The results of the two types of medical image also prove that ITK is a versatile software.

Once again, in Figure 5. 18 one ITK limitation is beaded: with large motions the results are worst because the object moves out of the field of view and make it difficult to detect the real motion such as when 30 mm and 30º was simulated. As expected, it can be concluded that the clinical images present worst results than the phantom images. This is because of the detail and complexity of the clinical images. Higher the image detailed and complexity, higher is the difficulty for ITK to estimate the motion precisely. Excluding large motions and low statistics, both phantom and clinical data allow rather accurate parameter estimation.

5.2.4. Choice of reference frame

On all previous studies the reference and the moved image are the same i.e. the motion was simulated in the reference image. However in clinical analysis this is not possible, there are frames without motion and frames with motion and only one specific frame or an average of frames is usually used as reference to correct the motion of all the other frames. Therefore an additional study has the aim to find out which frame should be chosen as reference when dynamic data is used, and if it affects the results significantly. In this study the [18F]-FDG dynamic data from the simulated brain phantom was used. This dataset has 23 frames and the Gaussian filter was applied on all the reconstructed images with 41 iterations. The four motion were also simulated and the estimation was made using Normalized Correlation ITK metric.

First, a comparison between using the same frame as reference and moved image and using frame 13 as reference to correct the other ones was made for all dynamic data. Frame 13 was chosen because it is one frame in the middle of the dynamic data (not too far from the beginning of the acquisition) and at the same time it has a considerable statistics, i.e. it has statistic above median (median = 1.29E6 counts).

Figure 5. 19 shows the results of these two methods. The dynamic data have 23 frames in total being impossible to present every frame on this graph. Therefore frames 3, 7, 11, 15, 19 and 23 were chosen to represent this study. Here only motions of 1 mm and 1º and 5 mm and 5° were shown but the other two motions (10 mm and 10º and 30 mm and 30º) presented similar results.

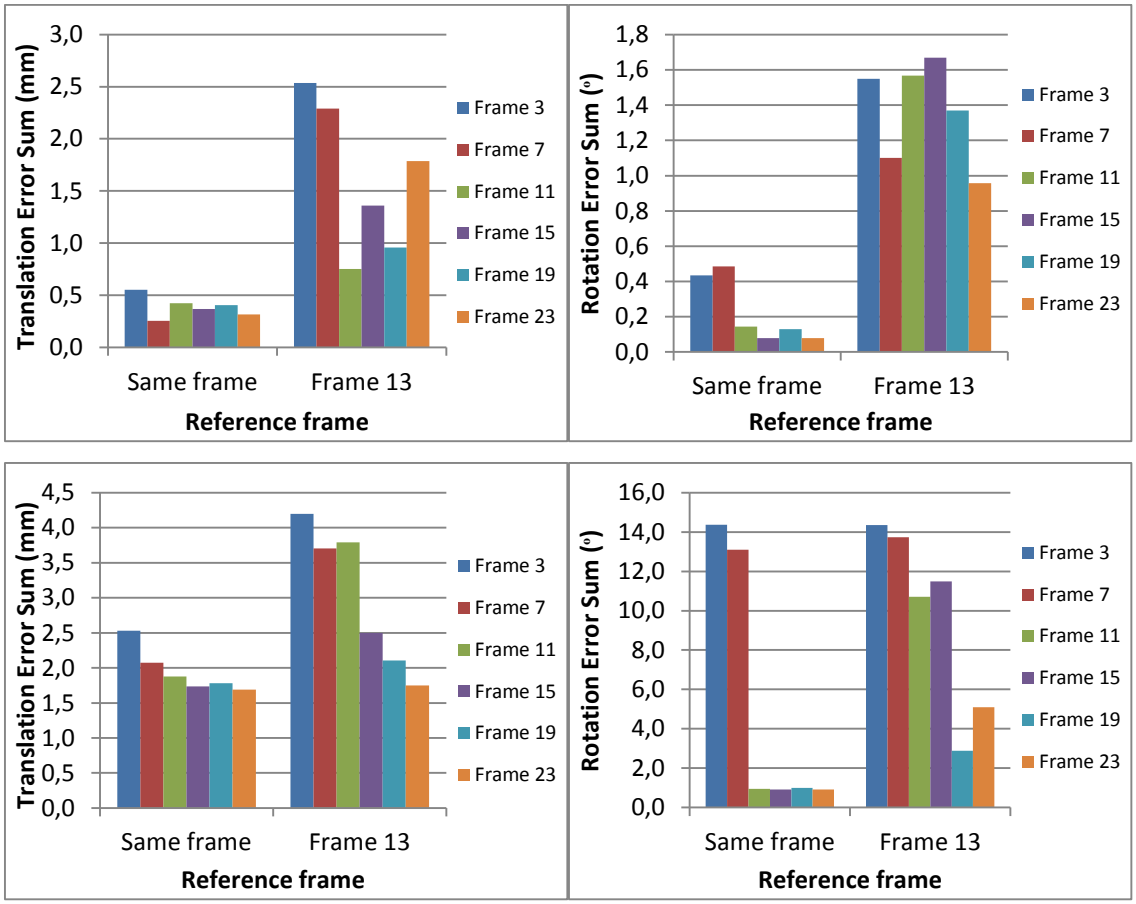

Figure 5. 19: In each row the absolute errors sums (in the three axes) of translation and rotation are respectively represented. The two graphics from first row correspond to 1 mm and 1° of motion on the three axes and the graphics from the last row correspond to 5 mm and 5° of motion on the axes too. Each graphic show the results using the same image as reference and moved image and using the frame 13 as reference image to correct the other ones. Here only six frames for dynamic brain phantom data were used. Normalized correlation ITK metric was used.

In Figure 5. 19 it can be noticed that using frame 13 as reference, the results are worst i.e. the absolute errors get higher. This reality is observed in translation and rotation and independently of the frame used i.e. independently the statistics of the frame. This is true for all four simulated motions. Using the frame 13 as reference or using the same reference frame as the moved image, images with low statistics have always bigger errors.

Secondly, it was decided to compare these results (using frame 13 as reference image) with the results of using the frame with highest statistics (frame 23) as reference frame. Frame 16 was chosen as moved image because has the statistics above average (2.50E7 counts) and this frame is between the two other frames (13 and 23). In the reference frame choice is important to select a frame with high statistics leading, as discussed in previous studies, to less noise which results in smaller errors. In Figure 5. 20 it is possible to verify the statistics difference between the used frames, 13, 16 and 23.

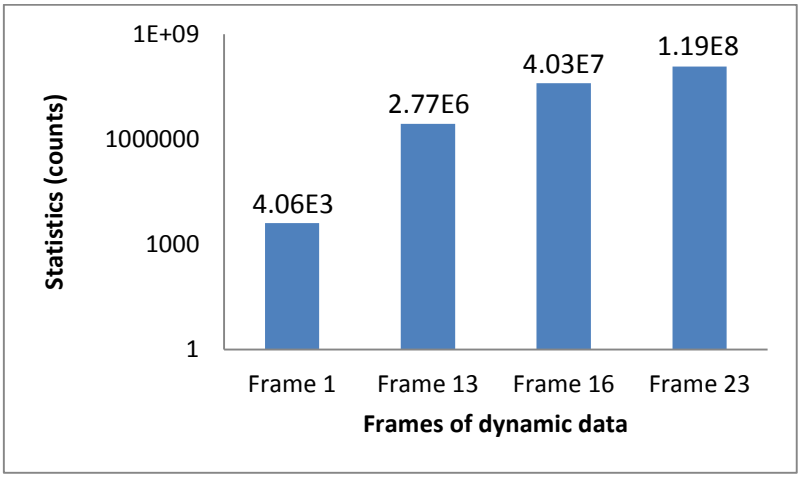

Figure 5. 20: Different frames from [18F]-FDG brain phantom data. The statistics are represented in logarithmic scale. Dynamic data have 23 frames in total.

The Figure 5. 21 represent the qualitative difference between the frame 13 and frame 23.

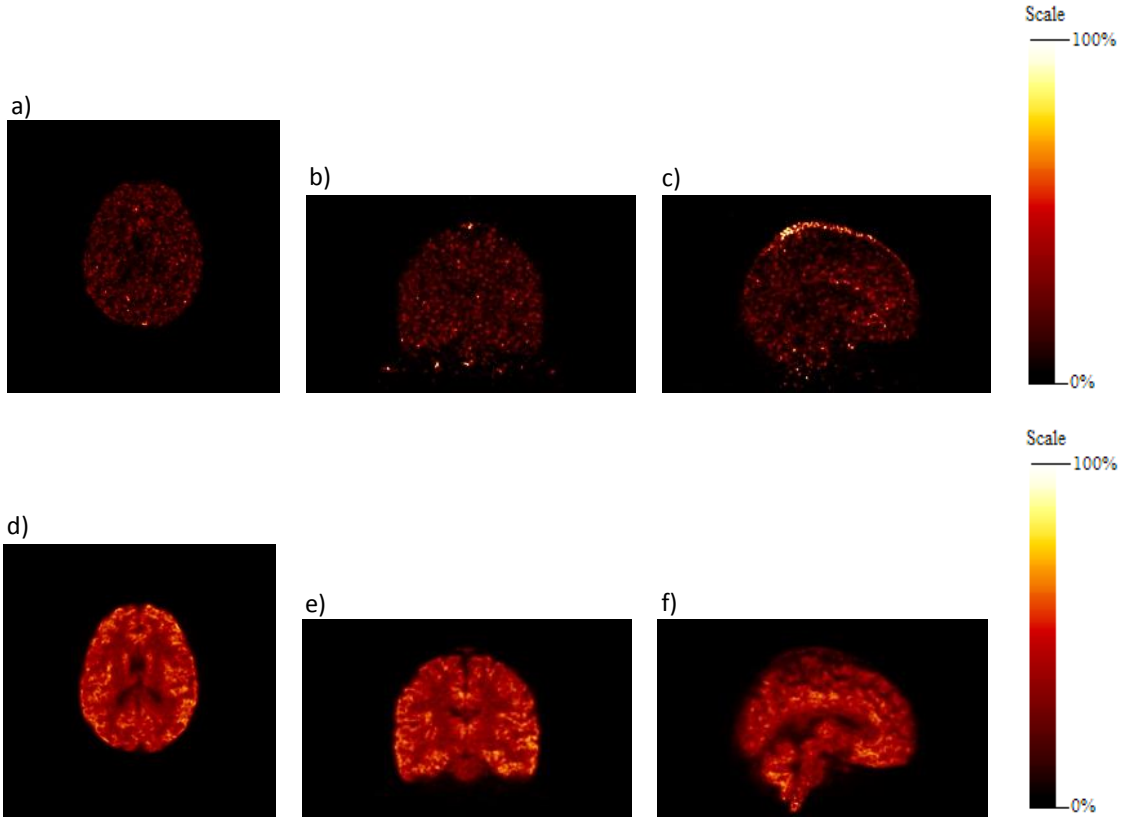

Figure 5. 21: [18F]-FDG images from brain phantom: frame 13 is in the first row and frame 23 in the last row. Acquired images: a) and d) transversal, b) and e) coronal and c) and f) sagittal views. All these images are motionless.

The quantitative comparison between the absolute errors sums using the frame 13 or using the frame 23 as reference is shown in Figure 5. 22. As stated above the moved image is the frame 16.

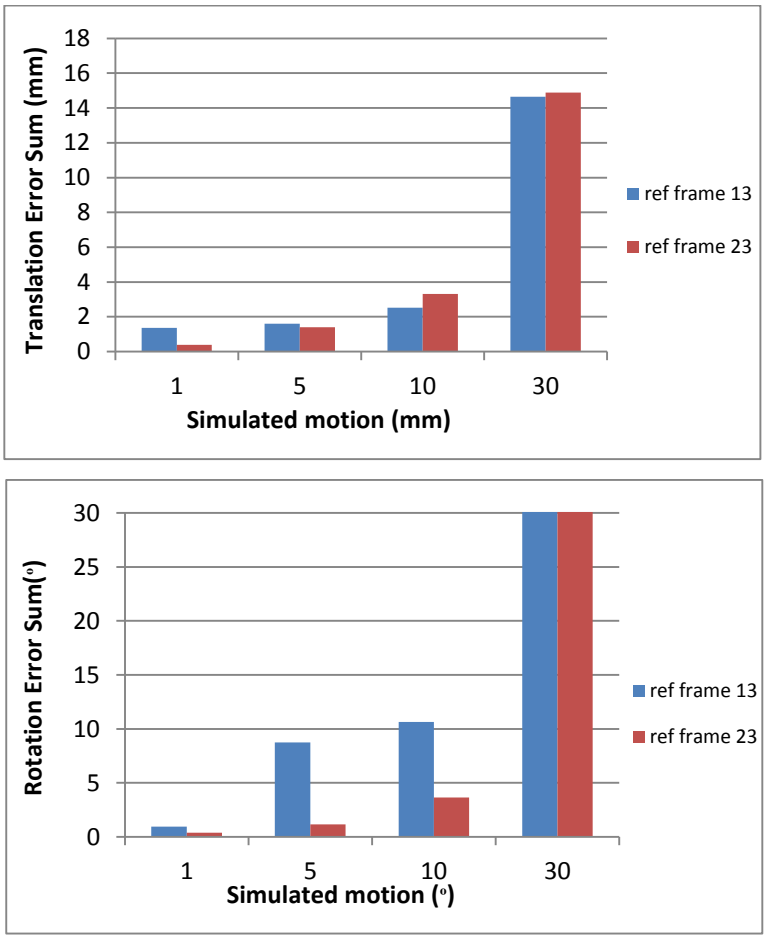

Figure 5. 22: Absolute errors sums (in the three axes) of translation and rotation respectively. These sums were performed for [18F]-FDG dynamic data (brain phantom). The blue columns represent the study when the frame 13 was used as reference frame and the red columns represent the frame 23 as reference. The moved frame used was the frame 16.

Figure 5. 22 shows that the absolute error sums results, using different reference frames, are not similar and they are better when frame 23 was used as reference. This is because it has a higher statistics than the frame 13. However it is not the best choice because the probability of motion is higher at the end of the exam. Furthermore, the MR images for the attenuation map are acquired at the beginning of the acquisition so the last frame can have the worst match with this attenuation map. In both reference frames (13 and 23) the same behavior can be observed: larger motions higher errors.

To confirm if these changes were made only by the reference frame and not by the combination of the two images used in ITK input (fixed and moved images), a additional comparison between

the frame 13 as reference and frame 23 as moved frame and the same two frames but in opposite position was made. The translation and rotation error sums are represented in Figure 5. 23. All the four motions are tested: 1 mm and 1º, 5 mm and 5º, 10 mm and 10º and 30 mm and 30º. These motions were made with respect to the three axes, all at the same time.

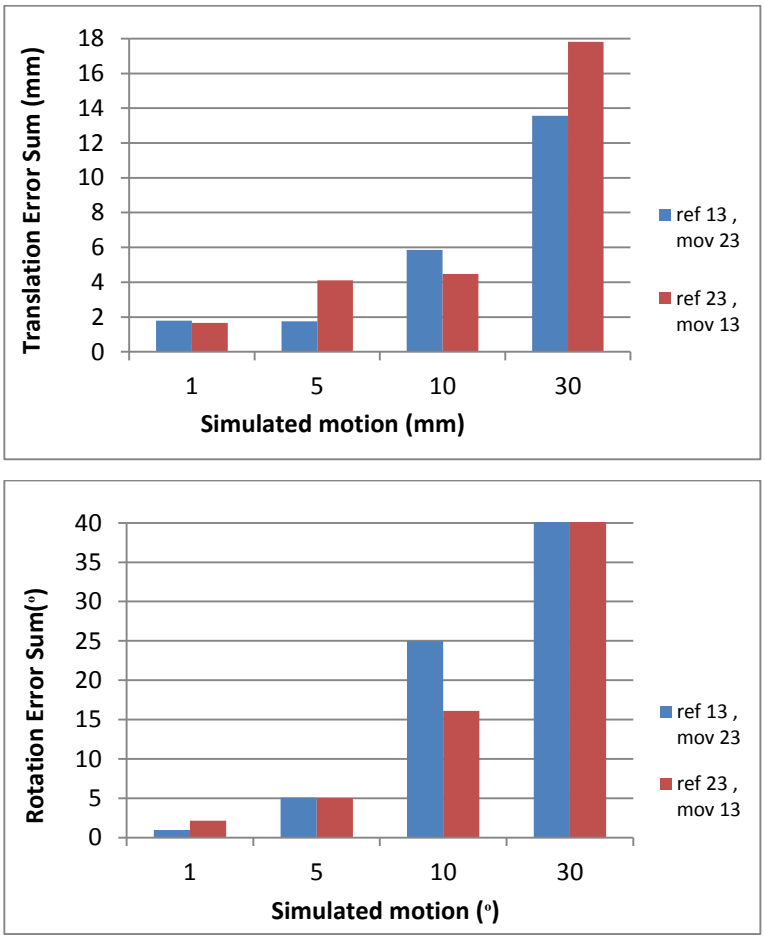

Figure 5. 23: Absolute errors sums (in the three axes) of translation and rotation respectively. These sums were performed for [18F]-FDG dynamic data (brain phantom). The blue columns represent the study when the frame 13 was used as reference frame and frame 23 as the moved frame. The red columns represent the opposite choice.

In this figure it can be seen that, even using the same frames but in opposite positions, the results were very different. Hence the reference image plays an important role in motion estimation. Using ITK, the fixed image and the moved image have different weights in motion estimation. Over again, the same behavior was observed: when using images with 30 mm and 30° of motion the errors are very high. In this figure, the results are balanced, sometimes the errors are smaller when it was used the frame 13 as reference but other times these results are higher. This happens in both translation and rotation analysis. Therefore these last results do not lead to one definitive conclusion.

In general, it is possible to get better results using the frame with high statistics than one middle frame. However the results are even better using the same image as reference and image affected by motion. This happens because it is more difficult for the software to detect the motion with different frames once besides motion, there is also biological/physiological changes in the brain activity. Other possibility is that the time nearness of the frames (following frames) can influence the results of motion estimation and then frames with bigger time difference present bigger errors.

In this study it cannot be concluded which frame should be chosen to correct the motion, but the results prove that it is important to evaluate and stipulate this in the future. For future studies in this thesis, when the dynamic brain phantom data is used, the reference image is the frame 13.

5.2.5. Choice of metrics

ITK has several metrics available for motion estimation. Until now, in all the studies, the Normalized Correlation metric was the only used. In this analysis, in order to improve the results, two more metrics were also tested and compared: Mutual Information and Mean Squares. The Mutual Information metric comprised an optimization ITK parameter, *Set Number of Spatial Sample*, which defines the number of random pixels used to compute this metric. In order to assess changes in results two of its values were tested, 10 000 and 200 000. Mutual Information is the metric used commonly in multi-modality analyses while Normalized Correlation is used with images of one modality. Mean Squares was also tested in this study, because it is the metric used in PMOD clinical analyses at FZJ to correct the motion. Mean Squares is used in one-modality analysis. In order to fully understand the scope of the research topic is important to evaluate which metric can achieve better results. For this comparison filtered images (with 41 iterations) of brain phantom and EPI clinical data were used.

First, images from one modality were studied. Two independent analysis using only [18F]-FDG brain phantom data and only EPI clinical images were made. From [18F]-FDG dynamic data, frame 13 was used as reference frame while frame 23 was used as moved frame (frame with highest statistics). On the estimation using EPI images the same image was used as fixed and moved image (with simulated motion). Table 5. 8 shows the different results achieved. Here only the two smaller motions (1 mm and 1º and 5 mm and 5º) are represented.

Table 5. 8: Absolute errors sums (in the three axes) of the different ITK metrics. These sums were performed for [18F]-FDG and EPI data. The considered motions were 1 mm and 1°;and 5º and 5 mm. For the other motions (10 mm and 10°; 30 mm and 30°) the behavior generally were the same.

ITK metrics	PET (FDG)				MRI (EPI)			
	Translation		Rotation		Translation		Rotation	
	1mm	5mm	1 °	5 °	1 mm	5 mm	1 °	5 °
Mutual Information (10 000)	0.99	1.71	1.69	2.27	0.86	3.93	0.18	0.95
Mutual Information (200 000)	0.50	1.53	0.77	1.33	0.84	3.84	0.16	0.88
Mean Squares	0.65	1.50	2.77	6.79	**0.77**	**3.77**	0.03	0.88
Normalized Correlation	**0.29**	**1.47**	**0.11**	**0.88**	**0.77**	**3.77**	**0.02**	**0.87**

Based on the results shown in Table 5. 8, it can be concluded that when the parameter value (*Set Number of Spatial Samples*) of Mutual Information increases the results improve i.e. the sum of errors are smaller. Using EPI images, Mean Squares and Normalized Correlation shows very similar results, differing by very small values (in the order of hundredth of millimeter or degrees). However the Normalized Correlation metric shows always smaller errors when [18F]-FDG images were used. Concluding, in general, to solve the problem in study, the Normalized Correlation is the best metric for both PET and MR images. Nonetheless the Normalized correlation metric takes more time to estimate the motion than the Mean Squares and Mutual information. Although this difference cannot be quantified because the study about the time difference between the three metrics was not made, it was very evident during the motion parameters estimation. Due to the lack of numbers, these results are not shown in the thesis. [18F]-FDG images do not have worst results than EPI images and one reason for this may be because PET images are from a simulated brain phantom while the EPI image is a clinical image or because the moved PET image has high statistics.

As stated, before Mutual Information metric is used when two types of image (multi-modality) are compared. Nevertheless Normalized Correlation and Mean Squares were used when images from the same modality were studied. In order to confirm this assertion one MRI image (FLASH sequence) and one PET image, both from the simulated brain phantom, were used. Simulated FLASH and [18F]-FDG images are show in Figure 5. 24.

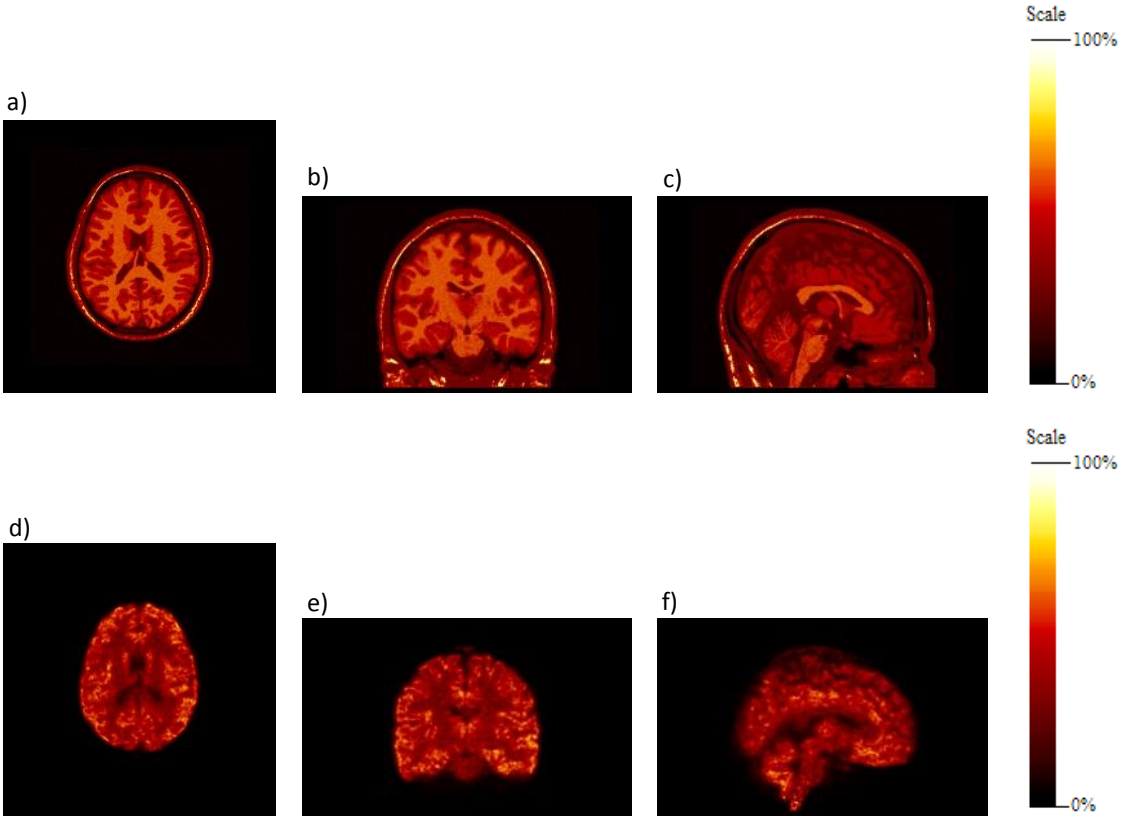

Figure 5. 24: Brain phantom: FLASH sequence images in the first row and [18F]-FDG images in the last row (frame 23). a) and d) transversal, b) and e) coronal and c) and f) sagittal view. All these images are motionless.

Although the two images are from the same phantom, they are very different. FLASH sequence images present higher resolution and lower levels of noise than [18F]-FDG images. The brain anatomy is more detail and its strutures are better deliniated in MR image than PET image. However the brain physology is represented in [18F]-FDG image and not in FLASH image.

Multi-modality analysis was followed. The motion was estimated using the FLASH image as reference image and [18F]-FDG image as image affected by motion and vice-versa. In this study only frame 23 of [18F]-FDG data was used, because it is the frame with highest statistics so is the best frame to estimate the motion. Before this analysis, the MR image was resampled to match the PET image in terms of orientation, center of rotation, image matrix and voxel size. The motion was also estimated using the three ITK metrics including the two mutual information variants. The results of these two multi-modalities comparisons are described in Table 5. 9. The four motion were simulated, however only two motion, 1 mm and 1° and 5 mm and 5° are represented in this table. The other two are not represented but they show the same behavior when these three metrics were analyzed. 30 mm and 30° presents results farthest than these two motion because the phantom moves out of the field of view, then the results are all adulterated.

Table 5. 9: Absolute errors sums (in the three axes) of the different ITK metrics. These sums were performed for [18F]-FDG (frame 23) and EPI data. The first column represents the [18F]-FDG image used as reference image and FLASH image used as moved image. The second column represent the same images but in inverse positions. The considered motions were 1 mm and 1º and 5 mm and 5°. For the other motions (10 mm and 10° and 30 mm and 30°) the results present the same behavior.

	PET image as reference and MR image as moved image				**MR image as reference and PET image as moved image**			
ITK metrics	**Translation**		**Rotation**		**Translation**		**Rotation**	
	1 mm	5 mm	1 °	5 °	1 mm	5 mm	1 °	5 °
Mutual Information (10 000)	0.88	2.11	0.41	1.24	**0.59**	**2.41**	**0.16**	0.95
Mutual Information (200 000)	**0.28**	**0.31**	**0.26**	**1.12**	0.81	2.59	0.23	**0.62**
Mean Squares	6.50	5.83	2.89	14.69	0.87	2.63	0.31	0.64
Normalized Correlation	1.18	2.20	0.32	1.72	0.90	2.65	0.33	0.65

Table 5. 9 shows that, in both analysis, the errors from Mutual Information metric are smaller than the errors from the others two ITK metrics. These smaller errors oscillate between the two different values of the parameter *Set Number of Spatial Sample*. When the PET image was used as reference and MR image as moved image, the results are better using this parameter with the value of 20 000. However when the same images were used but in opposite positions the errors are mainly smaller when the parameter has the value of 10 000. With these results it can be confirmed that Mutual information is the best metric when it was used multi-modality images and Mean squares and Normalized Correlation for one-modality images.

When MR image was used as reference image the results shows small errors than when [18F]-FDG image was used as reference. Therefore, once again, it can be concluded that in motion estimation, it is important to choose a good reference image. The difference may be due to EPI image has less noise than [18F]-FDG image. Hence, ITK can then correct better the motion, because the noise of the input reference image appears to influences directly the estimation.

As throughout the thesis the studies were made using always one-modality images, therefore the best ITK metric is the Normalized Correlation.

5.2.6. Comparison PMOD and ITK

PMOD is a viable software already used in clinical practice at FZJ to correct the motion. Therefore the comparison between PMOD and ITK results is vital to confirm if ITK can replace the PMOD. Comparing with PMOD, ITK is free, user-independent and allows the correction of the motion during the reconstruction (correcting all the LORs affected by the motion), avoiding an additional and hard-working step. Hence, ITK seems to have several advantages over PMOD being a good replacement option. Several datasets were used in this study: Utah phantom, simulated brain phantom, clinical PET ([18F]-FDG) and MRI (EPI) images. All the images were reconstructed with 41 iterations and filtered by a Gaussian filter with sigma = 6 mm. PMOD applies the filter directly in the estimation, but ITK does not, so this filter was implemented in *Matlab*.

Normalized correlation, Mean Squares and Mutual Information ITK metrics were used. PMOD only uses the Mean Square metric. For dynamic data (brain phantom images) the frame 13 was used as reference frame in ITK and PMOD. For the other data sets (Utah phantom, clinical PET and MRI data) the same image as used as reference and moved image. In PMOD one frame or an average of frames can be chosen as reference. Generally some frames of the dynamic data (first frames) are used. ITK only permits one input image (one frame) as reference. In order to use more than one is necessary to do an external procedure and convert several frames in an average image.

In PMOD only the affine transform of the motion can be extracted and values of motion (translation and rotation in all three Cartesian axes) can be obtained through some calculations.

ITK motion estimation works with interfile format while PMOD works with ECAT format. Therefore some conversions were made.

PMOD has some standard parameters that are represented in Table 5. 10.

Table 5. 10: Matching Parameters applied in PMOD to correct the motion.

Matching Parameters	
Gaussian Smoothing window	6.0 mm in all three axes (reference and input)
Dissimilarity function	Mean Squares
Interpolation method	Trilinear
Sample rate (start)	6.0 mm
Minimization method	Powell (Powell 1964)
Function tolerance	1.0E-4
Thresholding method (reference and input)	None
Algorithm runs	1
Max iterations	50

Figure 5. 25 and Figure 5. 26 show the difference between the motion estimation using PMOD or ITK. All four motions contribute to this analysis: 1 mm and 1º; 5 mm and 5º; 10 mm and 10º; 30 mm and 30°. The three ITK metric were also tested in this study. For this comparison all brain phantom frames were used but only the frame 2 and frame 18 are represented in these figures. These two frames were chosen because one has low statistics (frame 2) and another has high statistics (frame 18). It is impossible to show all the data results however they presented similar results to these two frames.

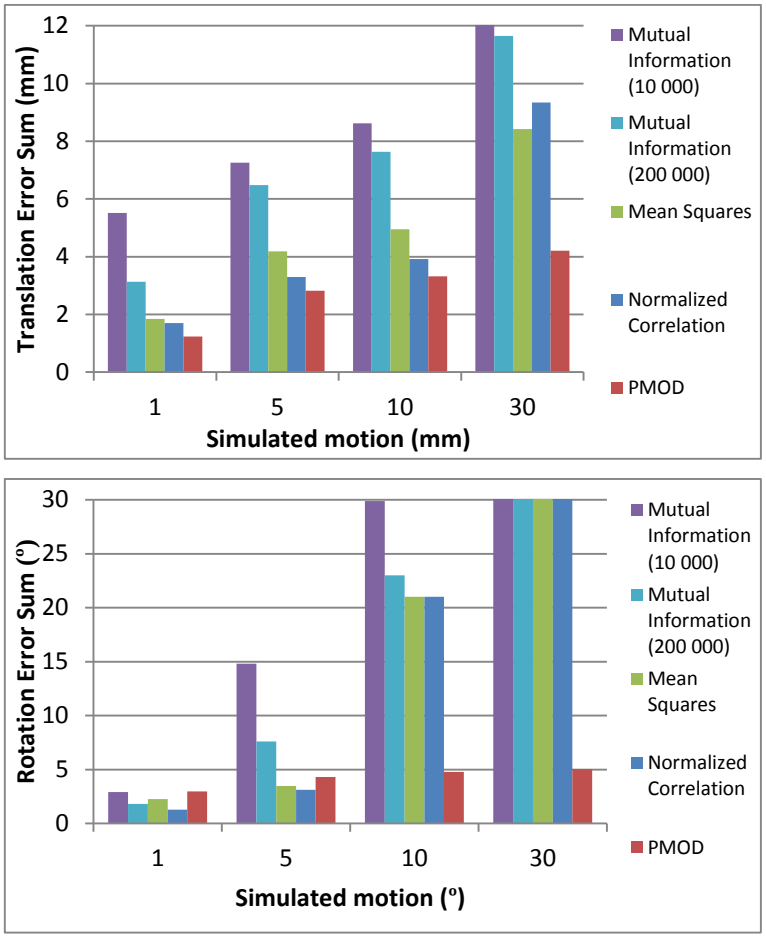

Figure 5. 25: Absolute errors sums (in the three axes) of translation and rotation respectively. The sums were performed for dynamic data of brain phantom ([18F]-FDG). The graphs represent the frame 2 and show the four types of motion (1 mm and 1º; 5 mm and 5º; 10 mm and 10º; 30 mm and 30°). Here the three ITK metrics and the PMOD were compared.

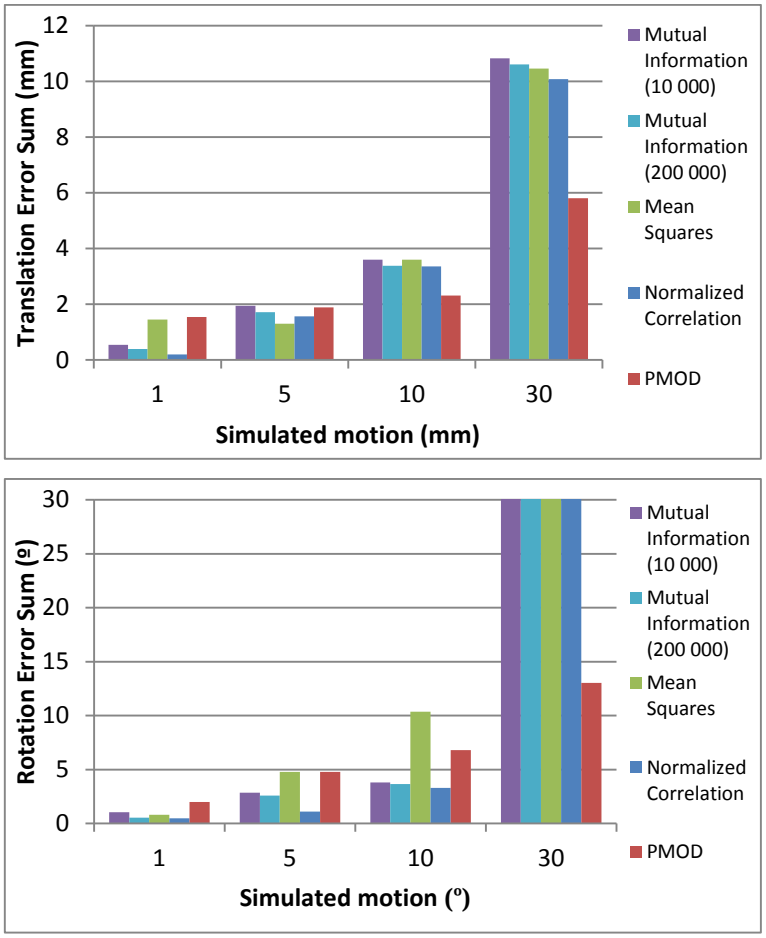

Figure 5. 26: Absolute errors sums (in the three axes) of translation and rotation respectively. The sums were performed for dynamic data of brain phantom ([18F]-FDG). The graphs represent the frame 18 and show the four types of motion (1 mm and 1º; 5 mm and 5º; 10 mm and 10º; 30 mm and 30°). Here the three ITK metrics and the PMOD were compared.

One more time, Normalized Correlation is the ITK metric which presents better results. Therefore this metric is the one chosen when the ITK results are compared with PMOD results in the next paragraphs.

The error averages of ITK is around 11% regarding the simulated motion in translation and around 9% in rotation, while the PMOD error averages are 11% and 15% respectively. The averages were calculated using the errors of the simulated motions excluding the largest one (30 mm and 30º). With these percentages it can be concluded that the ITK and PMOD results are not so different from each other. Referring to Figure 5. 25 and Figure 5. 26 it can be observed that the results are very inconsistent, sometimes PMOD shows better results but other times ITK shows small errors. This means that ITK comparing with PMOD is also a viable program to estimate the motion. The ITK results are more similar to PMOD in translation than in rotation. This is because ITK, as mentioned above, has more difficulty in estimate the motion in rotation, showing higher errors.

According with Figure 5. 25 and Figure 5. 26, when 30 mm and 30° was simulated the PMOD got always better results. Regarding to the biggest motion (30 mm and 30°), ITK Normalized Correlation presents absolute error sums of translation and rotation around 12.4% and 58% of the motion respectively, while PMOD presents 2.2% in translation and 3.88% in rotation. With low statistics images the PMOD also got smaller errors most of the time (Figure 5. 25). Hence it can be concluded that PMOD does not have the same limitation as ITK, i.e. PMOD is able correct large motions and images with low statistics. All the percentages presented in this section were calculated using the dynamic [18F]-FDG data (frame 13 to frame 23) from the brain phantom.

5.2.7. Influence of attenuation map

In the FZJ an atlas-based method is used for attenuation correction. In this case, a MR template is registered to the patient MR image, the transformation matrix is applied to attenuation map template and then the attenuation values are assigned to the PET image. Therefore it was expected that the motion estimation parameters were different when images with different attenuation map were used. These different maps were considered because currently in this institute, the motion is not being taken into account in attenuation maps and if it was the attenuation values would become different. Additionally, as the attenuation correction smooth the intensity contrast between the boundaries of the object in study and the background, maybe this correction does not help the motion estimation using an image-domain MC method like ITK. Hence the influence of attenuation correction (i.e. the application of the attenuation map in the images) in the presence of motion was also studied in this thesis work.

The motion estimation in this study was performed with PMOD and ITK and then a comparison between the software errors was made. Images with the correct attenuation map (map with the simulated motion), with the wrong attenuation map (map without the simulated motion) and images without attenuation correction were considered in this comparison.

[18F]-FDG images (reconstructed images with 41 iterations) of the simulated brain phantom with high statistics were used: frames 21, 22 and 23. In this study only one motion is simulated: 1 mm of translation and 1° of rotation on all the three axes. This motion is the chosen one because in clinical practice is much more common small head motion and larger ones. On the other hand if the results were adulterated by larger motions, because phantom moves out the FOV, the study about the attenuation map would be impossible to do. The images were filtered by a Gaussian filter with sigma = 6 mm. Equally to previous studies, PMOD used the Mean Squares metric while in ITK analysis the Normalized Correlation was used.

The three images (with right, wrong and without attenuation map) from frame 23 of dynamic data are represented in Figure 5. 27. Here transversal, coronal and sagittal views are shown.

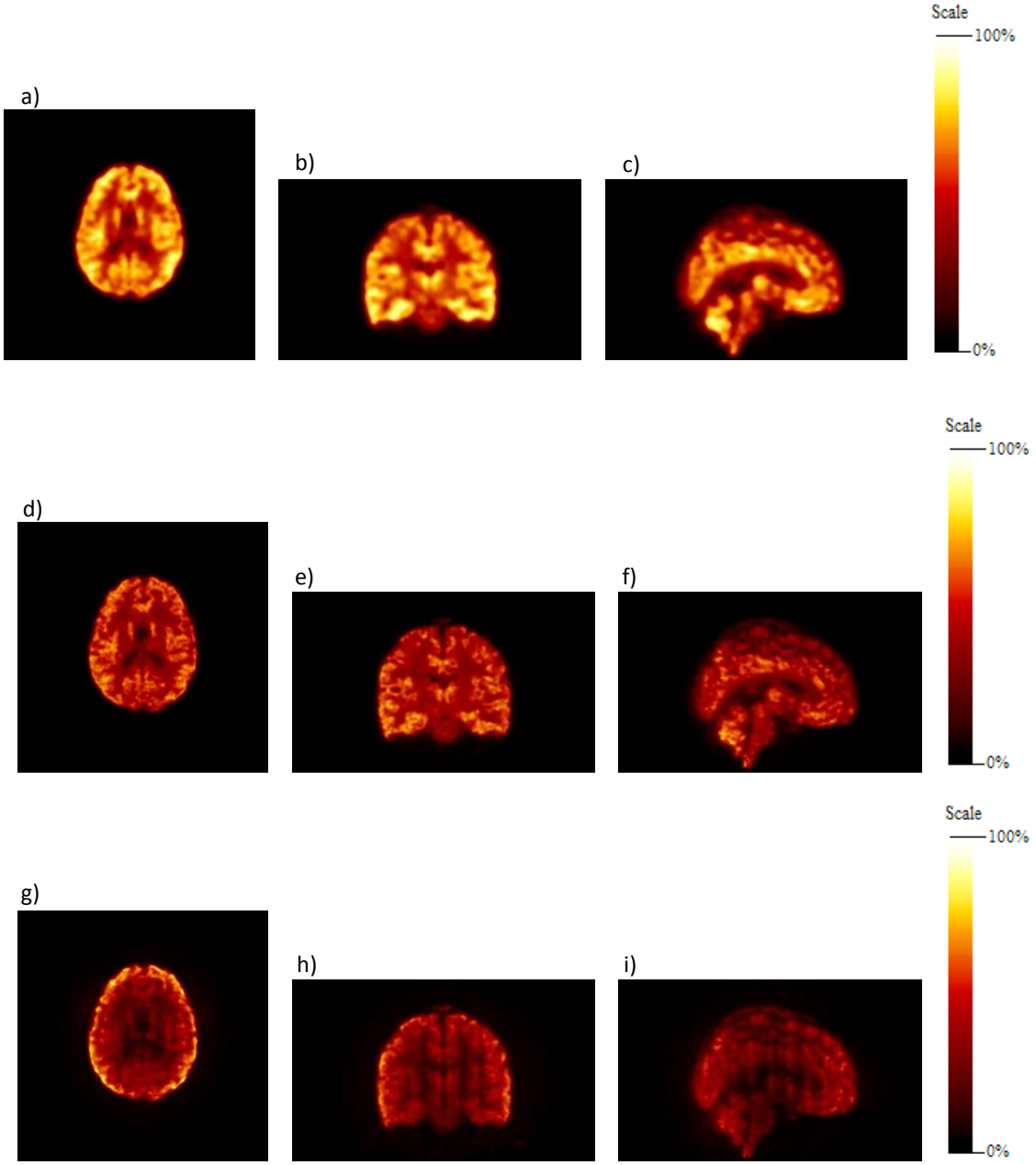

Figure 5. 27: [18F]-FDG images from brain phantom (frame 23): images with the correct attenuation map are in the first row, images with wrong attenuation map in the next row and in the last row the images without attenuation correction are shown. Images are represented in transversal (a), d) and g)), coronal (b), e) and h)) and sagittal views (c), f) and i)). All these images are motionless and filtered using the Gaussian filter with 6 mm.

All the three images are very different. The image with the correct attenuation map (Figure 5. 27 a)-c)) shows much more average intensity of the brain, according with the color scale, and a more detailed outline of the brain. However the circumvolutions of the brain can be seen in images with the correct and with the wrong map attenuation (Figure 5. 27 d)-f)). The image without attenuation

correction (Figure 5. 27 g)-i)) is the most different because exhibits much more noise, artifacts and distortion, showing the importance to correct the attenuation for future analysis. One of the artifact observed in this figure is the prominent activity at brain surface due to relative lack of attenuation at the surfaces compared to deeper structures. As the ITK corrects the motion using intensity values of the images maybe the motion parameters present smaller errors using images without the attenuation correction. This case will be studied below.

Two pairs of images were used to study the influence of attenuation map. The reference frame used was the previous frame to the moved frame i.e. first, the frame 21 was used as reference image and frame 22 as moved image and secondly the frame 22 was used as reference image and frame 23 as moved image. For simulated images with the correct and wrong attenuation map, the correct attenuation map was applied in the reference images. However when it was used moved images without attenuation correction, the reference image also had no attenuation map.

The results of this analysis are shown in Figure 5. 28. A comparison between ITK and PMOD was made using the translation and rotation error sums. Only Normalized Correlation was used because, as proved in previous tests, is the best ITK metric to estimate the motion using one-modality images. As previous mentioned, the simulated motion was 1 mm of translation and 1° of rotation with respect to all three axes and the data used.

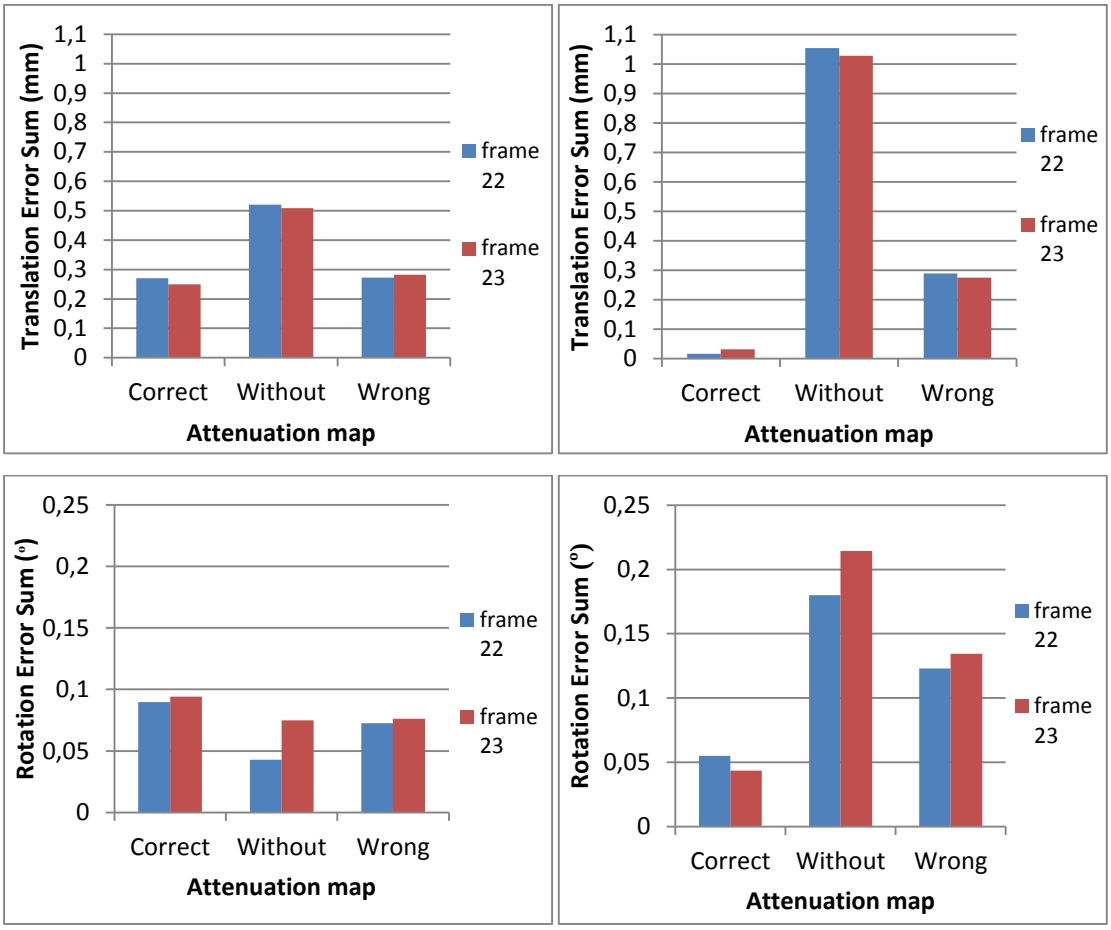

Figure 5. 28: Absolute errors sums (in the three axes) of translation and rotation respectively. These sums were performed for [18F]-FDG dynamic data (brain phantom). Here the motion estimation errors from images without and with the correct attenuation map (with motion) and even images with wrong attenuation map (without motion) are represented. The simulated motion was 1 mm and 1° in x, y and z axes. Only the frame 22 and 23 were corrected using Normalized Correlation ITK metric (left side - 1st column) and using PMOD (right side - 2nd column). The others frames and metrics had the same behavior.

The previous figure demonstrates that the image with the correct attenuation map presents higher errors when the motion is estimated by ITK (comparing to PMOD). However this comparison is not correct since the PMOD does not have the capability to apply the correct attenuation map like ITK. This inability is due to the PMOD correct the motion after the reconstruction so the images had always the wrong attenuation map (map without motion). Therefore the ITK results from the image with the correct attenuation map has to be compared with the PMOD results of the image with the wrong attenuation map. This comparison revealed that ITK displayed better results than PMOD. At the same time, when the images with the wrong attenuation map and with no attenuation correction were compared between the two software, ITK always gets smaller translation and rotation errors sums. Thus the PMOD good outcomes are more depended of the correct attenuation map application in the images which is not possible.

In another analysis, it can be noticed that in most of the cases, the results were worst when no

attenuation map is applied therefore attenuation correction is essential to ITK and PMOD motion estimation. Using PMOD the best results are always shown when the correct attenuation map is applied while using ITK the results are more inconsistent, showing no tendency. However the differences between the results of the three images used (with correct, wrong and without) in ITK analysis are not as big as in PMOD analysis. Using ITK the biggest difference between the three images is 0.25 mm in translation and 0.10º in rotation. Comparatively using PMOD the biggest difference is 1 mm in translation and 0.17º in rotation.

5.3. Acquired data

The Siemens 3T MR-BrainPET is routinely used for PET/MR studies with a variety of radiotracers, such as [18F]-FDG, [18F]-FET, [11C]-Raclopride (RC), [11C]-Flumazenil (DF), [15O]-Water. As the aim of this work is to find out if ITK is able to replace the PMOD in motion correction at FZJ, all these exams are tested here. Filtered images (Gaussian filter) with 41 iterations from two patients of each PET/MR exam were used. The output reconstruction images were used to confirm if this software can be used in clinical practice. Conversion programs from flat format to interfile were used.

In order to select the reference frame, the dynamic dataset was visualized frame by frame in PMOD. The reference image was set as the one immediately before to the frame with the first detected motion. This is a very subjective method and thus its accuracy is not clear. However for this study, this is not important because the same reference frame was used in PMOD and ITK. Only Normalized Correlation ITK metric was used in this analysis while the Mean Squares metric was used in PMOD motion estimation.

The next figures (Figure 5. 29 - Figure 5. 33) show filtered images from the five different exams. Here transversal, coronal and sagittal views are represented.

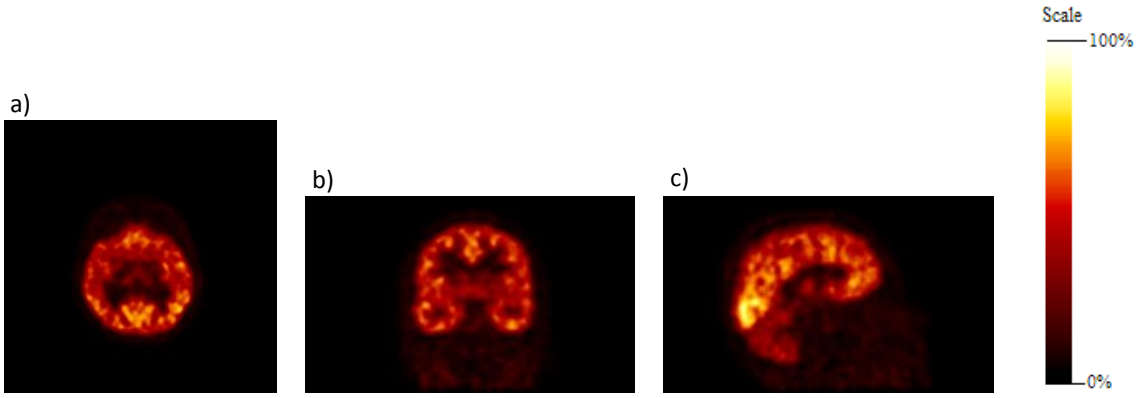

Figure 5. 29: Clinical images from an exam using [11C]-Flumanzenil. Transversal (a)), coronal (b)) and sagittal (c)) views are represented.

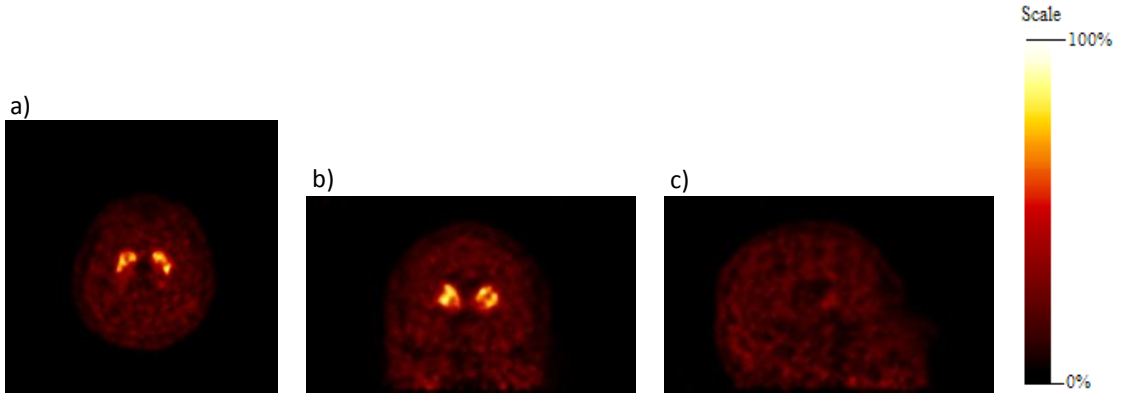

Figure 5. 30: Clinical images from an exam using [11C]-Raclopride. Transversal (a)), coronal (b)) and sagittal (c)) views are represented.

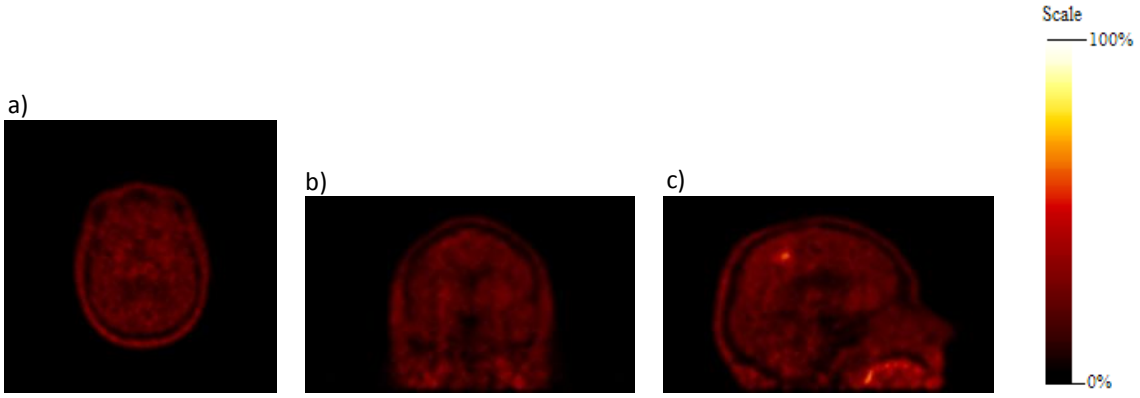

Figure 5. 31: Clinical images from [18F]-FET exam. Transversal (a)), coronal (b)) and sagittal (c)) views are represented.

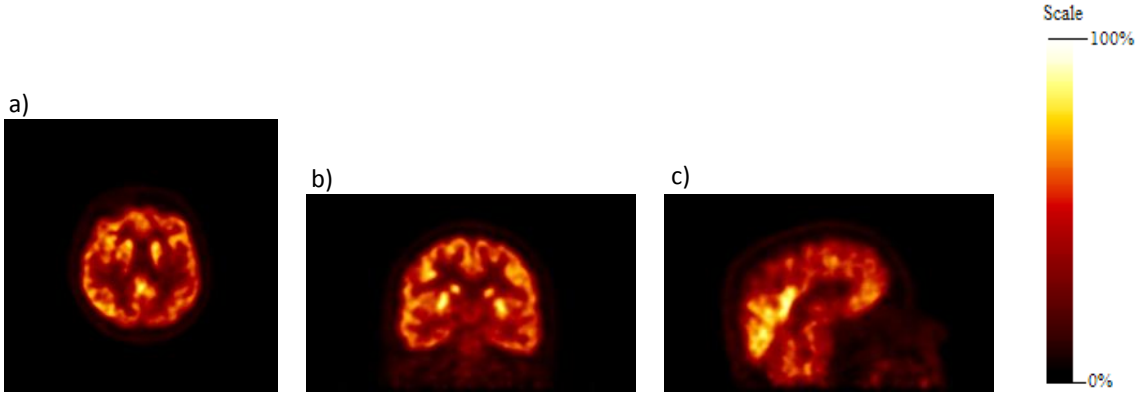

Figure 5. 32: Clinical images from [18F]-FDG exam. Transversal (a)), coronal (b)) and sagittal (c)) views are represented.

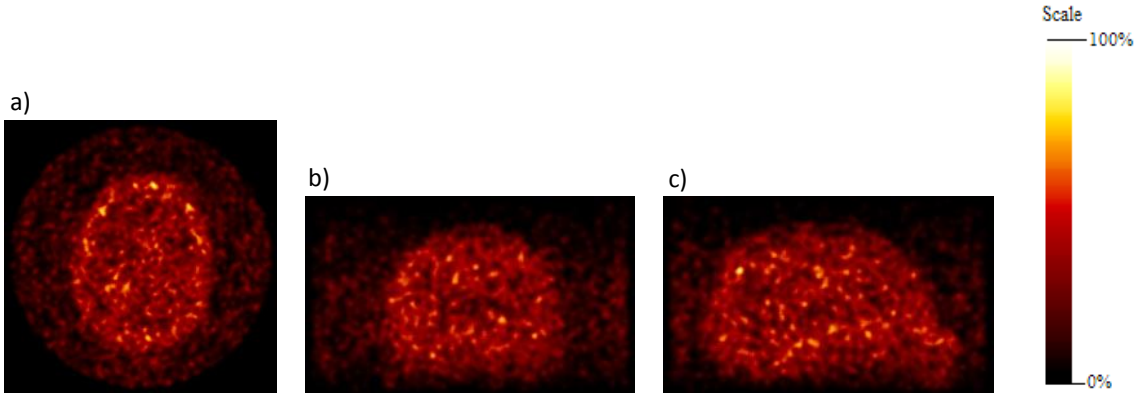

Figure 5. 33: Clinical images from an exam using [15O]-Water. Transversal (a)), coronal (b)) and sagittal (c)) views are represented.

The five examinations showed very different images. For instance, same brain region have different intensities on the different exams; only some of them mark brain structures visibly; some images reveal higher noise levels than others, among others. The [15O]-Water exam shows images with very noise, the brain cannot even be recognized in the figure (Figure 5. 33).

The real different motions that the patients made during the acquisition are unknown making impossible the calculation of the errors. Therefore in order to test this data, a comparison between ITK results and PMOD results was made. Then the translation and rotation absolute errors sums consist in the difference between the two software results and they are shown in Figure 5. 34 to Figure 5. 38. The two patient for each exam are represented in x-axis of the graphics.

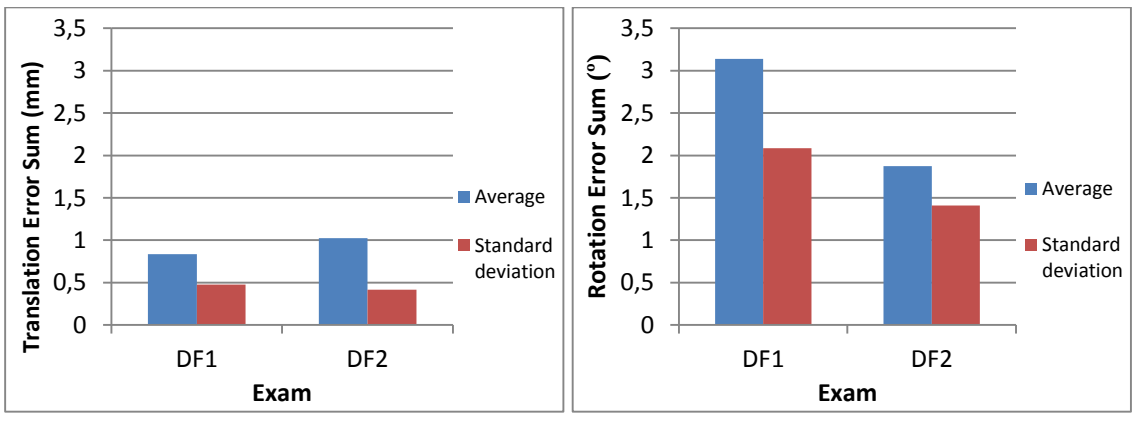

Figure 5. 34: Average and standard deviation of errors from [11C]-Flumanzenil exams. The first graphic corresponds to translation and the second to rotation error sums (in the three axes). These sums are the mean of all the frames acquired during the exam. DF1 and DF2 represent the two different patients.

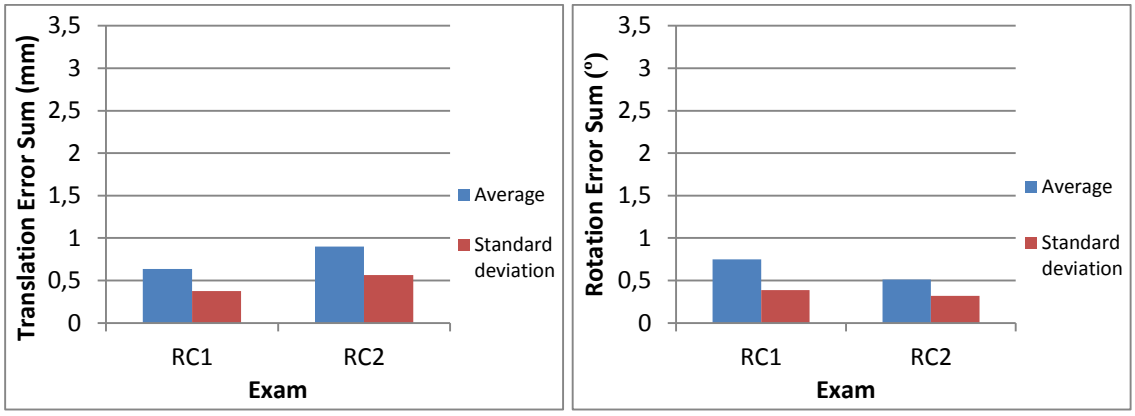

Figure 5. 35: Average and standard deviation of errors from [11C]-Raclopride exams. The first graphic corresponds to translation and the second to rotation error sums (in the three axes). These sums were the mean of all the frames acquired during the exam. RC1 and RC2 represent the two different patients.

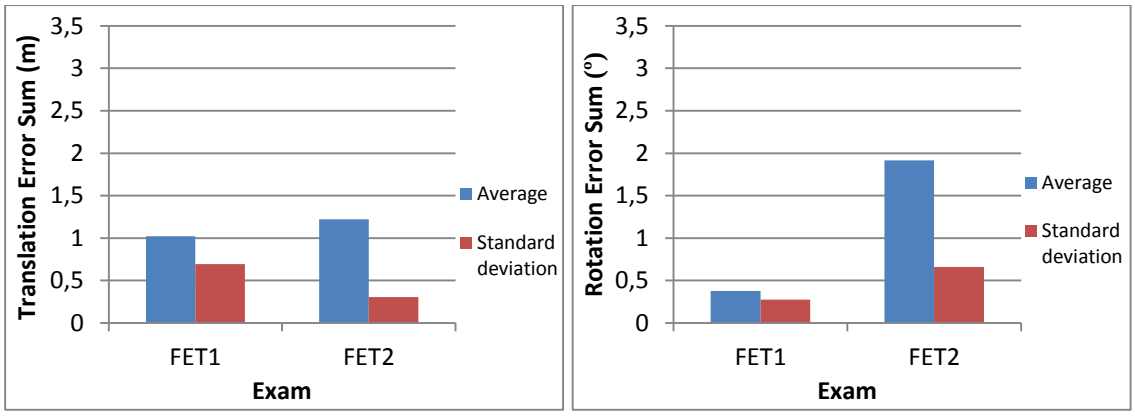

Figure 5. 36: Average and standard deviation of errors from [18F]-FET exams. The first graphic corresponds to translation and the second to rotation error sums (in the three axes). These sums were the mean of all the frames acquired during the exam. FET1 and FET2 represent the two different patients.

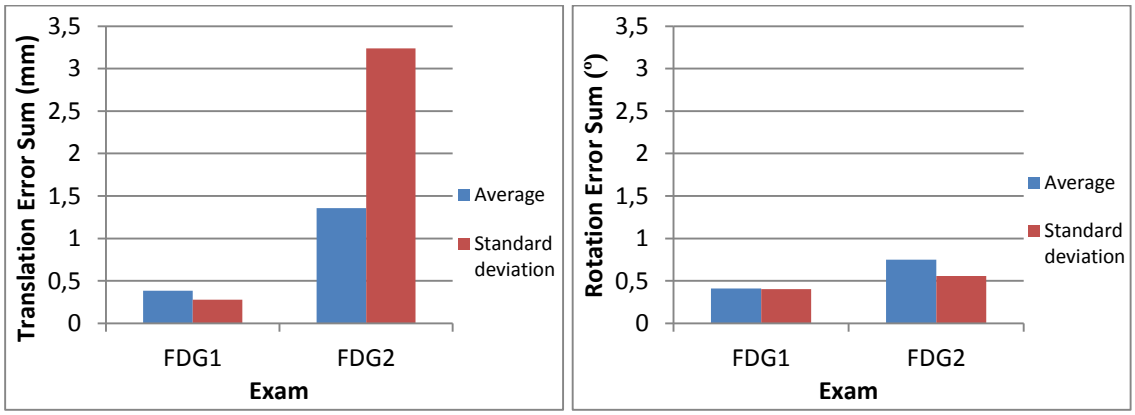

Figure 5. 37: Average and standard deviation of errors from [18F]-FDG exams. The first graphic corresponds to translation and the second to rotation error sums (in the three axes). These sums were the mean of all the frames acquired during the exam. FDG1 and FDG2 correspond the two different patients.

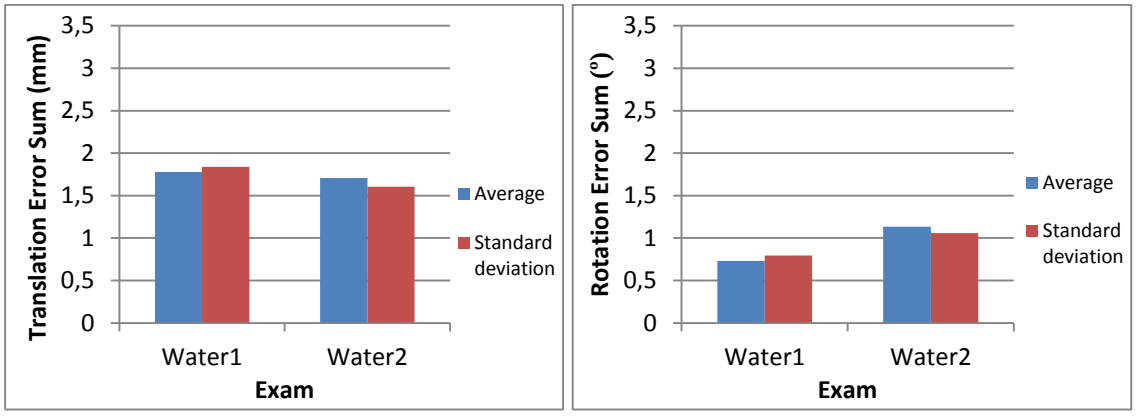

Figure 5. 38: Average and standard deviation of errors from [15O]-Water exams. The first graphic corresponds to translation and the second to rotation error sums (in the three axes). These sums were the mean of all the frames acquired during the exam. Water1 and Water2 correspond the two different patients.

The [15O]-Water exam (Figure 5. 38) shows average and standard deviation higher than the other four examinations in translation. This is because the [15O]-Water exam has bigger noise than the other images. However in rotation the error sum are higher in [11C]-Flumazenil exam (Figure 5. 34), maybe because the patient experienced large motions or the images has low statistics therefore the ITK cannot estimate the motion with accuracy especially in rotation. Patient 2 of the [18F]-FDG exam in the translation analysis (Figure 5. 37) shows the standard of error bigger than the average, this is because there are some outliers in the data. The same occurs with the patient one of water exam in both translation and rotation analysis. In both [18F]-FET and [18F]-FDG exams the results of the two patient are very different, maybe one of them performed bigger motions and ITK presents larger errors when estimate larger motions.

Even using real data the mean difference between the error sums of the two software is around 1.2 mm in translation and 1° in rotation. These values correspond to the average of the translation and rotation error sums (of the two patients) represented on the graphics.

In conclusion the results from the five examinations show small differences between ITK and PMOD. Therefore ITK is compatible with all reconstructed BrainPET images used in clinical practice of Forschungszentrum Juelich.

CHAPTER 6

Conclusion and Future work

Some exams have long acquisition time, such as PET, being difficult for the patients to stay still during all the exam. Subject motion degrades the image quality and this is a significant source of quantitative error in PET images. Therefore motion correction is mandatory for precise diagnostics and treatment. Physical devices are used to force the patients not to move and this can deeply influence the range of motion. However this physical limitations are not sufficient to avoid the motion. The brain has several small structures, therefore even a very small movement introduces a significant blurring on the image.

Over the years several software were proposed to correct the motion, some of them corrected the data after the reconstruction, e.g. PMOD, and others can be implemented in the reconstruction, such as ITK. Through a software which corrects motion during reconstruction, the lines-of-response affected by the motion are individually corrected, empowering a more accurate correction. The global objective of the thesis is to confirm if ITK is able to correct the motion and if it can replace the software used today in clinical and research practice at Forschungszentrum Juelich, PMOD.

The results obtained in this thesis show that ITK is a viable method for motion parameters estimation for acquisitions with the Siemens 3TMR-BrainPET scanner. This is proved by using simulated and acquired data ([18F]-FDG, [18F]-FET, [11C]-Flumazenil, [11C]-Raclopride and [15O]-Water). Besides PET images, MR images were also tested: EPI clinical images and simulated images from FLASH sequences. Relatively to PET images, ITK shows very small errors when images with high statistics were used. Higher image statistics, smaller are the absolute errors of the motion parameters. All this is justified by the presence of less noise in images with high statistics. The results of motion estimation using MR images are better than using PET images with low statistics. Therefore one possibility, in PET/MRI context, is to use EPI images

to correct the motion for the first frames of dynamic PET and the PET images when the frames have sufficient statistics.

There are several metrics available for ITK motion estimation and the best choice for each problem has to be found. As only a few millimetres of motion affect the image quality, the ITK metric used is an important factor to take into account because it can improve the motion estimation i.e. reduce the absolute errors. Three metrics were compared: Normalized Correlation, Mean Squares and Mutual Information. Observing the results Normalized Correlation is the best metric for one-modality images analysis while Mutual Information is the best for a multi-modality analyses. The comparison between ITK and PMOD reveals that, in generally, PMOD gets better results i.e. smaller absolute errors on motion estimation, especially for larger motions which are not expected when motion control systems are used. Despite of that, PMOD results are more dependent of applying the correct attenuation map i.e. the attenuation map that considerers the simulated motion, however if the motion was estimated by PMOD this map is not applied.

ITK has some limitations such as images with large motions because displacements happen, or images with low statistics because a high level of noise is present. However this software has important advantages over the PMOD. ITK can be implemented in the reconstruction script, saving time in image reconstruction and the technical staff who performs the reconstruction does not have to know how to manipulate the PMOD tool. Using PMOD an additional and hard-working step is always required. At the same time the ITK is a free software while each license of PMOD has very high cost (http://pmod.com/technologies/distribution/orderForm/ordering.php?p_licenseType=Commercial).

ITK can provide image based corrections, which allow to use easily PET or MR images for motion correction. The motion parameters extracted from ITK can be used to correct the motion in OSEM 3D using PRESTO or using the provider (Siemens) reconstruction after or within reconstruction (e.g. (Scheins et al. 2013)) without using tracking devices. The overall conclusion is that ITK is able to estimate the motion with a similar accuracy as PMOD, so for motion correction ITK is able to replace PMOD.

As future work, it is essential to improve the ITK results, e.g. by increasing the number of iterations. In this work it was proved the importance of the reference frame choice since the results are deeply influence by that. Therefore for using ITK as motion estimation is essential to know which frame of reference should be used. A study about this issue is very important, bringing essential information.

APPENDIX

Posters in Conferences

- M. Botelho, L. Caldeira, J. Scheins, N. Matela, E. Rota Kops, N. J. Shah, PET Motion Correction using PRESTO with ITK Motion Estimation, 6th Workshop on Biomedical Engineering, 5th April 2014, Lisbon, Portugal
- M. Botelho, L. Caldeira, J. Scheins, N. Matela, E. Rota Kops, N. J. Shah, PET Motion Correction using PRESTO with ITK Motion Estimation, 3rd Conference on PET/MR and SPECT/MR, 19th -21st May 2014, Kos island, Greece
- M. Botelho, L. Caldeira, J. Scheins, N. Matela, E. Rota Kops, N. J. Shah, PET Motion Correction using PRESTO with ITK Motion Estimation, INM-retreat, 1st -2nd July 2014, Forschungszentrum Juelich, Germany
- M. Botelho, L. Caldeira, J. J. Scheins, N. Matela, E. Rota Kops, N. J. Shah, PET/MR Motion Correction with Image-Based ITK Motion Estimation, IEEE Nuclear Science Symposium & Medical Imaging Conference, 21ST Symposium on Room-Temperature Semiconductor X-Ray and Gamma-Ray Detectors, 8th-15th November 2014, Washington State Convention Center, Seattle, WA USA

LIST OF FIGURES

LIST OF TABLES

REFERENCES

Akbarzadeh, A. et al., 2013. Evaluation of whole-body MR to CT deformable image registration. *Journal of applied clinical medical physics / American College of Medical Physics*, 14(4), p.4163.

Andres, P. a & Isoardi, R. a, 2007. Using ITK platform for medical image registration. *Journal of Physics: Conference Series*, 90, p.012056.

Antoch, G. & Bockisch, A., 2009. Combined PET/MRI: a new dimension in whole-body oncology imaging? *European journal of nuclear medicine and molecular imaging*, 36 Suppl 1, pp.S113–20.

Aubert-Broche, B., Evans, A.C. & Collins, L., 2006. A new improved version of the realistic digital brain phantom. *NeuroImage*, 32, pp.138–145.

Baete, K. et al., 2004. Evaluation of anatomy based reconstruction for partial volume correction in brain FDG-PET. *NeuroImage*, 23, pp.305–317.

Bai, B. et al., 2002. Model-based normalization for iterative 3D PET image reconstruction. *Physics in medicine and biology*, 47, pp.2773–2784.

Bailey, D., 2005. Positron Emission Tomography: Basic Sciences. *Springer*.

Beer, A.J. et al., 2007. [18F]galacto-RGD positron emission tomography for imaging of alphavbeta3 expression on the neovasculature in patients with squamous cell carcinoma of the head and neck. *Clinical cancer research : an official journal of the American Association for Cancer Research*, 13(22 Pt 1), pp.6610–6.

Beer, A.J. et al., 2005. Biodistribution and pharmacokinetics of the alphavbeta3-selective tracer 18F-galacto-RGD in cancer patients. *Journal of Nuclear Medicine*.

Bendriem, B. & Townsend, D.W., 1998. The theory and practice of 3D PET. *Springer Science & Business Media*.

Bloomfield, P.M. et al., 2003. The design and implementation of a motion correction scheme for neurological PET. *Physics in medicine and biology*, 48, pp.959–978.

Bluml, S. et al., 1996. A Comparison of Magnetization Prepared 3D Gradient-Echo (MP-RAGE) Sequences for Imaging of Intracranial Lesions. *Magnetic Resonance Imaging*, 14(3), pp.329–335.

Borthakur, A. et al., 2006. A Pulse Sequence for Rapid In Vivo Spin-Locked MRI. *Journal of Magnetic Resonance Imaging*, 23(4), pp.591–596.

Boss, A. et al., 2010. Hybrid PET/MRI of intracranial masses: initial experiences and comparison to PET/CT. *Journal of nuclear medicine : official publication, Society of Nuclear Medicine*, 51(8), pp.1198–205.

Brown, M. a. & Semelka, R.C., 2010. MRI: Basic Principles and Applications. *JOHN WILEY & SONS, INC.*

Bühler, P. et al., 2004. An accurate method for correction of head movement in PET. *IEEE Transactions on Medical Imaging*, 23(8), pp.1176–1185.

Bushberg, J.T. et al., 2002. The Essential Physics of Medical Imaging. *Second Edition*, p.2015.

Caldeira, L. et al., 2013. Evaluation of two methods for using MR information in PET reconstruction. *Nuclear Instruments and Methods in Physics Research Section A: Accelerators, Spectrometers, Detectors and Associated Equipment*, 702, pp.141–143.

Caldeira, L. et al., 2010. Maximum a Posteriori Reconstruction using PRESTO and PET/MR data acquired Simultaneously with the 3TMR-BrainPET. *IEEE Nuclear Science Symposuim & Medical Imaging Conference*, pp.2879–2884.

Caldeira, L. et al., 2012. Reconstruction of PET data acquired with the BrainPET using STIR. In *IEEE Nuclear Science Symposium Conference Record*. pp. 2327–2329.

Carson, R.E. et al., 2003. Design of a motion-compensation OSEM list-mode algorithm for resolution-recovery reconstruction for the HRRT. *2003 IEEE Nuclear Science Symposium. Conference Record (IEEE Cat. No.03CH37515)*, 5, pp.3281–3285.

Catana, C. et al., 2011. MRI-assisted PET motion correction for neurologic studies in an integrated MR-PET scanner. *Journal of nuclear medicine : official publication, Society of Nuclear Medicine*, 52(1), pp.154–61.

Cheng, J.C. & Laforest, R., 2013. Using ITK to obtain motion transform in anatomically guided PET motion correction for simultaneous PET/MR. *IEEE Nuclear Science Symposium Conference Record*.

Cherry, S., Sorenson, J. & Phelps, M., 2012. *Physics in Nuclear Medicine*,

Cherry, S.R., 2009. Multimodality imaging: beyond PET/CT and SPECT/CT. *Seminars in nuclear medicine*, 39(5), pp.348–53.

Cherry, S.R. & Huang, S.C., 1995. Effects of scatter on model parameter estimates in 3D PET studies of the human brain. *IEEE Transactions on Nuclear Science*, 42(4), pp.1174–1179.

Cherry, S.R., Louie, a. Y. & Jacobs, R.E., 2008. The Integration of Positron Emission Tomography With Magnetic Resonance Imaging. *Proceedings of the IEEE*, 96(3), pp.416–438.

Chun, S.Y. et al., 2012. MRI-Based Nonrigid Motion Correction in Simultaneous PET/MRI. *Journal of Nuclear Medicine*, 53, pp.1284–1291.

Cloquet, C. et al., 2010. Non-Gaussian space-variant resolution modelling for list-mode reconstruction. *Physics in medicine and biology*, 55(17), pp.5045–66.

Courreges, F., 2011. Design of a Bio-Inspired 3D Orientation Coordinate System and Application in Robotised Tele-Sonography. *Robot Arms*.

Daftary, A., 2010. PET-MRI: Challenges and new directions. *Indian Journal of Nuclear Medicine*, 25(1), pp.3–5.

Damadian, R., Goldsmith, M. & Minkoff, L., 1977. NMR in cancer: XVI. FONAR image of the live human body. *Physiological chemistry and physics*, 9(1), pp.97–100, 108.

Daube-Witherspoon, M. et al., 1990. Correction for motion distortion in PET by dynamic monitoring of patient position. *Journal of Nuclear Medicine*, 31(816).

Defrise, M. et al., 1991. A normalization technique for 3D PET data. *Physics in medicine and biology*, 36, pp.939–952.

Fahey, F.H., 2002. Data acquisition in PET imaging. *Journal of nuclear medicine technology*, 30(2), pp.39–49.

Ferreira, N.C. et al., 2002. A hybrid scatter correction for 3D PET based on an estimation of the distribution of unscattered coincidences: implementation on the ECAT EXACT HR+. *Physics in medicine and biology*, 47, pp.1555–1571.

Freire, L., 2003. Registration of Functional MRI Images. *Universidade de Lisboa, Faculdade de Ciências*.

Fulton, R.R. et al., 2002. Correction for head movements in positron emission tomography using an optical motion-tracking system. *IEEE Transactions on Nuclear Science*, 49, pp.58–62.

Gravel, P., Verhaeghe, J. & Reader, A.J., 2013. 3D PET image reconstruction including both motion correction and registration directly into an MR or stereotaxic spatial atlas. *Physics in medicine and biology*, 58, pp.105–26.

Guerreiro, C. et al., 2009. Development of component-based normalization correction for the clear-PEM system. *IEEE Nuclear Science Symposium Conference Record*, pp.2846–2848.

Herzog, H. et al., 2011. High resolution BrainPET combined with simultaneous MRI. *Nuklearmedizin. Nuclear medicine*, 50(2), pp.74–82.

Herzog, H. et al., 2005. Motion artifact reduction on parametric PET images of neuroreceptor binding. *Journal of nuclear medicine : official publication, Society of Nuclear Medicine*, 46, pp.1059–1065.

Herzog, H., 2012. PET/MRI: Challenges, solutions and perspectives. *Zeitschrift fur Medizinische Physik*, 22(January), pp.281–298.

Herzog, H. et al., 2010. The current state, challenges and perspectives of MR-PET. *NeuroImage*, 49(3), pp.2072–82.

Herzog, H., Stoffels, G. & Kaffanke, J., 2014. Simultaneous FET-PET and fMRI in brain tumors using a PET / MRI hybrid scanner. *Journal of Nuclear Medicine*, 51(1002), pp.1–2.

Hicks, R., Lau, E. & Binns, D., 2007. Hybrid imaging is the future of molecular imaging. *Biomedical imaging and intervention journal*, 3(3), p.e49.

Hofmann, M. et al., 2008. MRI-based attenuation correction for PET/MRI: a novel approach combining pattern recognition and atlas registration. *Journal of nuclear medicine : official publication, Society of Nuclear Medicine*, 49, pp.1875–1883.

Jadvar, H. & Colletti, P.M., 2014. Competitive advantage of PET/MRI. *European journal of radiology*, 83(1), pp.84–94.

Jin, X. et al., 2013. Evaluation of motion correction methods in human brain PET imaging--a simulation study based on human motion data. *Medical physics*, 40(10), p.102503.

Johnson, H.J., Mccormick, M.M. & Ibánez, L., 2015. The ITK Software Guide Book 1 : Introduction and Development Guidelines Fourth Edition Updated for ITK version 4 . 6.

Kolb, A. et al., 2012. Technical performance evaluation of a human brain PET/MRI system. *European radiology*, 22(8), pp.1776–88.

Kolbitsch, C. et al., 2014. A 3D MR-acquisition scheme for nonrigid bulk motion correction in simultaneous PET-MR. *Medical physics*, 41(8), p.082304.

Kops, E.R. & Herzog, H., 2007. Alternative methods for attenuation correction for PET images in MR-PET scanners. *IEEE Nuclear Science Symposium Conference Record*, 6, pp.4327–4330.

Kwan, R.K.-S., Evans, A.C. & Pike, G.B., 1996. An Extensible MRI Simulator for Post - Processing Evaluation. *Lecture Notes in Computer Science*, 1131, pp.135–140.

De Lange, E.E. et al., 1991. Magnetization prepared rapid gradient-echo (MP-RAGE) MR imaging of the liver: comparison with spin-echo imaging. *Magnetic resonance imaging*, 9, pp.469–476.

Liu, Y. et al., 2014. An ITK implementation of a physics-based non-rigid registration method for brain deformation in image-guided neurosurgery. *Frontiers in neuroinformatics*, 8(33).

Loening, A.M. & Gambhir, S.S., 2003. AMIDE: A Free Software Tool for Multimodality Medical Image Analysis. *Molecular Imaging*, 2(3), pp.131–137.

Maclaren, J. et al., 2013. Prospective motion correction in brain imaging: A review. *Magnetic Resonance in Medicine*, 69, pp.621–636.

Malone, I.B. et al., 2011. Attenuation correction methods suitable for brain imaging with a PET/MRI scanner: a comparison of tissue atlas and template attenuation map approaches. *Journal of nuclear medicine : official publication, Society of Nuclear Medicine*, 52(7), pp.1142–9.

Maramraju, S.H. et al., 2011. Small animal simultaneous PET/MRI: initial experiences in a 9.4 T microMRI. *Physics in medicine and biology*, 56(8), pp.2459–80.

Mattes, D. & Haynor, D., 2001. Nonrigid multimodality image registration. *Medical …*, 4322, pp.1609–1620.

McCormick, M. et al., 2014. ITK: enabling reproducible research and open science. *Frontiers in neuroinformatics*, 8(13).

Menda, Y. et al., 2009. Kinetic analysis of 3'-deoxy-3'-(18)F-fluorothymidine ((18)F-FLT) in head and neck cancer patients before and early after initiation of chemoradiation therapy. *Journal of nuclear medicine : official publication, Society of Nuclear Medicine*, 50(7), pp.1028–35.

Mendes, L., 2012. Positron Emission Tomography: Image Reconstruction based on multiscale and resolution methods. *UNIVERSITY OF COIMBRA*.

Menke, M., Atkins, M.S. & Buckley, K.R., 1996. Compensation methods for head motion detected during pet imaging. *IEEE Transactions on Nuclear Science*, 43, pp.310–317.

Michel, C. et al., 1998. Preserving Poisson characteristics of PET data with weighted OSEM reconstruction. *IEEE Nuclear Science Symposium and Medical Imaging*, 2, pp.1323–1329.

Miese, F. et al., 2011. Hybrid 18F-FDG PET-MRI of the hand in rheumatoid arthritis: initial results. *Clinical rheumatology*, 30(9), pp.1247–50.

Moehrs, S. et al., 2008. Multi-ray-based system matrix generation for 3D PET reconstruction. *Physics in medicine and biology*, 53(23), pp.6925–45.

Mourik, J., 2009. Image Derived Input Functions for Cerebral PET Studies. *VU university medical center, Amsterdam*.

Mourik, J.E.M. et al., 2009. Off-line motion correction methods for multi-frame PET data. *European Journal of Nuclear Medicine and Molecular Imaging*, 36(2009), pp.2002–2013.

Muller, H. et al., 2006. Automated Object Extraction for Medical Image Retrieval Using the Insight Toolkit (ITK). *Information Retrieval Technology*.

Nelson, F. et al., 2008. 3D MPRAGE improves classification of cortical lesions in multiple sclerosis. *Multiple sclerosis (Houndmills, Basingstoke, England)*, 14(9), pp.1214–1219.

Nensa, F. et al., 2014. Clinical applications of PET/MRI: current status and future perspectives. *Diagnostic and interventional radiology (Ankara, Turkey)*, 20(5), pp.438–47.

Noonan, P., 2014. An Investigation Into Motion Correction Schemes for High Resolution 3D PET and PET/CT. *University of Manchester*.

Oakes, T.R., Sossi, V. & Ruth, T.J., 1998. Normalization for 3D PET with a low-scatter planar source and measured geometric factors. *Physics in medicine and biology*, 43, pp.961–972.

Olesen, O.V., 2011. Markerless 3D Head Tracking for Motion Correction in High Resolution PET Brain Imaging. *Faculty of Health Sciences, University of Copenhagen*.

Panin, V.Y. et al., 2006. Fully 3-D PET reconstruction with system matrix derived from point source measurements. *IEEE Transactions on Medical Imaging*, 25(7), pp.907–921.

Panin, V.Y., Chen, M. & Michel, C., 2007. Simultaneous update iterative algorithm for variance reduction on random coincidences in PET. *IEEE Nuclear Science Symposium Conference Record*, 4, pp.2807–2811.

Pauleit, D. et al., 2005. O-(2-[18F]fluoroethyl)-L-tyrosine PET combined with MRI improves the diagnostic assessment of cerebral gliomas. *Brain*, 128, pp.678–687.

Picard, Y. & Thompson, C.J., 1997. Motion correction of PET images using multiple acquisition frames. *IEEE transactions on medical imaging*, 16(2), pp.137–144.

Pichler, B. et al., 2008. PET/MRI : The Next Generation of Multi-Modality Imaging? *The Journal of Nuclear Medicine*, 38(3), pp.199–208.

Pichler, B.J. et al., 2006. Performance test of an LSO-APD detector in a 7-T MRI scanner for simultaneous PET/MRI. *Journal of nuclear medicine : official publication, Society of Nuclear Medicine*, 47, pp.639–647.

Pichler, B.J. et al., 2008. Positron emission tomography/magnetic resonance imaging: the next generation of multimodality imaging? *Seminars in nuclear medicine*, 38(3), pp.199–208.

Powell, M.J.D., 1964. A Method for Minimizing a Sum of Squares of Non-Linear Functions Without Calculating Derivatives. *The Computer Journal*, 7(2), pp.155–162.

Pratx, G. et al., 2006. Fully 3-D List-Mode OSEM Accelerated by Graphics Processing Units. *IEEE Nuclear Science Symposium Conference Record*, pp.2196–2202.

Qi, J.Q.J. & Huesman, R.H., 2002. List mode reconstruction for PET with motion compensation: a simulation study. *Proceedings IEEE International Symposium on Biomedical Imaging*, pp.413–416.

Qin, L. et al., 2009. Prospective head-movement correction for high-resolution MRI using an in-bore optical tracking system. *Magnetic Resonance in Medicine*, 62(4), pp.924–934.

Rahmim, A., 2005. Advanced Motion Correction Methods in PET (Review Article). *Iranian Journal of Nuclear Medicine*, 13(24), pp.1–17.

Rahmim, A. et al., 2004. Motion compensation in histogram-mode and list-mode EM reconstructions: Beyond the event-driven approach. *IEEE Transactions on Nuclear Science*, 51(5), pp.2588–2596.

Rahmim, A. et al., 2008. System matrix modelling of externally tracked motion. *Nuclear Medicine Communications*, 29(6), pp.574–581.

Rahmim, A., Qi, J. & Sossi, V., 2013. Resolution modeling in PET imaging: theory, practice, benefits, and pitfalls. *Medical physics*, 40(6), p.064301.

Rahmim, A., Rousset, O. & Zaidi, H., 2007. Strategies for Motion Tracking and Correction in PET. *PET Clinics*, 2, pp.251–266.

Rao, K. et al., 2005. Impact of motion correction on the quantitative analysis of DCE-MR Images. *The Insight Journal*.

Riddell, C. et al., 2001. Noise reduction in oncology FDG PET images by iterative reconstruction: a quantitative assessment. *Journal of nuclear medicine : official publication, Society of Nuclear Medicine*.

Sauter, A.W. et al., 2010. Combined PET/MRI: one step further in multimodality imaging. *Trends in molecular medicine*, 16(11), pp.508–15.

Scheins, J. et al., 2013. MR-guided PET motion correction in LOR space using generic projection data for image reconstruction with PRESTO. *Nuclear Instruments and Methods in Physics Research Section A: Accelerators, Spectrometers, Detectors and Associated Equipment*, 702, pp.64–66.

Scheins, J.J. et al., 2009. High resolution PET image reconstruction for the siemens MR/PET-hybrid BrainPET scanner in LOR space. In *IEEE Nuclear Science Symposium Conference Record*. pp. 2981–2984.

Scheins, J.J. et al., 2011. PET motion correction in LOR space using scanner-independent, adaptive projection data for image reconstruction with PRESTO. *2011 IEEE Nuclear Science Symposium Conference Record*, pp.4099–4101.

Scheins, J.J. & Herzog, H., 2008. PET reconstruction software toolkit - PRESTO a novel, universal C++ library for fast, iterative, fully 3D PET image reconstruction using highly compressed, memory-resident system matrices. In *IEEE Nuclear Science Symposium Conference Record*. pp. 4147–4150.

Scheins, J.J., Herzog, H. & Shah, N.J., 2011. Fully-3D PET image reconstruction using scanner-independent, adaptive projection data and highly rotation-symmetric voxel assemblies. *IEEE transactions on medical imaging*, 30(3), pp.879–92.

Schlemmer, H.-P.W. et al., 2008. Simultaneous MR/PET imaging of the human brain: feasibility study. *Radiology*, 248(3), pp.1028–1035.

Schmand, M. et al., 2007. BrainPET: First human tomograph for simultaneous (functional) PET and MR imaging. *Journal of Nuclear Medicine*, 48(1002), p.45P.

Schnell, O. et al., 2009. Imaging of integrin alpha(v)beta(3) expression in patients with malignant glioma by [18F] Galacto-RGD positron emission tomography. *Neuro-oncology*, 11(6), pp.861–70.

Schwenzer, N.F. et al., 2012. Simultaneous PET/MR imaging in a human brain PET/MR system in 50 patients--current state of image quality. *European journal of radiology*, 81(11), pp.3472–8.

Shah, N.J. et al., 2014. Effects of magnetic fields of up to 9.4 T on resolution and contrast of PET images as measured with an MR-BrainPET. *PloS one*, 9(4).

Shao, Y. et al., 1997. Development of a PET detector system compatible with MRI/NMR systems. *IEEE Transactions on Nuclear Science*, 44(3), pp.1167–1171.

Shao, Y. et al., 1997. Simultaneous PET and MR imaging. *Physics in Medicine and Biology*, 42(10), pp.1965–1970.

Silva, N., 2012. On the Use of Image Derived Input Function for Quantitative PET Imaging with a Simultaneous Measuring MR-BrainPET. *Universidade de Lisboa, Faculdade de Ciências*.

Soret, M., Bacharach, S.L. & Buvat, I., 2007. Partial-volume effect in PET tumor imaging. *Journal of nuclear medicine : official publication, Society of Nuclear Medicine*, 48(6), pp.932–945.

Suetens, P., 2009. Fundamentals of Medical Imaging. *Cambridge University Press*, 2nd Editio.

Tellmann, L. et al., 2011. The effect of MR surface coils on PET quantification in whole-body PET/MR: Results from a pseudo-PET/MR phantom study. *Medical Physics*, 38(5), p.2795.

Thielemans, K., Mustafovic, S. & Schnorr, L., 2003. Image reconstruction of motion corrected sinograms. *2003 IEEE Nuclear Science Symposium. Conference Record (IEEE Cat. No.03CH37515)*, 4, pp.2401–2406.

Todd, C.A. et al., 2009. An analysis of medical image processing methods for segmentation of the inner ear. *University of Wollongong in Dubai*, pp.213–218.

Townsend, D.W., 2008. Multimodality imaging of structure and function. *Physics in medicine and biology*, 53, pp.R1–R39.

Tsoumpas, C. et al., 2010. Simultaneous PET-MR acquisition and MR-derived motion fields for correction of non-rigid motion in PET. *Annals of nuclear medicine*, 24(10), pp.745–50.

Ullisch, M.G. et al., 2012. MR-based PET motion correction procedure for simultaneous MR-PET neuroimaging of human brain. *PloS one*, 7(11), p.e48149.

Ullisch, M.G. et al., 2013. MR-guided data framing for PET motion correction in simultaneous MR–PET: A preliminary evaluation. *Nuclear Instruments and Methods in Physics Research Section A: Accelerators, Spectrometers, Detectors and Associated Equipment*, 702, pp.67–69.

User's Guide PMOD, P.F., 2008. PMOD Image Fusion (PFUS). *Pmod Technologies, version 3.6*.

Van der Veldt, A. a M., Smit, E.F. & Lammertsma, A. a, 2013. Positron Emission Tomography as a Method for Measuring Drug Delivery to Tumors in vivo: The Example of [(11)C]docetaxel. *Frontiers in oncology*, 3(August), p.208.

Watson, C.C., 2000. New, faster, image-based scatter correction for 3D PET. *IEEE Transactions on Nuclear Science*, 47(4), pp.1587–1594.

Wehner, J. et al., 2014. PET/MRI insert using digital SiPMs: Investigation of MR-compatibility. *Nuclear Instruments and Methods in Physics Research Section A: Accelerators, Spectrometers, Detectors and Associated Equipment*, 734, pp.116–121.

Weirich, C. et al., 2012. Analysis and correction of count rate reduction during simultaneous MR-PET measurements with the BrainPET scanner. *IEEE Transactions on Medical Imaging*, 31(7), pp.1372–1380.

Weirich, C. et al., 2010. Simultaneous PET and MR imaging with a newly developed 3TMR-BrainPET scanner. In *CEUR Workshop Proceedings*.

Wernick, M.N. & Aarsvold, J.N., 2004. Emission Tomography: The Fundamentals of PET and SPECT. *Elsevier Inc*.

Yamamoto, S. et al., 2010. Design and performance from an integrated PET/MRI system for small animals. *Annals of Nuclear Medicine*, 24, pp.89–98.

Yoshida, H., Hawkes, D. & Vannier, M.W., 2012. Abdominal Imaging : Computational and Clinical Applications. *Spinger*, pp.1–11.

Zeng, G., 2010. Medical Image Reconstruction : A Conceptual Tutorial. *Springer*.

Zhou, J. & Qi, J., 2011. Fast and efficient fully 3D PET image reconstruction using sparse system matrix factorization with GPU acceleration. *Physics in medicine and biology*, 56(20), pp.6739–57.

Zhou, L. et al., 2013. Improvement in motion correction technique for microPET brain imaging. In *IEEE Nuclear Science Symposium Conference Record*. pp. 1–4.

Zientara, G.P., 1995. Fast Imaging Techniques for Interventional MRI. *Interventional MR*, Ch 2, pp.25–52.

Zimmer, L. & Luxen, A., 2012. PET radiotracers for molecular imaging in the brain: past, present and future. *NeuroImage*, 61(2), pp.363–70.